

# Simulation of strain-induced and defect-controlled self-organization of nanostructures

Dissertation zur Erlangung des  
naturwissenschaftlichen Doktorgrades  
der Julius-Maximilians-Universität Würzburg

vorgelegt von  
Markus Walther  
aus Füssen

WÜRZBURG 2008

Eingereicht am 28. Februar 2008  
bei der Fakultät für Physik und Astronomie

1. Gutachter: Priv. Doz. Dr. Michael Biehl  
2. Gutachter: Prof. Dr. Wolfgang Kinzel  
der Dissertation.

1. Prüfer: Prof. Dr. Fakher Assaad  
2. Prüfer: Prof. Dr. Wolfgang Kinzel  
3. Prüfer: Prof. Dr. Jean Geurts  
im Promotionskolloquium.

Tag des Promotionskolloquiums: 20. Juni 2008

Doktorurkunde ausgehändigt am:

# Zusammenfassung

Im Rahmen dieser Doktorarbeit wird der Einfluss elastischer Verspannungen auf heteroepitaktisches Kristallwachstum mit Hilfe kinetischer Monte Carlo Simulationen untersucht. Von besonderem Interesse ist hierbei die Gitterfehlانpassung, die aus den unterschiedlichen Gitterkonstanten des Adsorbat- und des Substratmaterials herrührt. Dieser Gitterunterschied zeigt weitreichende elastische Verspannungseffekte mit starkem Einfluss auf den gesamten Kristall und dessen Morphologie. Hauptgegenstand der vorliegenden Arbeit ist die Untersuchung der wesentlichen Mechanismen, mittels deren die Kristallverspannungen abgebaut werden. Dabei gilt es ferner die maßgeblichen Parameter zu bestimmen, die es erlauben, die Relaxationsmechanismen zu kontrollieren.

Während das erste einleitende Kapitel zunächst an die Thematik heranführt, wird im zweiten Kapitel auf die Bedeutung der Molekularstrahlepitaxie (MBE) und deren experimentelle Umsetzung eingegangen. Da epitaktisches Wachstum fernab vom thermodynamischen Gleichgewicht stattfindet und somit stark von kinetischen Oberflächenprozessen beeinflusst wird, werden zunächst die relevanten mikroskopischen Prozesse beschrieben. Im Anschluss daran folgt ein Überblick über verschiedene unabhängige Methoden, die zur Modellierung epitaktischem Wachstums auf unterschiedlichen Zeit- und Längenskalen dienen, gefolgt von Charakterisierungsmöglichkeiten von Versetzungen und der Klassifizierung der verschiedenen Wachstumsmoden, basierend auf thermodynamischen Betrachtungen.

Das dritte Kapitel liefert eine detaillierte Beschreibung des verwendeten Modells und dessen Umsetzung mit Hilfe von Computersimulationen. Hierbei wird epitaktisches Wachstum mittels kinetischen Monte Carlo Simulationen verwirklicht, die es erlauben weitreichende Verspannungseffekte an Systemen mit einer Ausdehnung von einigen hundert Atomen zu untersuchen. Die Verwendung eines gitterfreien Simulationsmodells ermöglicht ferner den Teilchen, ihre vordefinierten Gitterplätze zu verlassen, was eine unverzichtbare Bedingung für die Simulation von Relaxationsmechanismen darstellt. Die Grundidee unseres Modells besteht darin, die Aktivierungsenergien aller relevanten thermisch aktivierten Prozesse mit Hilfe einfacher Paarwechselwirkungspotenziale zu berechnen, die in hohem Maße von den kontinuierlichen Teilchenabständen abhängen. Die Dynamik wird dadurch verwirklicht, dass jedes Ereignis entsprechend seiner Wahrscheinlichkeit

unter Verwendung eines verwerfungsfreien Algorithmus ausgeführt wird. Ferner werden das Kristallrelaxationsverfahren, die rasterbasierte Teilchenzugriffsmethode, welche die Simulationen erheblich beschleunigt, sowie die effiziente Implementierung des Algorithmus diskutiert.

In den weiteren Kapiteln findet unser Modell Anwendung in der Simulation der verschiedenen Mechanismen des Verspannungsabbaus beim heteroepitaktischen Wachstum. Um den Einfluss weitreichender elastischer Verspannungseffekte zu untersuchen, wurde der Großteil dieser Arbeit auf dem zweidimensionalen Dreiecksgitter bewerkstelligt, das als Querschnitt des realen dreidimensionalen Falls betrachtet werden kann.

Kapitel 4 behandelt den Verspannungsabbau durch die Bildung von Versetzungen sowie die sich daraus ergebenden Auswirkungen auf den weiteren Verlauf des Wachstums. Hierbei unterscheidet man zwei prinzipiell unterschiedliche Mechanismen der Versetzungsbildung, die unter zusätzlicher Berücksichtigung der Oberflächenkinetik maßgeblich vom Vorzeichen und Betrag der Gitterfehlpassung abhängen. Zusätzlich beeinträchtigen die Versetzungen die Gitterabstände innerhalb des Kristalls, deren Verlauf qualitativ gut mit experimentellen Beobachtungen übereinstimmt. Darüber hinaus beeinflussen Versetzungen den weiteren Wachstumsverlauf des Adsorbatfilms, da die potentielle Energie eines oberflächenteilchens durch vergrabene Versetzungen moduliert wird. Dabei besteht ein deutlicher Zusammenhang zwischen den lateralen Positionen der vergrabenen Versetzungen und denen der auf der Oberfläche gewachsenen Hügel.

Kapitel 5 befasst sich mit einer weiteren Möglichkeit, Verspannungen im Kristall abzubauen. Die Bildung dreidimensionaler Inseln ermöglicht den Teilchen sich ihrem bevorzugten Gitterabstand anzunähern. Im Rahmen unseres Modells ist es möglich, jede der drei epitaktischen Wachstumsarten einzustellen: Volmer–Weber, Frank–van der Merve oder Lage für Lage sowie die Stranski–Krastanov Wachstumsart. Ferner sind wir in der Lage zu zeigen, dass die sich einstellende Wachstumsart im Wesentlichen von zwei Parametern gesteuert werden kann: die erste wichtige Größe ist die Wechselwirkungsstärke zwischen Adsorbatteilchen untereinander verglichen mit jener zwischen Adsorbat- und Substratteilchen, den zweiten wichtigen Parameter stellt die Gitterfehlpassung zwischen Adsorbat und Substrat dar. Eine vernünftige Wahl dieser beiden Parameter erlaubt es, jede dieser drei Wachstumsarten zu simulieren. Schlussfolgernd kann gesagt werden, dass einerseits durch ein zu Grunde liegendes Versetzungsnetzwerk die Bildung von Nanostrukturen gesteuert werden kann, andererseits auch die durch Kristallverspannungen induzierte, regelmäßige Anordnung dreidimensional gewachsener Inseln in dem Konzept selbstorganisierter Strukturbildung Verwendung finden kann.

In Kapitel 6 erweitern wir schließlich unser Modell auf drei Dimensionen, was es uns ermöglicht, den Einfluss von Verspannung auf das Wachstum auf  $\text{bcc}(100)$  Oberflächen zu untersuchen. Um unter Verwendung der gitterfreien Methode ein stabiles  $\text{bcc}$ -Gitter zu erhalten, führen wir durch geeignete Modifikation ein ani-

sotropes Wechselwirkungspotenzial ein. Dabei zeigt sich, dass die Verspannung innerhalb der Monolageninseln hauptsächlich an den Inselrändern abgebaut wird und die Gitterfehlanpassung starken Einfluss auf die Diffusion in der Ebene genauso wie auf die Situation an den Inselrändern hat und somit bedeutende Auswirkungen auf das Erscheinungsbild von Submonolageninseln zeigt.

Zum Abschluss werden im letzten Kapitel nochmals die wesentlichen Ergebnisse zusammengefasst und die daraus resultierenden Schlussfolgerungen erörtert. Zu guter Letzt geben wir einen kurzen Ausblick auf weitere interessante Fragestellungen im Bereich heteroepitaktischer Wachstumssimulationen.



# Abstract

In this PhD thesis, the effect of strain on heteroepitaxial growth is investigated by means of Kinetic Monte Carlo simulations. In this context the lattice misfit, arising from the different lattice constants of the adsorbate and the substrate material, is of particular interest. As a consequence, this lattice misfit leads to long-range elastic strain effects having strong influence on the entire growing crystal and its resulting surface morphology. The main focus of this work is the investigation of different strain relaxation mechanisms and their controlling parameters, revealing interesting consequences on the subsequent growth.

While the first chapter aims at giving a brief introduction to the subject matter, which also includes remarks on the motivation for this work, in the second chapter we initially address the relevance of molecular beam epitaxy (MBE) and its experimental realization. Since epitaxial growth is carried out under conditions far away from thermodynamic equilibrium, it is strongly determined by surface kinetics. At this point the relevant kinetic microscopic processes are described, followed by theoretical considerations of heteroepitaxial growth disclosing an overview over several independent methodological streams, used to model epitaxy in different time and length scales, as well as the characterization of misfit dislocations and the classification of epitaxial growth modes based on thermodynamic considerations.

In the third chapter, a detailed description of the computational realization is given. The epitaxial growth is performed by means of Kinetic Monte Carlo simulations which allows for the consideration of long range effects in systems with lateral extension of few hundred atoms. By using an off-lattice simulation model the particles are able to leave their predefined lattice sites, which is an indispensable condition for simulating strain relaxation mechanisms. The main idea of our used model is calculating the activation energy of all relevant thermally activated processes by using simple pair potentials, depending decisively on the particles' distance in space, and then realizing the dynamics by performing each event according to its probability by means of a rejection-free algorithm method. In addition, the crystal relaxation procedure, the grid-based particle access method, which accelerates the simulation enormously, and the efficient implementation of the algorithm are discussed.

In the following chapters, our off-lattice model is applied to the simulation of

heteroepitaxial growth with regard to the different strain relaxation mechanisms. To study the influence of long range elastic strain effects, the main part of this work was realized on the two dimensional triangular lattice, which can be treated as a cross section of the real three dimensional case.

Chapter 4 deals with the formation of misfit dislocations as a strain relaxation mechanism and the resulting consequences on the subsequent heteroepitaxial growth. We can distinguish between two principally different dislocation formation mechanisms, depending strongly on the sign as well as on the magnitude of the misfit, but also the surface kinetics need to be taken into account. Additionally, the dislocations affect the lattice spacings of the crystal whose observed progression is in qualitative good agreement with experimental results. Furthermore, the dislocations influence the subsequent growth of the adsorbate film, since the potential energy of an adatom is modulated by buried dislocations. A clear correlation between the lateral positions of buried dislocations and the positions of mounds grown on the surface can be observed.

In chapter 5, an alternative strain relaxation mechanism is studied: the formation of three dimensional islands enables the particles to approach their preferred lattice spacing. We demonstrate that it is possible to adjust within our simulation model each of the three epitaxial growth modes: Volmer–Weber, Frank–van der Merve or layer-by-layer, and Stranski–Krastanov growth mode. Moreover, we can show that the emerging growth mode depends in principle on two parameters: on the one hand the interaction strength of adsorbate particles with each other, compared to the interaction of adsorbate with substrate particles, and on the other hand the lattice misfit between adsorbate and substrate particles. A sensible choice of these two parameters allows the realization of each growth mode within the simulations. In conclusion, the formation of nanostructures controlled by an underlying dislocation network can be applied in the concept of self-organized pattern formation as well as by the tendency to form ordered arrays of strain-induced three dimensional grown islands.

In chapter 6, we extend our model to three dimensions and investigate the effect of strain on growth on bcc(100) surfaces. We introduce an anisotropic potential yielding a stable bcc lattice structure within the off-lattice representation. We can show that the strain built up in submonolayer islands is mainly released at the island edges and the lattice misfit has strong influence on the diffusion process on the plane surface as well as on the situation at island edges with eminent consequences on the appearance of submonolayer islands.

The last chapter completes this work by summarizing the essential results, drawing conclusions and giving a short outlook to further subjects of investigation in the field of heteroepitaxial growth simulations.



# Contents

<b>1</b>	<b>Introduction</b>	<b>11</b>
<b>2</b>	<b>Description of heteroepitaxial growth</b>	<b>13</b>
2.1	Molecular beam epitaxy . . . . .	13
2.1.1	Experimental realization . . . . .	14
2.1.2	Microscopic processes on the crystal surface . . . . .	15
2.2	Misfit dislocations . . . . .	18
2.3	Classification of growth modes . . . . .	21
2.4	Theoretical description . . . . .	23
2.4.1	Density Functional Theory . . . . .	25
2.4.2	Molecular Dynamics . . . . .	26
2.4.3	Kinetic Monte Carlo simulations . . . . .	27
2.4.4	Continuum theory . . . . .	30
<b>3</b>	<b>Off-lattice Kinetic Monte Carlo simulations</b>	<b>33</b>
3.1	Lattice structures . . . . .	34
3.1.1	The triangular lattice . . . . .	34
3.1.2	The bcc lattice . . . . .	35
3.2	The potential energy . . . . .	36
3.2.1	The bulk equilibrium distance . . . . .	37
3.2.2	The potential energy surface . . . . .	38
3.3	Calculation of the activation energy . . . . .	39
3.3.1	Determination of the neighboring binding site . . . . .	40
3.3.2	Calculation of the transition state energy . . . . .	40
3.4	Local and global relaxation . . . . .	42
3.5	Downward funneling . . . . .	42
3.6	Kinetic Monte Carlo simulation . . . . .	43
3.6.1	Rejection-free method . . . . .	44
3.6.2	Grid-based particle access method . . . . .	45
3.7	Conclusions . . . . .	47

<b>4</b>	<b>Formation and consequences of misfit dislocations</b>	<b>49</b>
4.1	Formation of misfit dislocations . . . . .	50
4.1.1	Mechanisms of dislocation formation . . . . .	50
4.1.2	Behavior of the lattice spacings . . . . .	56
4.2	Influence of buried dislocations . . . . .	61
4.2.1	Positive misfit . . . . .	61
4.2.2	Negative misfit . . . . .	65
4.3	Conclusions . . . . .	68
<b>5</b>	<b>Simulation of the three different growth modes</b>	<b>71</b>
5.1	Simulation model . . . . .	72
5.2	Influence of the misfit on submonolayer islands . . . . .	74
5.3	Volmer–Weber-like growth . . . . .	77
5.3.1	Influence of the misfit on the diffusion process . . . . .	77
5.3.2	Characterization of the island growth . . . . .	79
5.3.3	Transition from layer-by-layer to VW growth . . . . .	85
5.4	Stranski–Krastanov-like growth . . . . .	90
5.4.1	Stable wetting layer . . . . .	91
5.4.2	Influence of the misfit on the island growth . . . . .	92
5.4.3	Transition from layer-by-layer to SK growth . . . . .	95
5.5	Conclusions . . . . .	100
<b>6</b>	<b>Growth on bcc(100) surfaces</b>	<b>103</b>
6.1	Simulation model . . . . .	104
6.2	Influence of the misfit . . . . .	108
6.2.1	Influence on the potential energy . . . . .	108
6.2.2	Characterization of submonolayer islands . . . . .	111
6.2.3	Evolution of the island density . . . . .	113
6.3	Conclusions . . . . .	115
<b>7</b>	<b>Conclusions and outlook</b>	<b>117</b>
<b>A</b>	<b>Pair-potentials</b>	<b>121</b>
A.1	The Lennard–Jones potential . . . . .	121
A.2	The Morse potential . . . . .	122
	<b>Bibliography</b>	<b>124</b>

# Chapter 1

## Introduction

The use and understanding of matter in its condensed state have accompanied the advances of civilization and technology throughout the history. While historical ages have often been named after the material dominating the technology of the time, the foundations of our understanding of the macroscopic properties of matter were established by the end of the nineteenth century [1].

The dawn of modern surface science dates back to the 1960s, where many studies on surface phenomena including basic theoretical concepts had been developed, but its breakthrough originates from the progress in vacuum technology, the development of surface analytical techniques and the occurrence of high-speed computers. The ability to study surfaces of materials on a microscopic scale can be traced back to spectacular advances in techniques such as scanning tunneling microscopy which enable us to observe individual atoms on surfaces. From the experimental point of view, an indispensable accomplishment is the ability to produce crystal surfaces with the desired quality in terms of material purity, uniformity and interface control. One of the most widely used techniques for producing high purity epitaxial layers of metals, insulators, and superconductors is the molecular beam epitaxy (MBE), conducted in ultra-high vacuum.

A complete understanding of the behavior of materials and fundamental principles requires theoretical and computational tools facilitated by the development and availability of high-speed computers allowing for even sophisticated theoretical studies. An emerging field of material research is the computational nano-engineering leading to nanometer-scale modeling and simulation methods, which enable and accelerate the design and development of nanoscale devices. Semiconductor quantum dot structures have attracted a lot of attention in recent years due to their exciting electronic properties and potential applications in opto-electronic devices. An alternative to conventional fabrication techniques like lithography is the self-assembled formation of nanostructures. Since the shape and size of nanostructures directly affect properties like the energy level quantization and the density of states of a system, it is necessary to study growth mechanisms such as growth mode and island evolution to obtain controllable

shape and size of nanocrystals. An additional concern for nanocrystal applications is the dislocation formation driven by strain relaxation, because it is related to carrier processes in nanocrystals.

In this work, the effect of strain on heteroepitaxial growth is investigated by means of Kinetic Monte Carlo simulations. The strain in crystals arises from the different lattice constants of the adsorbate and the substrate material. The main focus of this work is the investigation of different strain relaxation mechanisms and their controlling parameters, revealing interesting consequences on the further growth progression. Chapter 2 deals with the experimental realization of MBE and the description of the relevant atomistic processes, but also presents an outline of possible theoretical approaches. In chapter 3, the used model and method is described, which will be applied to the formation and consequences of misfit dislocations in chapter 4, and to the simulation of the three different growth modes in chapter 5. In chapter 6, we focus on submonolayer growth on  $\text{bcc}(100)$  surfaces and round off this work in chapter 7 with a summarizing conclusion and a short outlook to future fields of investigation.

# Chapter 2

## Description of heteroepitaxial growth

The epitaxial growth of thin films is of utmost technological importance and in almost the same manner it displays a variety of highly non trivial phenomena that makes it very interesting from a theoretical point of view as well. This work treats of crystal growth far from thermodynamic equilibrium by means of molecular beam epitaxy (MBE).

The term *epitaxy*, derived from the Greek expressions “epi” (on) and “taxis” (arrangement), was introduced by L. Royer in 1928 [2] and is used for the growth of a crystalline layer upon a crystalline substrate, where the crystalline orientation of the substrate imposes an order on the orientation of the deposit layer. While the term *homoepitaxy* is used when the deposit material and the substrate material are the same, *heteroepitaxy* is used in the case of different materials.

In this chapter, initially the relevance of MBE and its experimental realization is described followed by theoretical considerations of heteroepitaxial growth, including the effect of strain and the classification of the different growth modes.

### 2.1 Molecular beam epitaxy

Molecular beam epitaxy (MBE) is an Ultra-High-Vacuum (UHV)-based technique for producing high quality epitaxial structures made of semiconductors, metals or insulators with monolayer (*ML*) control. Compared to earlier vacuum deposition techniques, the control of the beam fluxes and growth conditions is significantly more precise in MBE. In principle, MBE is applicable to the growth of epitaxial layers of a wide variety of materials. As the technique allows to control the deposition on an atomic layer-by-layer basis, it is feasible to grow artificial crystals with periodicities not available in nature [3,4].

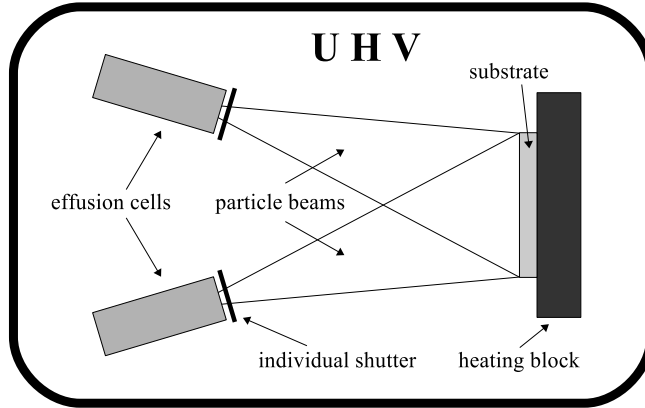


Figure 2.1: Schematic illustration of an MBE growth system.

### 2.1.1 Experimental realization

The epitaxial growth process is experimentally realized in an MBE growth chamber, which is illustrated in Fig. 2.1. Despite the conceptual simplicity, a great technological effort is required to produce systems that yield the desired quality in terms of material purity, uniformity and interface control.

As an object of physical investigations a well-defined surface has to be prepared on a particular solid under well-defined external conditions. The contamination by impurities or adatoms of another species leads to disturbances of the surface.

Under ultra-high vacuum (UHV) conditions, one or several adsorbate materials are heated up in effusion cells where they begin to evaporate. In form of a directed thermal atomic or molecular beam, the particles are deposited onto a chemically clean crystalline substrate surface of well-defined crystal orientation serving as seed crystal. The substrate is heated at fixed temperature to provide high mobility of the impinging particles for crystalline growth. In order to preserve the beam nature of the mass transport, the vacuum conditions are indispensable. The uniformity in thickness as well as in the composition of the films grown by MBE depends on the uniformities of the molecular beam fluxes and also on the geometrical relationship between the configurations of the sources and the substrate.

The substrate is attached to a manipulator that allows continuous rotation of the sample which causes an enhancement in thickness and composition homogeneity of the grown epilayer. The effusion cells are placed on a source flange, and are co-focused on the substrate heater to further optimize flux uniformity. Simple mechanic shutters in front of the beam sources are used to interrupt the beam fluxes and can be shut in a fraction of a second, which allows for nearly atomically abrupt transitions from one material to another.

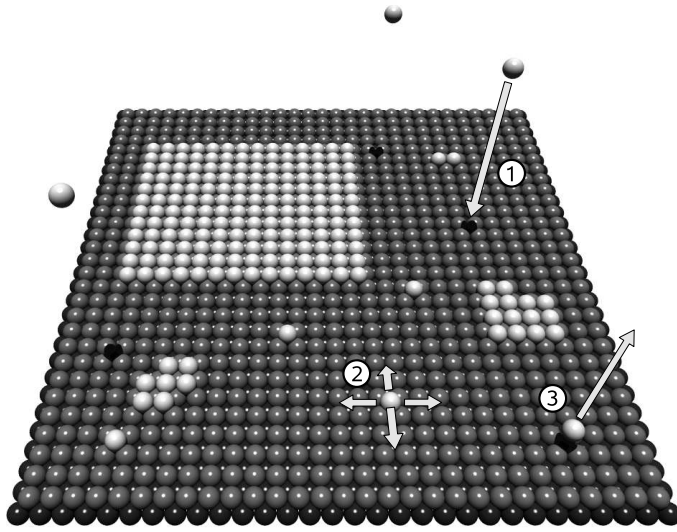


Figure 2.2: Schematic illustration of the relevant surface processes: deposition (1), diffusion (2), and desorption (3).

The UHV environment in the growth chamber allows the application of various in-situ measurements techniques to study the processes governing crystal growth. One possibility is monitoring the growth of the crystal layers by means of reflection high energy electron diffraction (RHEED) [5–7].

These measurements give qualitative feedback on the surface morphology and provide information about growth kinetics and can therefore be used to implement real-time feedback loops for growth control. This facility enables the fabrication of sophisticated device structures using the MBE growth technique.

### 2.1.2 Microscopic processes on the crystal surface

Epitaxial growth carried out under conditions far away from thermodynamic equilibrium is to a high degree determined by the kinetics of the surface processes occurring after the particles impinged onto the substrate surface, and the microscopic pathway taken by the system becomes decisive. Understanding and controlling growth morphologies in the kinetic regime therefore requires detailed knowledge of the microscopic processes involved.

One can distinguish between three elementary microscopic processes: deposition of particles on the surface, surface diffusion of the adatoms, and desorption of particles from the surface [8–10]. A schematic illustration of these processes is shown in Fig. 2.2. While the relaxation of the surface profile is driven towards equilibrium via surface diffusion, the deposition is a competing effect and drives the surface away from equilibrium. Although equilibrium concepts can be helpful in understanding certain aspects of epitaxial phenomena [11, 12], MBE is a non-equilibrium process with a number of effects that are of manifestly kinetic origin [8, 9, 13]. In the following the microscopic processes are described with respect to their feasible modeling.

## Deposition

The particles evaporate from the effusion cell and arrive in the form of an atomic or molecular beam and finally impinge on the substrate surface. The composition of the grown epilayer and its doping level depend on the relative arrival rates of the constituent elements and dopants, which in turn depend on the evaporation rates of the appropriate sources. The constant particle flux is normally given in monolayers per second, and typically ranges from  $10^{-3} MLs^{-1}$  to  $1 MLs^{-1}$ . In the so-called “mixing zone” the molecular beams intersect each other and the vaporized elements mix, while the mean free path of the molecules of these beams is considerably larger than the distance between the effusion cells and the substrate, and no collisions or other interactions between the molecules of different species occur.

The energy distribution of the atoms arriving at the substrate surface is accordant to the temperature of the effusion cell that is generally higher than the substrate temperature. Thus, some of the atoms re-evaporate immediately from the substrate. The arriving particles can also be accelerated by the attractive potential of the substrate and the kinetic energy is significantly higher than the energy corresponding to the substrate temperature [14]. In order to stick at the surface and not being reflected into the atmosphere, the impinging particles have to dissipate a sufficient fraction of their total energy, e.g. by transferring energy to the substrate in the form of lattice vibrations, until the temperature is adjusted to the substrate temperature.

A particle that has been adsorbed, called adatom, may still retain enough of its energy to keep moving ballistically over the surface. If the particle is unable to dissipate the energy gained in condensation, this energy allows the particle to skip several lattice sites and fly up to a special distance away from the point of the first impinge, until it becomes immobile. This *transient mobility* was motivated by the observation of layer-by-layer growth for temperatures, far below the onset of thermally activated diffusion [15]. An alternative explanation is a very short range (one to two atomic sites) transient mobility along three-dimensional surface structures built up in the early stages of growth. The so-called funnelling mechanism and other similar short-range atomic rearrangements like incorporation have been shown to have the effect of smoothing surface sufficiently [16], and can be implemented in simulation models [16–21].

The particles that have not re-evaporated again can be adsorbed at the surface. This can either be done by physical adsorption, often called *physisorption*, or by *chemisorption*. In the first case there is no electron transfer between the adsorbate and the adsorbent and the attractive forces are van der Waals type. In the latter case electron transfer between the adsorbate and the adsorbent takes place in terms of chemical reactions. This is usually observed when the interaction between the adsorbate and the substrate is very strong, which can even lead to dissociation of the adsorbate molecule.



## Diffusion

As the particle flux is chosen to be low enough, the impinging adatoms are able to move across the growing surface. The surface diffusion provides the mechanisms by which the diffusion particles find their way to the energetically most favorable incorporation sites and reproduce the correct crystal structure. Surface diffusion is a thermally activated process which explains the strong influence of the temperature on the crystal morphology. In order to diffuse to the next lattice position, the particle has to overcome an energy barrier. The transition path, which connects the initial and the final configuration of the adatoms, passes over a saddle point in the configuration space. The activation energy  $E_a$  is given by the difference between the potential energy of the transition state  $E_t$  and the potential energy of the initial binding site  $E_b$ :

$$E_a = E_t - E_b \quad (2.1)$$

A particle can gain enough energy from the thermal vibrations of surface atoms due to thermal fluctuations. The rate  $R$  for the diffusion process is given by the universal Arrhenius law for thermally activated processes:

$$R = \nu_0 e^{-\frac{E_a}{k_B T}}. \quad (2.2)$$

Here  $T$  denotes the temperature,  $k_B$  is the Boltzmann constant and  $\nu_0$  is the attempt frequency that is a measure for the time scale of the dynamics and is in the order of the debye frequency. To ensure that the adatom spends sufficient time between two jumps, so that equilibration can occur, a required condition is that  $R \ll \nu_0$  and therefore  $E_a \gg k_B T$  [22]. The transition state theory assumes that at each bonding site the adatom is in local thermodynamic equilibrium with the heat bath of system phonons, and the transition rate can be calculated as a local thermodynamic ensemble average. Besides the jumps from one adsorption site to the other, there is also the possibility of exchange diffusion or concerted motion which allows the particles to maintain a higher coordination during the migration step. The exchange diffusion was theoretically predicted [23] and experimentally observed [24] and confirmed [25, 26], and can even be energetically preferred for some systems [23].

If diffusing particles meet, they bond to form a two-dimensional island. And if additionally the adatom cluster formed by this nucleation process exceeds a critical size  $i$ , which means it contains more than  $i$  atoms, it keeps stable and immobile and the particles do not dissociate again. The new two-dimensional island grows by irreversible incorporation of further diffusing adatoms.

## Desorption

Besides the immediate reflection of an adsorbate particle impinging at the substrate surface due to its too high kinetic energy, also an already absorbed particle

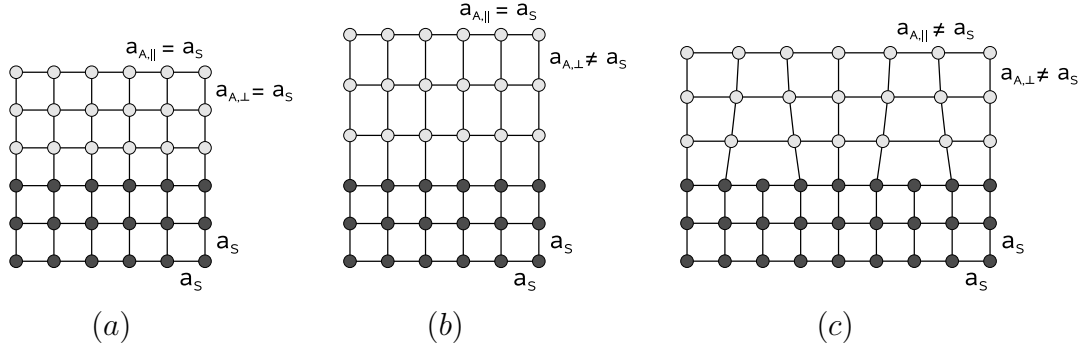


Figure 2.3: Schematic strain effects in heteroepitaxial growth: *lattice-matched* growth (a), *pseudomorphic* growth (b), and *dislocated* growth (c).

can escape again from the adsorption well if it gains enough energy from thermal vibrations. For this thermal desorption the particle has to overcome the energy barrier  $E_d$  which now is equal to the binding energy  $E_b$ . The resulting rate follows again an Arrhenius law. The binding energy depends on the particle's local environment and increases with the number of adjacent particles.

Due to high binding energies, the mean time a particle spends on the surface from deposition to desorption is usually longer than the time, given by the inverse particle flux, that is needed to deposit a complete layer. Thus, the particle is totally built in before the desorption process is performed. Therefore, the desorption can be neglected for many materials under typical MBE conditions. The desorption plays a more decisive role in the absence of a particle flux.

## 2.2 Misfit dislocations

In heteroepitaxy the substrate and the adsorbate film are of different materials and the crystal structure is necessarily not the same. The relative difference of their lattice constants is described by the misfit  $\varepsilon$ :

$$\varepsilon = \frac{a_A - a_S}{a_S}, \quad (2.3)$$

where  $a_i$  denotes the lattice constants of the substrate and the adsorbate. If the lattice constant is the same, ideal *lattice-matched*, *commensurate* growth takes place (Fig. 2.3a). Relatively low misfit can be accommodated by elastic strain, and the strained film adopts the periodicity of the substrate in the interfacial plane and is distorted in the perpendicular direction to preserve the volume of the unit cell. This *pseudomorphic* growth is illustrated in Fig. 2.3b.

For high values of misfit the strain is relieved by the formation of *misfit dislocations* at the substrate-adsorbate interface, see Fig 2.3c. The typical lateral

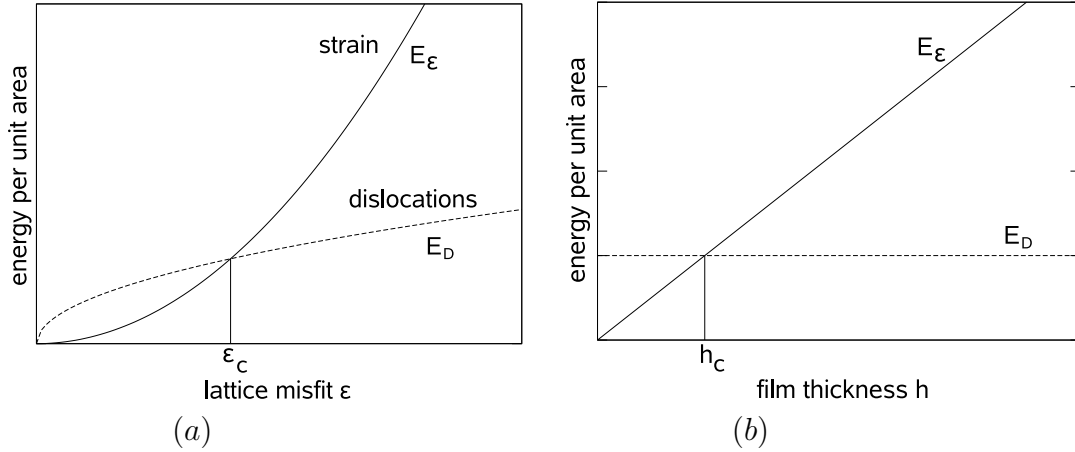


Figure 2.4: Schematic plot of the energy stored at the substrate-adsorbate interface per unit area (a) as a function of the misfit  $\varepsilon$  and (b) as a function of the film thickness. Strained pseudomorphic growth is energetically favored below a critical misfit  $\varepsilon_c$  and below a critical film thickness  $h_c$ . Beyond the critical values dislocated growth is favored.

distance  $d$  between the misfit dislocations is given by [10]

$$d = \frac{a_A a_S}{|a_A - a_S|}. \quad (2.4)$$

The relationship between the free energy density associated with the strain  $E_\varepsilon$  and that with dislocations  $E_D$  affects the occurring growth. The transition from pseudomorphic to relaxed growth is illustrated in Fig. 2.4, following [10]. Above a critical misfit  $\varepsilon_c$  the formation of misfit dislocations becomes energetically more favorable than a purely strained, pseudomorphic grown adsorbate film.

While the strain energy increases with the film thickness, the dislocation energy keeps constant. Consequently, the strain is released by the formation of a misfit dislocation at a critical film thickness  $h_c$  which can be identified as the intersection of the plots in Fig. 2.4b.

There are two different types of dislocations: *edge dislocations* and *screw dislocations*. An edge dislocation is a defect where an extra half plane is introduced through the crystal which distorts the lattice. The dislocation line of an edge dislocation is the line connecting all the atoms at the end of the extra plane. If the dislocation is such that a step or ramp is formed by the displacement of atoms in a plane in the crystal, then it is referred to as a screw dislocation. The dislocation line of a screw dislocation is the axis of the screw. In real materials the dislocations are normally mixed and have therefore characteristics of both.

The best way and fundamental quantity defining an arbitrary dislocation is its *Burgers vector* [27], which can be seen as a non-vanishing dislocation displacement vector. The Burgers vector is obtained by making a closed circuit (*Burgers*

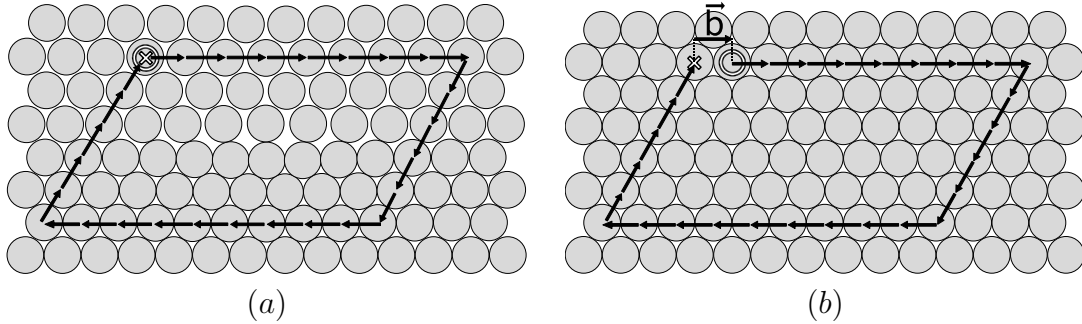


Figure 2.5: Construction of the Burgers vector of an edge dislocation in a two dimensional lattice: Image (a) shows a closed Burgers circuit around the dislocation, with identical starting point (circle) and ending point (cross). Image (b) shows the same chain of base vectors on a regular reference lattice. The starting point (circle) and the ending point (cross) now differ. The Burgers vector  $\vec{b}$  is defined as the vector closing the chain.

*circuit*) enclosing the dislocation from lattice point to lattice point. This leads to a closed chain of the base vectors defining the lattice, see Fig. 2.5a. As a reference, the same chain of base vectors is constructed on a regular, dislocation free lattice. Now, the chain is no closed circuit and the vector closing this chain is the Burgers vector  $\vec{b}$ , Fig. 2.5b. As long as the whole dislocation is enclosed the Burgers vector is independent of the choice of the lattice chain. The Burgers vector is perpendicular to the line direction in the case of an edge dislocation and parallel in the case of screw dislocations.

The position of a dislocation in a lattice is not fix and it can slip in planes containing both the dislocation line and the Burgers vector. While screw dislocations can slip in any plane, edge dislocations can only slip in one plane, as the Burgers vector is perpendicular to the direction line. In the so-called *dislocation glide* a dislocation is able to move rather easily by breaking and forming new bonds in the glide plane. The number of lattice sites of the whole system remains constant during this motion and the dislocation glide can be seen as a conservative motion [28].

The mechanism that also allows an edge dislocation to move out of its slip plane is the dislocation climb, caused by the movement of vacancies through the crystal lattice. Those glide and climb dislocations can be observed experimentally in thin films [29].

The direct observation of misfit dislocations between lead selenide (PbSe) and lead sulphide (PbS) using the transmission electron microscope technique was achieved in 1961 by Matthews [30, 31].

The formation of a misfit dislocation is not the only strain relaxation mechanism. As we will see in the next section, the stress can also be relieved by three dimensional island growth.

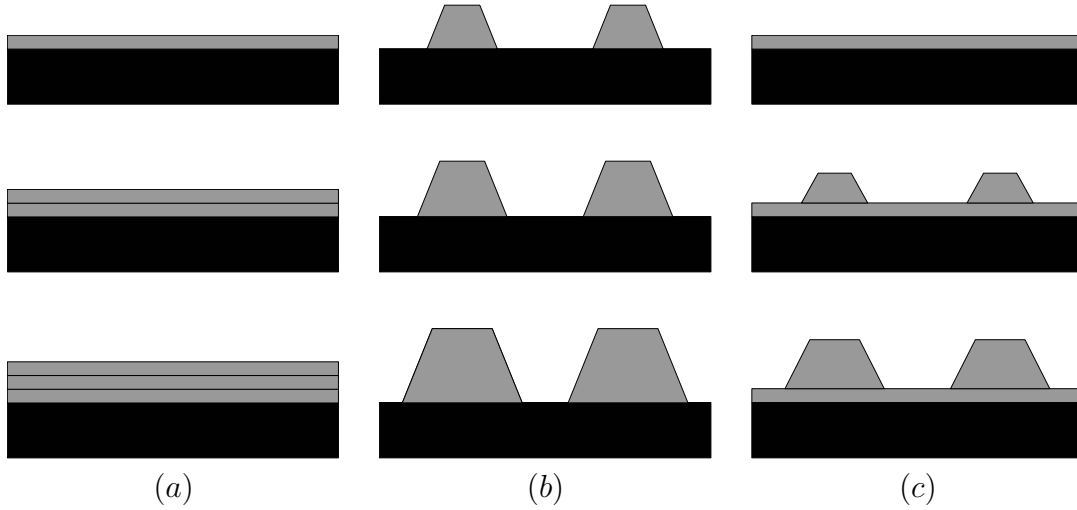


Figure 2.6: Schematic representation of the three main growth modes: (a) *Frank-van der Merve* growth mode, (b) *Volmer-Weber* growth mode, (c) *Stranski-Krastanov* growth mode.

## 2.3 Classification of growth modes

Concerning the acquired surface morphology one can distinguish between three mechanisms of epitaxial growth. The first classification of epitaxial growth modes based on thermodynamic considerations, which therefore applies to growth near thermodynamic equilibrium, was introduced by Bauer in 1958 [12]. These modes are named after their original investigators and are as follows: the *Frank-van der Merve* or layer-by-layer growth mode, the *Volmer-Weber* growth mode, and the *Stranski-Krastanov* growth mode. A schematic illustration of these three different growth modes is shown in Fig. 2.6.

As epitaxial growth is per definition a non-equilibrium process determined by kinetic phenomena, growth morphologies will deviate more or less from the thermodynamic picture and metastable growth modes are possible. In the strict sense, these equilibrium considerations can not be applied to MBE and the classification of growth modes is used in order to characterize the growing surface and distinguish between the different growth behaviors.

The different growth modes are distinguished according to the balance between the surface free energy of the adsorbate-vacuum interface  $\gamma_a$ , the surface free energy of the substrate-vacuum interface  $\gamma_s$  and the substrate-adsorbate interface free energy  $\gamma_i$ .

### Frank-van der Merve

In the *Frank-van der Merve* growth mode the film atoms are more strongly bound to the substrate than to each other. Consequently, each layer is fully completed

before the next layer starts to grow and strictly two-dimensional growth takes place. In this case the surface free energy relation is

$$\gamma_s \geq \gamma_a + \gamma_i \quad (2.5)$$

and the case of equality can normally only be fulfilled for homoepitaxial growth systems, where  $\gamma_i = 0$  by definition. This resulting layer-by-layer growth takes place during the entire growth, because any deviation from perfect layer-wise growth would increase the deposit surface area and cause an unnecessary increase of the total free energy, and according to the thermodynamic requirements this would be driven back again. The layer-by-layer growth mechanism is frequently observed in the case of metal deposits on metal substrates, classical examples are treated in [12, 32, 33].

### Volmer–Weber

In the *Volmer–Weber* growth mode the adsorbate particles are more strongly bound to each other than to the substrate particles, and the corresponding relation for the surface free energy is given by:

$$\gamma_s < \gamma_a + \gamma_i. \quad (2.6)$$

In this case the energy balance requires to minimize the area that is covered by the adsorbate material and the adsorbate will grow in the form of three-dimensional islands direct on the substrate.

### Stranski–Krastanov

The last case of the three heteroepitaxial growth modes is the *Stranski–Krastanov* growth mode and can be seen as the intermediate mode. If only the different surface energies of the substrate and the adsorbate material are considered, either the *Frank–van der Merve* or the *Volmer–Weber* growth mode appears at the thermodynamic limit, when the interface energy is neglected [12]. However, the growth mode also depends on the elastic strain in the film which depends on the lattice mismatch between the substrate and the adsorbate, see Eq. (2.3). If

$$\gamma_s > \gamma_a + \gamma_i, \quad (2.7)$$

the energy balance requires to maximize the area covered by the adsorbate material and the film will initially grow smoothly, one atomic layer at a time. In heteroepitaxial growth the lattice constants of the substrate and the adsorbate material normally differ, and the deposit material will be strained and stores elastic energy in this initial state of growth.

The condition (2.7) must break down after the deposition of a certain number of layers, because the chemical influence of the original substrate more and more

decreases and the two surface free energies  $\gamma_s$  and  $\gamma_a$  will be nearly identical. After the deposition of  $n$  layers the elastic influence of the original substrate leads to a strained  $n$ -th layer and causes a positive, nonzero interface energy  $\gamma_i$  between the layer  $n$  and the layer  $n + 1$  which invalidates the condition (2.7) and replaces it with condition (2.6) at a critical layer thickness. By beginning with the deposition of layer  $n + 1$ , the flat morphology is no longer stable and three dimensional islands will form on top of the  $n$  smoothly grown layers, which are combined usually called *wetting layer*.

In real growth systems a number of subtle details complicate the whole picture [34–36], but if the decay of the substrate chemical influence is faster compared to the substrate elastic influence at the growth front, the layer-by-layer growth breaks down which leads eventually to the formation of three dimensional islands for any epitaxial system that initially satisfies (2.7).

The detailed mechanism of island formation is not completely clear, but monolayers on top of the wetting layer play an important role and act as precursors for the formation of three dimensional islands. One explanation is that the stability of the edge atom of a monolayer island decreases with the island width and now a weakly bound edge atom is able to jump on that monolayer and can then be seed of a new monolayer island on top of the initial island. This process then is repeated several times resulting in the formation of three dimensional islands that can be understood as a phase transition.

It is of high technological interest to produce thin films with crystalline perfection and smooth interfaces which is only possible by a proper deviation from equilibrium. Growth morphologies created far from equilibrium, as it is in the case of heteroepitaxy by means of MBE, can strictly seen not be categorized in terms of these three near-equilibrium growth modes without further considerations. In heteroepitaxy energetic effects, due to the lattice mismatch and differences in surface free energies, and kinetic effects, due to the far from equilibrium growth conditions, can usually not be clearly distinguished in two contributions. But one often labels the kinetic growth modes according to the surface morphologies of the equilibrium consideration.

## 2.4 Theoretical description

Besides the experimental point of view, there is a high interest in the theoretical description of MBE growth as it is far from thermodynamic equilibrium and no general theoretical framework like equilibrium statistical mechanics is available. The emergence of tools for imaging surfaces at the atomic scale [37–39] has given valuable information about surface morphology and surface diffusion.

An important role in theoretical studies has been the identification of the processes that give rise to the surface structures observed in experiments. Effective control of the growth morphology relies on choosing conditions and systems that

shift the balance between competing atomic-scale processes in such a way as to favor the desired outcome.

A theoretical prediction of the growth process requires an accurate description of the atomic interactions and analysis of the rates of various atomic-scale transitions and the simulation of the growth on the experiment's timescale. Therefore it is of great importance to calculate atomistic rates for specific materials as an input into realistic growth simulations and for comparison with experimentally determined numbers. The rate of any process connecting two configurations can be obtained if the total energy of the surface is known for all possible atomic arrangements. The thermal motion of the atoms is slow compared to the dynamics of the electron system and the electronic ground state energy can be computed approximately for a static configuration of the atomic nuclei, which is known as the *Born-Oppenheimer* approximation. As a consequence the problem is reduced to the solution of the stationary Schrödinger equation for the many-electron system. The resulting calculation becomes intractable already for a moderate number of electrons.

The atomic interaction can be described at various levels of theory. The most general applicable approach is the first principles, or "ab initio" approach, where no adjustment of parameters is made to fit information about chemical bonds. The only input to the calculation is the chemical identity, like the charges of the nuclei, of the atoms involved.

The morphological evolution of an epitaxial film results from the interplay between the processes that are operative over a wide range of length and time scales [40, 41]. Consequently, a complete understanding of mechanical properties requires theoretical and computational tools that range from the atomic-scale detail of first-principles density functional methods to the more coarse-grained picture provided by continuum elasticity theory. Understanding the morphology and properties of epitaxial films requires accommodating the atomic-scale information about the movement of adatoms on surfaces and their various bonding configurations into the macroscopic evolution of the thin film. This involves a large disparity of length and time scales that range from one atomic vibrational period ( $10^{-12} - 10^{-15}$ s) to time scales for the formation of an atomic layer that even can take several minutes. One of the central problems of describing epitaxial phenomena is to find a way to incorporate systematically the atomistic information provided by first principle methods into computational models that are appropriate for macroscopic length and time scales.

In the following an overview over the several independent methodological streams used to model epitaxy in the corresponding time and length scales is given [42–44]. An illustration of the hierarchy of the different modeling methods is shown in Fig. 2.7, following [40].



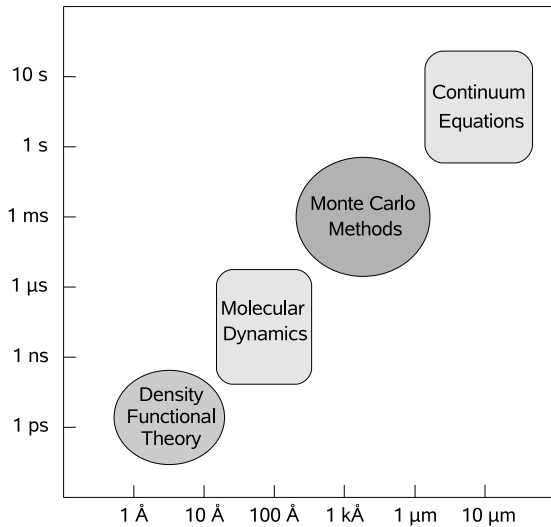


Figure 2.7: Illustrative ranking of modeling methods in the range of time and length scales they are typically used. The lower boundaries of each image define the basic spatial and temporal resolutions of the corresponding computational method. The upper boundaries are determined by computational and algorithmic limits, where continuum equations extend beyond the limits shown into the macroscopic domain.

### 2.4.1 Density Functional Theory

The first principle methods provide detailed information on the energetics of specific atomic configurations. The density functional theory (DFT) [45] is based on the theorem derived by Hohenberg and Kohn in 1964 [46]. The original theorem states in essence that an exact representation of the ground state properties of a stationary, non-relativistic many-particle system is possible in terms of the ground state density. So for an electron gas in an arbitrary external static potential  $V$ , resulting from the nuclei of the treated molecules, the potential is uniquely determined by the ground state energy density which therefore determines the ground state wave function through the Schrödinger equation. Hence, it contains in principle all information about the many body ground state properties. The density that minimizes the energy is the ground-state density and this minimum energy is the ground-state energy of the system.

In consideration of the Kohn-Sham equations [47] the intractable many-body problem of interacting electrons in a static external potential is reduced to a tractable problem of non-interacting electrons moving in an effective potential. This effective potential includes the effects of the Coulomb interactions between the electrons, for example the exchange and correlation interactions, and the external potential.

DFT calculations of surface dynamics have been applied very successfully [48–53] and in some cases they even led to reinterpretation of experimental data [48, 54]. The DFT calculations enable the evaluation of specific ground state energies of different reconstructions of a particular material surface and afford the detailed structure, that is the precise position of the atoms at the surface. The development of efficient algorithms and a better understanding of density functionals have made DFT to the primary method for calculating the proper-

ties of materials [55], including band structures, band gaps, cohesive energies, chemisorption energies or activation barriers for various kinetic processes [44]. The so gained information is very useful in the development of models describing the surface and its evolution [56–58]. But the ground state energies of only few surface configurations is not sufficient for the analysis of dynamical properties during crystal growth [59].

It is also important to keep in mind that the DFT calculations are not exact, as the exchange correlation energy and consequently the true density functional is not known and approximations are necessary. The most widely used approximation is the local density approximation (LDA), where the density locally can be treated as a uniform electron gas. Consequently, the electron exchange and the correlation energy at any point in space is only a function of the electron density at that point. Besides the need of approximation in the density, there is a further restriction. Due to the great computational efforts, the DFT calculations are restricted to a small number of particles and small time intervals which makes it for instance impossible to include long-range elastic strain effects properly.

### 2.4.2 Molecular Dynamics

One important tool for describing the temporal evolution of many particle systems is Molecular Dynamics (MD). In this method, which is explained in many textbooks [60–62], the evolution of a system of  $N$  mutually interacting particles is calculated by numerical integration of the equations of motion. The simplest case is assuming classical interactions of the particles, whereas the used potentials range from simple pair or many particle potentials to highly sophisticated material specific potentials, which can be either obtained by first principle DFT considerations or by fitting suitable parameterizations to experimentally observed material properties. Pair potentials, such as the Lennard–Jones and the Morse potential are used for large-scale simulations where a generic description is sufficient rather than detailed comparisons with particular material systems. The potentials determine the forces acting upon each particle in the system. Other constraints may be placed on the system, such as a fixed temperature and the restriction of particle activity to a fixed volume of space. By choosing a particular potential, the information concerning energy barriers for particular kinetic processes and the relative probability of different events is provided. Thus, there is no guarantee that the chosen potential is appropriate for all of the atomic configurations that occur during the kinetic processes being studied, which limits the practical application of MD simulations in the context of crystal growth.

Besides the classical consideration, it is also possible to include the quantum mechanics of the systems into the MD description. In this *ab initio* MD simulations, the forces are determined by performing a DFT total energy calculation in each time step [63]. In the *Car-Parrinello method* [64] the only assumptions are the validity of classical mechanics to describe the ionic motion and the *Born-*

*Oppenheimer approximation* to separate nuclear and electronic coordinates. The minimization of the Hohenberg-Kohn functional is carried out simultaneously with the classical motion of the nuclei by endowing the Kohn-Sham wave functions with a fictitious classical dynamics [65].

Therefore, the quantum molecular dynamics in principle provides the most accurate way of modeling epitaxial growth but suffers, as well as the classical MD, from the fact that processes such as atomic diffusion are inherently multi-scale phenomena and the basic time step must be shorter than the vibrational period of an adatom, about  $10^{-13}$ s which is to be contrasted with a typical monolayer completion time in a growth experiment, that usually lasts several seconds or even minutes. Quantum MD simulations are limited to system sizes of a few hundred atoms and to elapsed real times of a few picoseconds. Even with acceleration techniques, as proposed in [66], the relevant time scales cannot be achieved. By the application of MD simulations to thermally activated processes like surface diffusion, a large part of the simulation time is spent for the description of collective vibrations of the crystal atoms which do not change the system configuration significantly, as diffusion steps are quite rare. Consequently, most implementations of MD simulations of epitaxial growth have used unrealistic high growth rates in order to deposit a significant amount of material during the course of the simulation [67, 68].

Nevertheless, MD simulations have proved to be highly useful for investigating individual atomistic processes during crystal growth, which proceed on short time scales and involve the motion of several atoms. This are for example the transient motion of the deposited atom along the surface or the process of funneling and steering which are involved in the condensation at steps [14]. The MD is also a good tool to identify exotic exchange mechanisms [69].

### 2.4.3 Kinetic Monte Carlo simulations

Depending on the time scale of interest, the atomistic processes involved in crystal growth can be modeled deterministically or stochastically. The motion of the atoms takes the form of complex trajectories resembling irregular orbits that are located close to individual sites [40], but only occasionally these trajectories take an atom from one site to another. This observation motivates an approximate description of adatom kinetics and the time scale limitation of the MD simulations can be overcome, if one only regards processes that lead to relevant changes of the system configuration. This is the basic philosophy of the Kinetic Monte Carlo method applied to epitaxial phenomena [70, 71] and is used in the simulations of the present work.

Initially, the principles of equilibrium thermal Monte Carlo simulations will be discussed, followed by the realization of Kinetic Monte Carlo simulations.

In a Monte Carlo simulation a stochastic process is numerically realized, in which a system develops over a set of configurations  $\{C\}$  with prescribed transi-

tion rates  $R(C_m \rightarrow C_n)$  for passing from the configuration  $C_m$  to configuration  $C_n$  [14]. In statistical physics, Monte Carlo simulations have been applied to the evaluation of thermodynamic equilibrium properties of interacting many-body systems [72]. The simulation is used to generate a set of sample configurations with statistical weights corresponding to the correct equilibrium distribution, the Boltzmann probability distribution [73].

The states are generated by a so called *Markov process*, where the transition probabilities do not vary over time and only depend on the properties of the initial and the final state [73]. In the simulation a Markov process is used repeatedly to generate a *Markov chain* of states. If the Markov process is performed a sufficient number of times, starting from any state of the system, the different states appear with probabilities given by the Boltzmann distribution. To achieve this, the condition of ergodicity is required, which means that it should be possible to reach any state of the system from any other state, if the process is run long enough.

The probability of the state  $C_m$  is denoted by  $p(C_m, t)$  and the change of the probability  $p(C_m, t)$  with the time  $t$  can be written in the following master equation [72, 74]:

$$\frac{dp(C_m, t)}{dt} = \sum_{n=1}^N W(C_n \rightarrow C_m) p(C_n, t) - \sum_{n=1}^N W(C_m \rightarrow C_n) p(C_m, t), \quad (2.8)$$

while  $W(C_m \rightarrow C_n)$  denotes the transition probability to move from the state  $C_m$  to the state  $C_n$  and  $N$  the number of configurations. This equation can be considered as a continuity equation and describes the balance of gain and loss processes. In equilibrium the probability becomes stationary,  $\dot{p}(C_m, t) = 0$ , and using  $\sum_{n=1}^N W(C_m \rightarrow C_n) = 1$  leads to

$$\sum_{n=1}^N W(C_n \rightarrow C_m) p(C_n, t) = p(C_m, t). \quad (2.9)$$

If the principle of *detailed balance*

$$W(C_n \rightarrow C_m) p_{eq}(C_n) = W(C_m \rightarrow C_n) p_{eq}(C_m) \quad (2.10)$$

is fulfilled, the equilibrium probability  $p_{eq}(C_m)$  is a solution of the stationary master equation (2.9). The condition of detailed balance is sufficient but not necessary for the convergence of the generated Markov chain [75]. There are many ways to satisfy these constraints, one of the most famous and widely used algorithm is the *Metropolis algorithm*, introduced by Nicholas Metropolis and his co-workers in a 1953 paper on simulations of hard sphere gases [76]. The algorithm works by repeatedly choosing a new state and then accepting it or

rejecting it with respect to the chosen acceptance probability fulfilling the condition of ergodicity. Concretely, a possible transition from the configuration  $C_m$  to  $C_n$  leads to a change of the system energy  $\Delta E = E_n - E_m$  and is accepted with certainty if the system energy is lowered and accepted otherwise with the probability  $\exp[-\Delta E/k_B T]$ .

In contrast to this kind of thermodynamic Monte Carlo simulation, the Kinetic Monte Carlo (KMC) simulations aim at modeling the time evolution of systems describing non-equilibrium phenomena such as MBE crystal growth. Therefore, all relevant kinetic processes have to be identified. As the quality of the simulation is only as good as the quality of the input, one has to ensure that no important process is missing to avoid erroneous results. By taking care of the physical properties, each thermally activated process is assigned a rate of Arrhenius form (cf. Sec. 2.1.2):

$$R = \nu_0 e^{-\frac{\Delta E}{k_B T}}. \quad (2.11)$$

If the considered process refers to surface diffusion,  $\Delta E$  denotes the activation energy  $E_a$  given by the difference between the potential energy of the transition state  $E_t$  and the potential energy of the initial binding site  $E_b$ :

$$\Delta E = E_t - E_b. \quad (2.12)$$

A precondition for the validity of the expression (2.11) is the separation of time scales between the attempt frequency  $\nu_0$  and the transition rate  $R$ . The relation  $R \ll \nu_0$  ensures that the system loses its memory between subsequent transitions. The time required for the actual motion across the energy barrier is much shorter than the waiting time between these transitions which can be regarded as instantaneous, and approximately no two transitions occur simultaneously and the evolution can be described as a sequence of configurations separated by individual atomistic events [14].

In the Arrhenius law (2.11) the attempt frequency  $\nu_0$  is assumed to be time independent. This approximation is justified in the Transition State Theory (TST) [77, 78], which is based on the assumption of thermal equilibrium between the occupation of the binding and transition states [79]. The rate of the kinetic process is

$$R = \frac{k_B T}{h} e^{-\frac{\Delta F}{k_B T}}, \quad (2.13)$$

where  $h$  denotes the Planck's constant and  $\Delta F$  is the difference of the free energy of the transition state and the binding state and given by [80]:

$$\Delta F = \Delta E - T \Delta S \quad (2.14)$$

The migration barrier  $\Delta E$  is approximately the difference in static potential energy between the transition state and the adsorption minimum, as the dynamic

barrier taking into account of the vibrational internal energy differences is negligible [37]. The rate can be separated then into an entropy and an energy term which leads direct to Eq. (2.2) with the attempt frequency

$$\nu_0 = \frac{k_B T}{h} e^{\frac{\Delta S}{k_B}}. \quad (2.15)$$

The decrease in the vibrational entropy difference  $\Delta S$  ( $\Delta S < 0$ ) in the exponential of Eq. (2.15) compensates the linear increase of its prefactor with increasing temperature [37]. Experimental observations confirm that the energy barrier and the prefactor are approximately constant [81] and therefore it is often simply assumed that the attempt frequency is the same for all possible diffusion processes in the system. A popular choice is  $\nu_0 = 10^{12} s^{-1}$  corresponding to the typical frequency of atomic vibrations [42]. The assumption of a constant attempt frequency lets the Arrhenius rates satisfy the condition of detailed balance (2.10), [14].

As the KMC performs directly the activated diffusion steps, it overcomes the timescale problem of the MD as discussed above. The KMC is a good tool to test ideas on how the interplay of various microscopic processes determines the film and island morphology. Many aspects of thin film growth such as island size distributions, kinetic roughening, and island morphologies have been addressed with that technique.

The disadvantage of this method is the requirement of a predetermined set of possible configurations and transitions in advance of the simulation which can be problematic in the case of complicated rearrangements involving several atoms. In order to combine the dynamic character of the KMC method with the determination of transitions during the simulation, several hybrid approaches were suggested [14, 66].

#### 2.4.4 Continuum theory

In order to examine macroscopic regions in space over extended periods of time, a reduced description of the system in terms of continuous fields is favorable. If one is interested to simulate the roughness of the surface or the shape of islands and other structures formed on the surface during crystal growth, the evolution of an epitaxial growth front can be described with a continuous function giving the height of the surface as a function of the lateral position. The effect of diffusion and other dynamics can be represented by a set of differential equations which neglect the underlying atomic structure of matter.

A stochastic differential equation capable to describe kinetic roughening is the *Langevin equation* of the form:

$$\frac{\partial h(\vec{r}, t)}{\partial t} = \kappa (\nabla h(\vec{r}, t), \nabla^2 h(\vec{r}, t), \dots) + \delta F(\vec{r}, t). \quad (2.16)$$

The Langevin equation contains a deterministic term that has a relaxing and smoothing effect on the surface and is represented by  $\kappa$ , a polynomial function of the derivatives of the height  $h(\vec{r}, t)$ , and a random noise term describing the fluctuations in the deposition flux [82], which is represented by  $\delta F(\vec{r}, t)$ .

A Langevin equation containing the most relevant terms appropriate to describe a particular growth situation defines the *universality classes* of kinetic roughening which can be distinguished in conserved and non-conserved growth [83]. In conserved growth the volume of the growth film is conserved and hence  $\kappa$  has the form

$$\kappa = -\nabla \mathbf{J}(\nabla h(\vec{r}, t), \nabla^2 h(\vec{r}, t), \dots). \quad (2.17)$$

Conserved growth equations are appropriate to describe epitaxial crystal growth without desorption and vacancy formation, ideal MBE [84], as the volume of the growing film only depends on the number of atoms independent of the surface processes [14]. The most robust conserved universality class is the *Edwards–Wilkinson* equation:

$$\frac{\partial h(\vec{r}, t)}{\partial t} = K \nabla^2 h(\vec{r}, t) + \delta F(\vec{r}, t), \quad (2.18)$$

where  $K$  is a positive coefficient. Non-conserved self-affine growth is described by the *Kardar–Parisi–Zhang* equation:

$$\frac{\partial h(\vec{r}, t)}{\partial t} = K \nabla^2 h(\vec{r}, t) + \lambda (\nabla h)^2 + \delta F(\vec{r}, t). \quad (2.19)$$

The physical meaning of the nonlinear term  $\lambda(\nabla h)^2$  is that the local growth rate of the film depends on the local surface slope.

The advantage of continuum models, such as phase field models [85, 86], is the computational simplicity [41]. Continuum equations play an important role in establishing connections between microscopic processes and the macroscopic evolution of the growth front. By parameterizing a KMC model with first principle calculations, which then could be converted into a stochastic partial differential equation, a connection across length and time scales could be achieved [40].





## Chapter 3

# Off-lattice Kinetic Monte Carlo simulations

In the last chapter, the experimental realization of heteroepitaxial growth by means of MBE technique was described and an overview over the most important theoretical approaches was given as well. The method of choice strongly depends on the length and time scale one is interested in. In heteroepitaxial systems, the different lattice constants of the adsorbate and the substrate material lead to long-range elastic strain effects which affect the entire growing crystal.

The computational efforts restrict Density Functional Theory calculations to a small number of particles and to small time intervals. The time scale limitation of Molecular dynamics simulations refuses the consideration of larger systems growing several monolayers. The main focus of this work is the effect of strain on growing systems, hence the heteroepitaxial growth is investigated by means of Kinetic Monte Carlo simulations, which allows for the consideration of long-range effects in systems with lateral extension of few hundred atoms.

If the material is expected to crystallize in a regular lattice without dislocations or other defects, the so called *lattice gas models* can be used, where a particular site is either occupied or empty and the particles can only be placed precisely on the lattice sites [42, 87, 88]. In some material systems the atoms at the crystal surface may be slightly shifted from their corresponding bulk positions due to surface reconstructions and, as long as the topology of the lattice remains unchanged, this effect can be taken into account within the lattice gas framework by adding additional discrete degrees of freedom to the model [58, 89].

However, the formation of misfit dislocations as a strain relaxation mechanism demands the possibility of particles leaving their predefined lattice sites. Consequently, the representation of the system by a rigid lattice is not suitable for this kind of simulation of heteroepitaxial growth. Instead of the lattice gas models, an off-lattice model can be used that allows for continuous particle coordinates in space enabling the atoms to be displaced from their initial predefined lattice site. Such models were suggested for example by Plotz et al. [90] and implemented in

simulations for instance in [91–95].

The main idea of our method is based on the work by Schindler and Wolf [96]. The interaction of the particles is described by pair-potentials as a function of the continuous particle distances. The activation energy of the relevant thermally activated processes is calculated by the change of the total energy, obtained with the interaction potential, and then used to determine the corresponding hopping rates, which are put in a standard rejection-free Kinetic Monte Carlo simulation.

In the following sections the simulation model and the used method of this work are described in detail.

## 3.1 Lattice structures

One of the first steps in the construction of a simulation model for epitaxial growth is the choice of the proper lattice structure which depends on the purpose of the simulation. Besides the chemical nature of the atoms, their geometrical arrangement governs the electronic, magnetic, optical and other properties of the surface. If one is interested in the description of a specific material system, it is indispensable to choose the corresponding lattice structure, as the topology determines for instance the potential diffusion events and neighborhood relations. Otherwise, if one addresses general aspects and phenomena of epitaxial growth on a qualitative level, the description by using a simple lattice structure is justified.

Besides the choice of the lattice type, it is also important to choose the correct surface orientation. For example, the surface of a body-centered cubic (bcc) lattice is isotropic in the (100) orientation direction but anisotropic in the (110) direction, which has a pronounced influence on the surface morphology.

### 3.1.1 The triangular lattice

Off-lattice Kinetic Monte Carlo simulations demand high computational efforts which restrict the simulated physical time and the system size. To study the influence of long range elastic strain effects like the influence of misfit dislocations on the subsequent growth or strain induced island growth, the main part of this work was realized on a lattice in 1+1 dimensions (substrate + height), which can be treated as a cross section of the real 2+1 dimensional case.

On a qualitative level, all the essential properties of the real 2+1 systems are given correctly in 1+1 dimensions. This assumption also implicates that in the real three dimensional case the monolayer islands have a compact rather than a fractal shape and a possible lattice misfit is one and the same in both orthogonal directions.

Including simple isotropic pair potentials, the particles arrange in the triangular lattice structure, illustrated in Fig. 3.1, with stacking *ABAB* yielding a coordination number of six. The resulting distance of the layers in the vertical

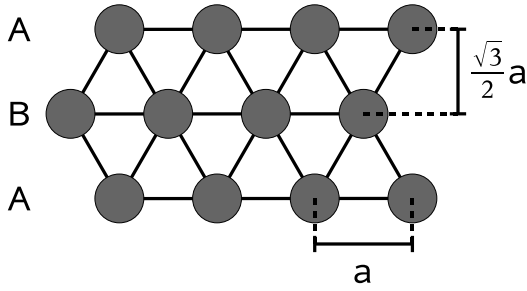


Figure 3.1: Illustration of the triangular lattice in two dimensions with stacking *ABAB*.

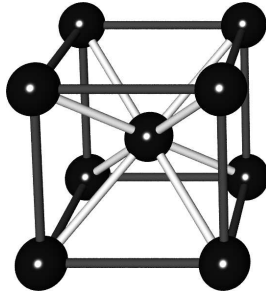


Figure 3.2: Illustration of the bcc lattice structure, obtained by adding an additional particle to the center of the simple cubic lattice. The light bonds represent the bonds to its nearest neighbors yielding the coordination number eight.

direction is  $a\sqrt{3}/2$ , where  $a$  denotes the lattice constant given in lateral direction. An infinite triangular lattice has a six-fold rotational symmetry. In the simulations, the lateral system size is typically in the order of few hundred particles which excludes possible finite size effects. To avoid undesired edge effects, periodic boundary conditions in the horizontal direction are assumed.

### 3.1.2 The bcc lattice

The two dimensional model represented on the triangular lattice can be extended to three dimensions that allows for different possible lattice structures. One of the most common cubic lattice types is the face centered cubic (fcc) which is close packed and the usual lattice structure for the majority of crystalline metals and therefore subject matter of many experimental and theoretical studies, e.g. the investigation of self assembled nanopatterns on the fcc (111) surface by means of an off-lattice Kinetic Monte Carlo simulation model [97].

Another common three dimensional cubic Bravais lattice is the body centered cubic (bcc) which is the lattice structure of iron and the alkali metals. Amongst others, they play an important role in the research in magnetic thin films and a growing interest is focused on nanostructured films made of objects of reduced lateral dimensions like magnetic dots. To give one example, the growth and magnetism of iron films on tungsten have been extensively investigated in the past [98–100].

The geometric arrangement of the bcc lattice is illustrated in Fig. 3.2. This lattice is obtained by adding an additional particle to the center of each cubic of the lattice given in the simple cubic structure. Thus, the central atom is cubically

surrounded and the resulting coordination number is eight and the stacking is *ABAB*. Every edge particle can be seen as a central particle of a further cubic and thus, every central particle is edge particle. One can also think of this lattice as made from layers of square-packed spheres and alternating layers stack, so that the spheres “nestle down” into the spaces between the spheres in the layer below.

In this work, the influence of strain in the submonolayer regime was studied on a bcc lattice in the (100) surface direction. The detailed implementation of this lattice structure to the off-lattice simulation model is given in chapter 6.

## 3.2 The potential energy

The next step in constructing the simulation model is the description of the particle interaction. By choosing a particular potential, the information concerning energy barriers for the thermally activated kinetic processes is provided. As this model does not aim at giving a detailed comparison to particular material systems, a generic description given by simple pair potentials is sufficient. The simple pair potentials used in this work are the Lennard–Jones potential and the Morse potential (cf. appendix A). In the main part of this work, the Lennard–Jones potential was used in the form

$$U_{ij}(U_0, \sigma, r_{ij}) = 4 U_0 \left[ \left( \frac{\sigma}{r_{ij}} \right)^{12} - \left( \frac{\sigma}{r_{ij}} \right)^6 \right]. \quad (3.1)$$

While  $U_0$  denotes the potential depth, the parameter  $\sigma$  is the distance at which the potential is equal to zero and specifies the different material properties in the model. The argument  $r_{ij}$  represents the continuous particle distance between the interacting particles  $i$  and  $j$ .

The attractive contribution in the potential competes with the strong repulsive part dominating at small distances. While the exponent “6” of the attractive part is motivated by van der Waals dispersion forces, originated by dipole-dipole interactions in turn due to fluctuating dipoles, the only condition for the exponent of the repulsive part is being higher than the exponent of the attractive part. Therefore the exponent “12” is chosen exclusively for practical reasons, as it allows to calculate the potential energy very efficiently, since  $r^{12}$  is the square root of  $r^6$ . The repulsive part results from the *Pauli exclusion principle* of electrons with overlapping orbitals. The potential also determines the force between two particles  $i$  and  $j$  which is given by

$$\vec{F}_{ij} = -\nabla U_{ij}. \quad (3.2)$$

The competition between the attractive and the repulsive contribution of the potential leads to a minimum value of the energy at the equilibrium distance  $r_0 = 2^{1/6} \sigma$ , where the force  $\vec{F}_{ij}$  between the two particles vanishes.

The interaction potential now allows for the calculation of the total energy of any atomic arrangement. The total potential energy of a system consisting of  $n$  particles is

$$E_{tot} = \sum_{i=1}^n \sum_{j=i+1}^n U_{ij}. \quad (3.3)$$

The force  $\vec{F}_{ij}$  acting upon each particle in the system leads to a local minimization of the potential energy (3.3).

While in Molecular Dynamics the force defined in Eq. (3.2) drives the system energy to a local minimum, in our KMC simulation model the minimization of the total energy is accomplished by means of a conjugate gradient method [101]. Note that the relaxation procedure only takes the energy of the system to its nearest local minimum which is achieved by small changes of the particle positions without changing the crystal topology. In order to stabilize the crystal, the particle positions of three bottom layers are fix. Due to the fact that the film thickness of the fix bottom layers is concordant with the cut-off distance, undesired edge effects can be avoided.

Since the interaction strength decreases fast with the particle distance, a cut-off distance  $r_{cut}$  with  $U_{ij} = 0$  for  $r_{ij} > r_{cut}$  is assumed. In most cases the cut-off is chosen to be  $r_{cut} = 3r_0$ , because the value of the potential calculated with Eq. (3.1) is already less than one percent of the value at the equilibrium distance  $r_0$ . This cut-off is necessary, since the computer time required for calculating the energy increases with the number of involved particles, and the energy contribution of the particles beyond the cut-off distance is negligible.

### 3.2.1 The bulk equilibrium distance

As every particle interacts with all other particles of the system, the resulting equilibrium distance of a bulk particle to its nearest neighbors slightly differs from the equilibrium distance  $r_0$  of two isolated particles. Consequently, if one is interested in building up a substrate crystal without artificial strain,  $r_0$  has to be replaced by the bulk equilibrium distance which can be obtained by preliminary calculations.

The energy  $E_i$  of a particle  $i$  in the bulk is given by the summation of all pair interactions with all system particles:

$$E_i = \sum_{j \neq i} U_{ij}. \quad (3.4)$$

The energy of a bulk particle strongly depends on the used lattice structure. In the following, the considerations refer to the two dimensional triangular lattice structure, but can be applied in the same manner to the three dimensional lattice representation. In the case of a cut-off distance  $r_{cut} = 3R$ , where  $R$  denotes the

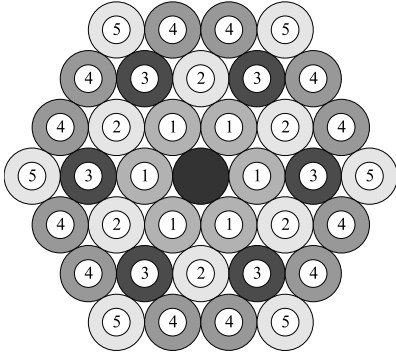


Figure 3.3: Particles contributing to the total potential energy of a bulk particle on the triangular lattice with cut-off distance  $r_{cut} = 3R$ . The number denotes the corresponding nearest neighbor ranking.

distance to the nearest neighbor, only the particles of the environment illustrated in Fig. 3.3 need to be taken into account. By using the Eq. (3.1) and (3.4), the total energy of a bulk particle  $i$  can be calculated as a function of the nearest neighbor distance  $R$ :

$$\begin{aligned}
 E_i(R) &= \sum_j 4 U_0 \left[ \left( \frac{\sigma}{r_{ij}} \right)^{12} - \left( \frac{\sigma}{r_{ij}} \right)^6 \right] \\
 &= 4 U_0 \left[ \sum_j \left( \frac{\sigma}{r_{ij}} \right)^{12} - \sum_j \left( \frac{\sigma}{r_{ij}} \right)^6 \right] \\
 &= 4 U_0 \left[ A_{12} \left( \frac{\sigma}{R} \right)^{12} - A_6 \left( \frac{\sigma}{R} \right)^6 \right]. \tag{3.5}
 \end{aligned}$$

The coefficient  $A_m$  ( $m = 6$  or  $m = 12$ ) denotes the lattice sum and, in consideration of the chosen lattice structure and the cut-off distance, is given by

$$A_m = 6 \times 1 + 6 \times \left( \frac{1}{\sqrt{3}} \right)^m + 6 \times \left( \frac{1}{2} \right)^m + 12 \times \left( \frac{1}{\sqrt{7}} \right)^m + 6 \times \left( \frac{1}{3} \right)^m. \tag{3.6}$$

The position of each summand in Eq. (3.6) corresponds to the number labeled on the particles in Fig. 3.3. By minimizing the energy (3.5), the equilibrium distance  $R_0$  in the bulk can be calculated.

$$\frac{\partial E_i(R)}{\partial R} = 4 U_0 \left[ 12 A_{12} \left( \frac{\sigma^{12}}{R^{13}} \right) - 6 A_6 \left( \frac{\sigma^6}{R^7} \right) \right] \stackrel{!}{=} 0 \tag{3.7}$$

yields an equilibrium distance  $R_0 \approx 1.1119 \sigma$ , which is slightly smaller than the equilibrium distance  $r_0 = 2^{1/6} \sigma \approx 1.1225 \sigma$  of two isolated particles.

Since the main focus of this work is the influence of strain in heteroepitaxial growth systems, the exact determination of the equilibrium distance is indispensable, as already small deviations lead to artificial strain in the crystal.

### 3.2.2 The potential energy surface

The temporal evolution of the surface morphology is mainly influenced and determined by the thermally activated surface diffusion processes. In Fig. 3.4 the

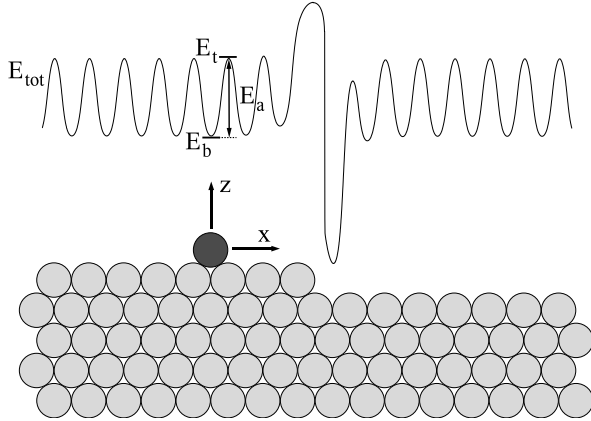


Figure 3.4: Potential energy surface of a test particle (dark) moving on the crystal surface. The shown surface is section of a larger system.

potential energy surface (PES) of an adatom on a triangular lattice is displayed. In order to obtain the PES a test particle is placed onto the crystal surface and the total potential energy is calculated according to Eq. (3.3). Now the total energy  $E_{tot}$  is minimized by varying the coordinates of all system particles. The only exception is the lateral coordinate of the test particle (marked as  $x$ -direction in Fig. 3.4) which is kept fix for each step, and the test particle is only allowed to relax in the plane perpendicular to the diffusion path. The system energy is recorded, the lateral coordinate is slightly increased and the whole procedure is repeatedly performed until the desired range of the PES is achieved.

### 3.3 Calculation of the activation energy

The following considerations refer again to the description on the triangular lattice. The modulation of the PES shown in Fig. 3.4 reveals that the particle has to overcome an energy barrier to reach the next binding site on the minimum energy path. The transition path connecting the initial and the final configuration of the particles, passes over a saddle point in the configuration space. The resulting activation energy  $E_a$  is given by the difference between the potential energy of the transition state  $E_t$  and the potential energy of the initial binding site  $E_b$ :

$$E_a = E_t - E_b \quad (3.8)$$

Due to the exponential nature governing the energy fluctuations, any event following another trajectory, with by definition an energy higher than at the saddle point, will be much less probable and can be neglected [102]. In order to get the correct rates for the diffusion process, which are necessary to understand the dynamical properties of the considered material, a precise determination of the activation energy is required.

Since the activation energy has to be calculated repeatedly for every possible diffusion process, the demanded computational effort is enormous, and the *frozen*

*crystal approximation* is applied as an important simplification when calculating the transition state energy and identifying possible diffusion sites. In this approximation, the positions of all particles, with the exception of the diffusing particle, are considered constant in the Molecular Static procedure. This restricts the accuracy of the method, but the energy barriers calculated within the frozen crystal approximation differ typically less than ten percent from the correct ones in the model, which was also confirmed in [103].

### 3.3.1 Determination of the neighboring binding site

Before calculating the activation energy for the diffusion processes, one has to determine possible free neighboring binding sites on which the regarded particle is supposed to jump. In contrast to lattice gas models, where particles occupy predefined lattice sites, in the off-lattice representation the binding sites can only be identified as local minima in the potential energy landscape. In the two dimensional representation one usually expects two neighboring binding sites for an isolated adatom.

For moderate values of the lattice mismatch between substrate and adsorbate, see Eq. (2.3), the rough position of the neighboring binding site can be guessed by geometrical considerations. Therefore it is indispensable to ensure that all possible diffusion scenarios (e.g. the interlayer diffusion on a sloped surface or the diffusion on the undersurface of overhangs) are taken into account and no important process is missing to avoid erroneous results, since the evolution of the morphology is mainly governed by the surface diffusion and the quality of the simulation is only as good as the quality of the input.

In the case of high values of the lattice misfit, this procedure can turn to be more sophisticated, especially in the local environment of misfit dislocations where the purely geometrical considerations are in need of sensible corrections assuring that the nearest local minimum is found. The rough position of the supposed free neighboring binding site then is determined in the frozen crystal approximation by means of *Brent's method*, a simple and fast minimization routine [101], ensuring that the detected position is a valid binding site. The precise position and therewith the precise binding energy of the destination site is not needed in order to calculate the activation energy. Since the system is relaxed before any diffusion step is performed, the binding energy  $E_b$  at the initial site is equivalent to the present binding energy and no further calculations are needed.

### 3.3.2 Calculation of the transition state energy

The potential energy surface in Fig. 3.4 shows the minimum energy path of a test particle moving on the surface. The transition state for a diffusion step can be identified as a maximum in this curve and is in the strict sense a first order saddle point (minimum in the  $z$ -direction, maximum in the  $x$ -direction).



The method used in the simulation for the calculation of the transition state energy is the so-called *activation-relaxation technique* (ART), originally applied with success to amorphous semiconductors and metallic glasses [104–106]. The ART consists of two parts: the activation from the local energy minimum to a nearby saddle point and the relaxation to the next local energy minimum.

In the simulation the determination of the saddle point is performed in the frozen crystal approximation with the following proceeding:

- In the first step, the particle is slightly displaced from the present local energy minimum towards the destination binding site, which was preliminary determined in section 3.3.1. This displacement leads to a force  $\vec{F}$  acting on the particle according to Eq. (3.2). The resulting displacement vector  $\vec{r}$  points from the last local minimum to the current position of the configuration.
- Now a force vector  $\vec{G}$  can be defined, opposite in sign to the force  $\vec{F}$  in the direction parallel to  $\vec{r}$  and equal to  $\vec{F}$  in any direction perpendicular to  $\vec{r}$ :

$$\vec{G} = \vec{F} - (1 + \alpha) (\vec{F} \cdot \vec{e}_r) \vec{e}_r \quad (3.9)$$

Here  $\vec{e}_r$  denotes the normalized vector parallel to  $\vec{r}$  and  $\alpha$  is a positive number serving as a control parameter.

- The force  $\vec{G}$  is applied iteratively on the particle which thereby is moved in small steps towards the nearby saddle point.
- At the saddle point, both  $\vec{G}$  and  $\vec{F}$  are zero and the iterative process stops.

The parameter  $\alpha$  controls the increment in each iteration step. A sensible value in the simulation turned out to be  $\alpha = 0.5$ , since too high chosen values of  $\alpha$  result in missing the correct saddle point and too small values slow down the saddle point determination due to too many iteration steps.

In principle the breakup condition  $\vec{G} = \vec{F} = 0$  is also fulfilled at an energy maximum, but the algorithm can only end up at a maximum, if it was already chosen as starting point. Including the knowledge of the initial and the final minimum site, the approximate position of the saddle point can be estimated and ending up at a maximum can be excluded.

The ART is a quite robust method and can be applied to three dimensional calculations as well as to the two dimensional description of epitaxial growth. In the latter case, the saddle point can be found by using a one dimensional minimization method [101], as the saddle point can be identified as a local maximum in the  $x$  direction when minimizing the same time in the perpendicular  $z$ -direction, referring to Fig. 3.4. This method is faster than the ART but also less stable and has to be applied more carefully and occasionally be replaced by the ART. At the saddle point, the transition state energy, needed for the activation energy, can be calculated.

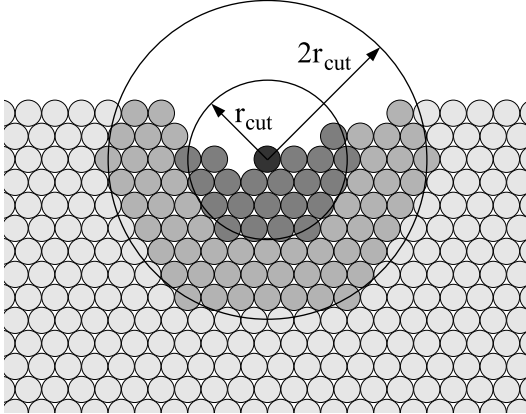


Figure 3.5: Local relaxation on a triangular lattice. The positions of all particles in the circle with radius  $r_{cut}$  are varied taking into consideration the information of all particles in the circle with radius  $2r_{cut}$ .

### 3.4 Local and global relaxation

After a particle has successfully overcome the diffusion barrier and reached its destination site, the whole environment of this particle is immediately affected by this change of the surface configuration. Since in the simulation the determination of the energy barrier was accomplished in the frozen crystal approximation, the hopping particle is put on its destination site without changing the position of any other system particle. As each particle position corresponds to a minimized potential energy, the rearrangement leads to slight deviation of the energy from its local minimum. In order to compensate for this effect and incorporate the deformation of the crystal correctly, after each step the system is relaxed by minimizing the total energy (3.3) by means of a conjugate gradient method [101].

The relaxation procedure of the crystal is performed locally after each event by varying the positions of all particles within a sphere of the cut-off radius  $r_{cut}$  around the hopped particle, which is therefore called *local relaxation*. To calculate the total potential energy, the information of all particles in the distance  $2r_{cut}$  is needed, see Fig 3.5. Since the used potentials are fast decreasing, this is a valid simplification which saves a lot of computer time.

In order to avoid artificial strain of the system, after a certain number of microscopic steps the energy is minimized with respect to the position of all system particles which shall be denoted as *global relaxation* and affects the entire system. The relaxation procedure only takes the energy of the system to its nearest local minimum without changing the crystal topology. The frequency of the global relaxation depends on the specific problem and on factors like misfit or system size and is adjusted by preliminary energetic considerations.

### 3.5 Downward funneling

After the deposition of a particle on the surface, the particle may still have enough kinetic energy to keep moving ballistically over the surface. This *transient*

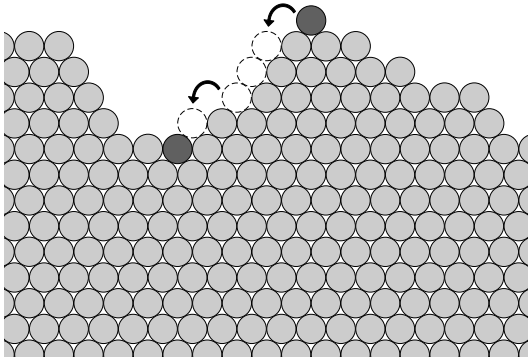


Figure 3.6: Illustration of the downward funneling effect: The newly deposited particle (dark) slides down to the lowest local position (dark) by successive jumps to lower neighboring sites (white) until no lower neighboring site is available.

*mobility* (see section 2.1.2) allows the particle to skip several lattice sites and bound up to a certain distance away from the point where it has impinged on the surface.

In the so called *downward funneling* mechanism the kinetic energy enables deposited particles landing on an inclined facet to slide down to the lowest position locally available, since the site with highest coordination is at the bottom of the facet. This mechanism and similar incorporation mechanisms which smoothen the surface morphology are discussed in [9] and can be included in the model as well.

In Fig. 3.6 the downward funneling is illustrated. A newly deposited particle on top of the mound jumps successively to the lower neighboring binding site until the lowest site is reached. If both the left and the right site are lower than the initial one, the lowest binding site is chosen. In the case of two equal low sites, the direction is chosen by random. Alternatively, it is possible to restrict the number of funneling steps. The restriction of the funneling steps to only one single step leads to the "knock out" effect in which the landing particle hits another at a terrace edge, pushes it aside and ends up inside the terrace.

## 3.6 Kinetic Monte Carlo simulation

After all relevant kinetic processes have been identified and the corresponding activation energy is used to calculate the transition rates following the Arrhenius law, Eq. (2.2), the time evolution of the system is described by means of a Kinetic Monte Carlo simulation. The dynamics is realized by choosing a possible event and then accepting or rejecting it with respect to the chosen acceptance probability. In the simulation of epitaxial growth, the acceptance probabilities for diffusion can become very small due the exponential decrease of the Arrhenius rates and a lot of computer time is lost by choosing rejected events. Especially for low temperatures and high barriers, the fraction of unaccepted events is high and most of the computer time is wasted without any change of the system.

### 3.6.1 Rejection-free method

A further way to realize the dynamics is to use the so-called *rejection free method* [73]. In this method, every Monte Carlo step leads to a change of the system and the pronounced problem of wasting computer time is avoided. The trick of this method is that the events are already chosen according to their probabilities and always performed, in contrast to the Metropolis algorithm where the probability of the event is included after the event is picked and one part of the events is rejected.

The probability of an event  $j$  is given by

$$p_j = \frac{R_j}{\sum_i R_i + R_d}, \quad (3.10)$$

depending on the diffusion rates  $R_i = \nu_0 e^{-\frac{E_{a,i}}{k_B T}}$ , with  $E_{a,i}$  as activation energy, and the deposition rate  $R_d = F L$ , where  $F$  is the particle flux and  $L$  the size of one monolayer of the system. For simplification, the attempt frequency is set to the constant value  $\nu_0 = 10^{12} s^{-1}$  for all processes.

The rejection-free method requires the knowledge of all currently possible events and an additional bookkeeping is needed. After any performed event, the rates of all affected particles have to be re-calculated and updated in the rate bookkeeping. The resulting extra computational effort is markedly small compared to the saved computer time due to no event rejection.

The sequence of events in the continuous time simulation form a Poisson process and the physical time  $\tau$  between two events is [107]

$$\tau = -\frac{\ln r}{\sum_i R_i + R_d} \quad (3.11)$$

with a uniformly distributed random number  $r \in ]0; 1]$ .

In the beginning of the simulation, the rates for possible diffusion events of all surface particles that are not completely incorporated in the bulk are determined. In the triangular lattice, this affects all particles with four or less nearest neighbors with the exception of substrate particles that are not allowed to diffuse but contribute to the potential energy surface.

In order to perform the random selection of the events, a fast method to apply the algorithm is needed. In the simulation, the list of the rates of all events is stored in a *complete binary tree* [73,108] which allows for fast access to its entries. A detailed implementation of a binary tree is described for instance in [20].

The simulation progress consists of the following steps:

1. An event  $j$  is drawn according to its probability (3.10) and performed.
2. The region of the crystal around this microscopic event is locally relaxed.

3. The system time is increased according to Eq. (3.11).
4. Relaxation of the whole system, if the global relaxation condition is fulfilled.
5. In the case of local relaxation, the rates of all affected particles (compare Fig. 3.5), in the case of global relaxation the rates of all adsorbate particles are re-calculated and the binary tree is updated.
6. Go back to iteration step 1 unless a stopping condition is fulfilled.

This proceeding was applied in all simulations of this work in order to describe the temporal evolution of heteroepitaxial growth systems. Additional to this progression, certain analyses and the evaluations of quantities, e.g. the surface width, were done during the simulation which enables also to describe the time evolution of these values.

### 3.6.2 Grid-based particle access method

A main part in the simulation of heteroepitaxial growth systems consisting of many particles is the calculation of the potential energy (3.3). Due to the surface diffusion and the energy relaxation procedure, the continuous positions of all particles change permanently and the set of particles contributing to the binding energy of one regarded particle changes throughout the simulation. In order to collect all particles within the cut-off distance  $r_{cut}$ , the distance of the regarded particle to all other particles of the system has to be calculated to check whether a non-vanishing contribution to the energy is delivered. This is the most often performed operation of the simulation, since it is needed to calculate the activation energy for diffusion, to find possible binding sites and transition states, and in the process of local and global relaxation.

A simple but also inefficient implementation is to pass through a list of all system particles and calculate each distance. Especially for larger systems a lot of computer time is wasted to calculate the distance to particles far away from the regarded adatom. Since this operation is repeated permanently, the simulation is slowed down needlessly.

Following the work by Vey [109], a grid-based particle access method is used. In this method, the whole system is divided into quadratic areas, called “boxes”, of the width  $r_{cut}$ . The grid in Fig. 3.7 represents the different areas on a triangular lattice. Every system particle is exactly in one of these areas, and with an additional bookkeeping the corresponding box of each particle is recorded. Now a list consisting of all particles that can be found in each box is made which needs to be updated whenever a particle’s position is changed. Since the width of the quadratic areas is chosen to be  $r_{cut}$ , only particles of the present box and its eight neighbor boxes (boxes within the red quadratic frame in Fig. 3.7) have to be taken into account when collecting all particles within the cut-off distance  $r_{cut}$ .

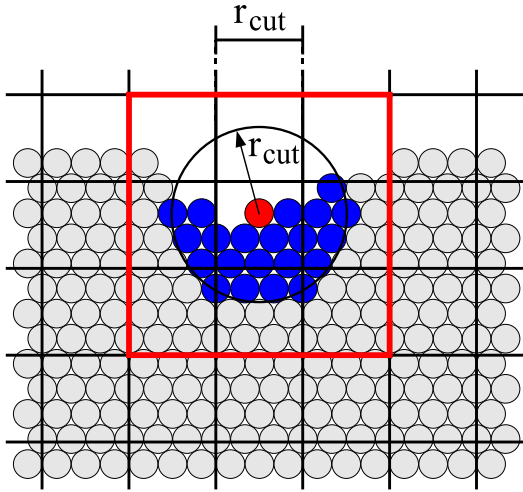


Figure 3.7: Grid on a triangular lattice. To collect all particles that are located in the circle with radius  $r_{cut}$  (blue) around the reference particle (red), only particles in the adjacent boxes (red frame) need to be taken into consideration.

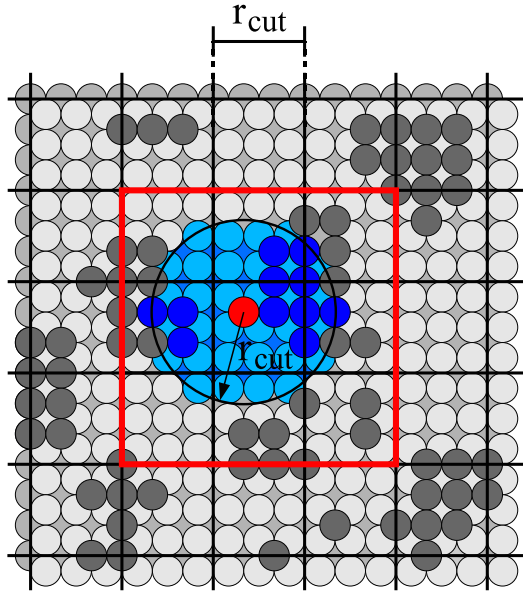


Figure 3.8: Grid on a bcc(100) surface. To collect all particles that are located in the circle with radius  $r_{cut}$  (blue coloring) around the reference particle (red), only particles in the adjacent boxes (red frame) need to be taken into consideration.

Instead of calculating the distance of a particle to all other system particles, it is sufficient to regard only particles of the same and of the neighboring boxes. This possible preselection accelerates the simulation enormously and outweighs clearly the computational effort needed for the additional bookkeeping as comparing simulations proved.

It is also possible to apply this grid-based method to the three dimensional lattice representation. In this case, the formerly quadratic two dimensional boxes are replaced by cuboids with quadratic base area. The division on a bcc lattice is illustrated in Fig 3.8 showing a top view of the (100) surface. All particles within the cut-off distance from the reference particle (red) are displayed in color. Again, only particles of the present box and its eight neighbor boxes (within the red frame) have to be taken into account when collecting all particles within

the cut-off distance  $r_{cut}$ . In contrast to the two dimensional system, the boxes here also consist of all particles in deeper layers. While the width of each box is chosen to be  $r_{cut}$ , the vertical size is given by the layer thickness. Since only growth in the submonolayer regime is regarded, the vertical system size is small compared to its lateral extension and the simulation is already accelerated at a system width of  $L = 4r_{cut}$  and outweighs the computational effort needed for the additional bookkeeping. Especially in three dimensions the main part of the time costing particle distance calculations is unneeded and can be avoided by the grid-based method whose application accelerates the whole simulation decisively.

## 3.7 Conclusions

In this chapter we have presented a simulation model which allows for Kinetic Monte Carlo simulations of heteroepitaxial growth systems. In contrast to many lattice gas models, our off-lattice model includes the possibility of particles leaving their predefined lattice sites. Our model does not aim at giving a detailed comparison to particular material systems, but heteroepitaxial growth is examined on a qualitative level.

In this work the simulation model is initially applied to the two dimensional triangular lattice and extended to three dimensions using the bcc lattice structure. For the temporal evolution of the system, realized by thermal activated surface diffusion processes, the precise calculation of the potential energy is indispensable for the determination of the activation energy of the corresponding kinetic process. The computational effort for the calculation of the saddle point energy as well as the total potential energy is enormous. Besides several simplifications, a grid-based method for faster particle access is implemented to save computer time.

In the following this model is used to study the influence of strain in heteroepitaxial growth systems with the aim to gain general insight in strain-related phenomena like the formation of misfit dislocations or the island growth as strain relaxation mechanisms.





## Chapter 4

# Formation and consequences of misfit dislocations

One of the central problems in material science is the growth and the stability of thin films in heteroepitaxial systems. One can often observe the emergence of misfit dislocations which affect many of the physical properties of the surface such as surface morphology, chemical reactivity, alloying properties and epitaxial growth. Improving the physical properties of heterostructures requires controlling the atomistic processes that are responsible for the generation of these defects. Understanding the atomistic mechanisms and how these dislocations form is thus of fundamental importance for further progress in the field of heteroepitaxial growth and structural control of nanostructures, since one is often interested in producing a smooth adsorbate film of a well-defined thickness on a given substrate. Besides the disastrous or destructive effect, dislocations can also have useful effects on devices and their performance and are therefore crucial for the device design. Buried dislocations produce a long-range elastic strain field which can be applied, for instance, in the concept of self-organization due to elastic strain [110].

Since experiments alone often cannot yield information about the exact origin of dislocation-related effects or about how to suppress unwanted or promote desired effects, computer simulations can help to interpret the experimental data. A lot of information about the nature of dislocations has been obtained within the continuum elastic theory, however the details of the underlying atomistic mechanisms through which dislocations occur is not delivered, since surface steps and surface roughness are not included but play an important role for the dislocation nucleation [111].

In this chapter different mechanisms of the dislocation formation and the resulting consequences on the lattice as well as the influence of the dislocations on the subsequent growth are presented.

## 4.1 Formation of misfit dislocations

In heteroepitaxial systems the substrate and the adsorbate material generally differ. In the conceptually simplest situation the adsorbate and the substrate crystallize in the same type of lattice with only slightly different lattice spacings. This relative difference of the lattice spacings can be characterized by the lattice misfit  $\varepsilon$ , see Eq. (2.3). For relatively low values of the misfit, the adsorbate grows pseudomorphically and the misfit can be accommodated by elastic strain, while the strain energy increases with the film thickness. Far away from the substrate, one expects that the substrate has no significant influence on the adsorbate and the adsorbate can grow with its own lattice constant. As a result, the strain of the system can be released by the formation of misfit dislocations above a critical adsorbate thickness  $h_c$ .

In the following simulations, the particle interaction is described by the Lennard-Jones 12-6 potential (cf. section 3.2 ) used in the form

$$U_{ij}(U_0, \sigma, r_{ij}) = 4 U_0 \left[ \left( \frac{\sigma}{r_{ij}} \right)^{12} - \left( \frac{\sigma}{r_{ij}} \right)^6 \right]. \quad (4.1)$$

The interaction of two substrate particles is given by  $U_{ij}(U_s, \sigma_s)$  and accordingly for two adsorbate particles by  $U_{ij}(U_a, \sigma_a)$ , with  $\sigma_a = \sigma_s (1 + \varepsilon)$ . To keep the number of parameters small, we set  $\sigma_s = 1$  and follow a standard approach by setting the interaction between substrate and adsorbate particles to  $U_{ij}(U_{as}, \sigma_{as})$ , with the geometric mean  $U_{as} = \sqrt{U_a U_s}$  and the arithmetic mean  $\sigma_{as} = (\sigma_s + \sigma_a) / 2$ .

In the following we set  $U_s = U_a = U_{as}$  which allows to isolate the influence of the misfit from energetic effects. To set the energy scale, the potential depth in the simulation is  $U_0 = 1.3125 \text{ eV}$  which leads to a diffusion barrier of about  $0.9 \text{ eV}$  for an isolated adsorbate particle on a plane substrate surface. Furthermore, the simulations were performed on the two dimensional triangular lattice with periodic boundary conditions in the direction parallel to the film-substrate interface. While the system has a lateral extension of a few hundred lattice spacings, the substrate consists of at least eight monolayers with three fix bottom layers stabilizing the crystal. This allows for the simulation of a semi-infinite substrate, since the cut-off distance is chosen to be  $r_{cut} = 3 r_0$  which prevents that particles feel the bottom edge of the system. If not explicitly stated, the temperature is set to  $T = 450 \text{ K}$  and the flux to  $F = 1.0 \text{ MLs}^{-1}$ .

### 4.1.1 Mechanisms of dislocation formation

The mechanisms of the misfit dislocation formation depend mainly on the sign and the magnitude of the misfit, but also on the surface topology and cannot be understood by purely energetic arguments, since it is a kinetic process. In this section, a detailed description of the different observed dislocation nucleation mechanisms will be given.

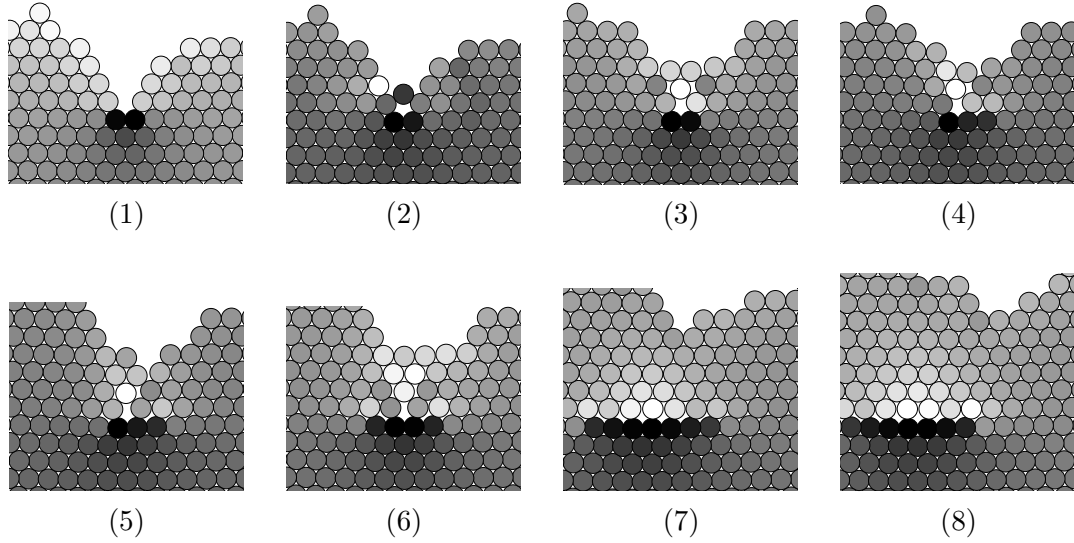


Figure 4.1: The formation of a dislocation simulated with positive misfit  $\varepsilon = +3.0\%$ . This sequence of snapshots shows the temporal evolution of a section of a larger system. The grey level of a particle indicates the average distance to its nearest neighbors. The lighter a particle is drawn, the larger this distance is.

### Positive misfit

For positive misfit less than about  $\varepsilon \approx +3.0\%$ , the adsorbate initially grows coherently with the substrate. Above a critical film thickness  $h_c$ , the formation of misfit dislocations becomes energetically more favorable than a purely strained, pseudomorphic grown adsorbate film.

The mechanism of an evolving dislocation is exemplarily shown in Fig. 4.1. The grey level of the particles just indicates the average distance of a particle to its neighbors. The lighter a particle is drawn, the larger the average distance to its neighbors is. The grey level of a given particle changes during the simulation, since also the relative particle distances change when distorting the surface; and the grey level only reflects the relative distance of a particle compared to all other system particles and does not refer to an absolute distance and only serves as a tool to reveal the strain distribution of the system. Due to the Ehrlich-Schwoebel effect, the diffusing particles on top of islands tend to form mounds instead of growing layer-by-layer [19, 112]. At the critical adsorbate height, the lateral distance between two neighboring mounds is not large enough to allow a further particle in between (1). Hence, the additional particle between the two mounds is dislocated from the supposed lattice position (2). This position is now seed for the emerging dislocation and is finally overgrown by further adsorbate material, by both deposition and diffusion.

For higher values of positive misfit, the dislocation formation mechanism is

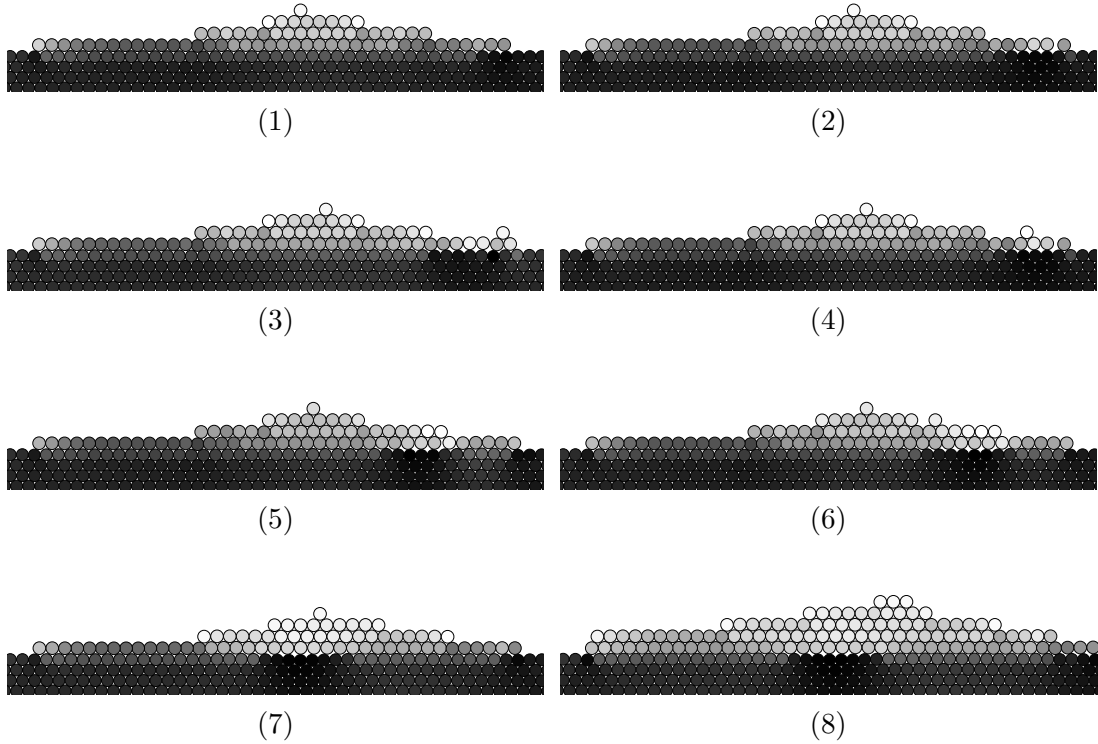


Figure 4.2: The formation of a dislocation simulated with positive misfit  $\varepsilon = +8.0\%$ . This sequence of snapshots shows the temporal evolution of a section of a larger system. The grey level of a particle indicates the average distance to its nearest neighbors. The lighter a particle is drawn, the larger this distance is.

principally the same. The only difference is that no initial pseudomorphic growth takes place and the dislocations are built direct on the substrate-adsorbate interface.

The formation mechanism of the dislocation depends not only on the misfit but also on the surface morphology, as it can be seen in the scenario of Fig. 4.1, where the two neighboring mounds are origin of the dislocation nucleation. In the case of low particle fluxes, a different formation mechanism can be observed. In the initial state of growth in the submonolayer regime, the mean distance of islands increases with increasing temperature or decreasing particle flux. Fig. 4.2 shows the evolution of a system with misfit  $\varepsilon = +8.0\%$  and particle flux  $F = 0.001 MLs^{-1}$ .

The low particle flux leads to submonolayer islands of large lateral size, one of them is shown in image (1). Due to the high value of misfit, dislocations are expected to be formed direct on the substrate-adsorbate interface. Since no adjacent island or mound can serve as seed for a misfit dislocation, the adsorbate island is very strained. The binding energy of an edge particle decreases with

increasing lateral island size and the particle can easily detach.

In image (2) the right edge particle has detached from the island by hopping to the neighboring free binding site, but still has strong influence on the island. As a result, the new island edge particle and its left neighboring particle are clearly dislocated from their supposed lattice site. The distance of the detached particle from the dislocated island edge particle is only small and a newly deposited adsorbate particle connects the formerly detached particle again with the island. The whole ends up in a misfit dislocation close to the island edge, displayed in image (3). Since the particles of the dislocation have the same lateral position as the nearest underlying substrate layer, their positions are only metastable and the diffusion of the latest deposited particle towards the island center affects the lateral position of the dislocation which glides along the substrate-adsorbate interface, see panels (4) and (5). The diffusing particle is part of the local environment of the dislocation and any change of the topology leads to a force acting on the dislocation. This results in the dislocation glide, since the affected particles can move rather easily by breaking and forming new bonds in the glide plane [28]. This dislocation glide can also be observed experimentally [29, 113].

In the further temporal evolution of the system, the dislocation keeps the lateral position of the adsorbate mound grown on it. By the deposition of further adsorbate material, the influence of the surface diffusion on the dislocation decreases due to the increasing vertical distance to the dislocation.

The number of dislocations that are necessary to relief the strain caused by the lattice mismatch increases with the misfit and the mean distance between dislocations is close to  $1/\varepsilon$  which reflects the relative periodicity of the substrate and adsorbate lattice [19]. In the simulation the mechanism of dislocation formation at the island edge, with a following dislocation glide towards the island center, is observed for high values of positive misfit in systems with initial dislocation free islands of lateral size significantly higher than the expected mean dislocation distance  $1/\varepsilon$ .

## Negative misfit

If the lattice constant of the adsorbate is smaller than the substrate's lattice constant, the strain in the adsorbate film is tensile and the observed mechanisms of misfit dislocation formation are different. In the case of negative misfit, the dislocations are formed by two different mechanisms.

For high values of negative misfit, like  $|\varepsilon| \gtrsim 8\%$ , the dislocations are formed direct on the substrate, in analogy to the case of high positive misfit. This behavior is shown for a system with misfit  $\varepsilon = -11.0\%$  in Fig. 4.3. Again, two neighboring mounds of adsorbate are seed for a new emerging dislocation. On panel (1) one can see two resulting gaps between the bottom edge particles of the central and the two adjacent mounds. In order to approach the relaxed undisturbed bulk structure, the particles forming the adsorbate mounds are slightly

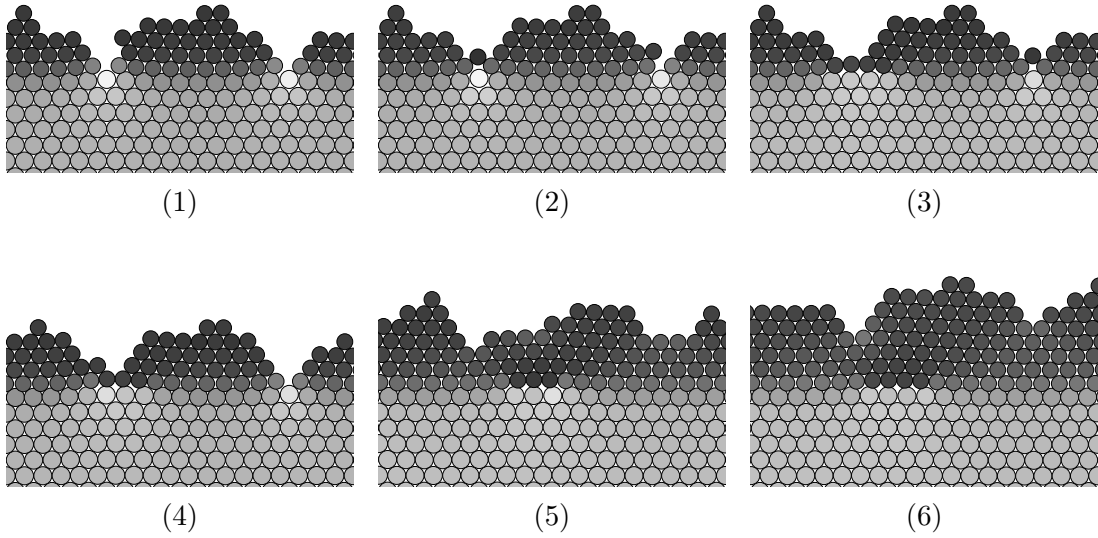


Figure 4.3: The formation of a dislocation simulated with a negative misfit  $\varepsilon = -11.0\%$ . This sequence of snapshots shows the temporal evolution of a section of a larger system. The grey level of a particle indicates the average distance to its nearest neighbors. The lighter a particle is drawn, the larger this distance is.

dislocated from the supposed lattice positions which are given by the underlying substrate lattice structure. The bottom edge particle is attracted by the rest of the mound particles which are laterally dislocated towards the mound center, due to the high tensile strain. This explains the resulting gap in the middle of the mounds.

The left gap enables the particle diffusing on the left slope of the central mound to move in between, as displayed in panel (2). Note that before the diffusing particle has filled this gap, the second gap on the right side of the central mound can serve as seed of an emerging dislocation as well. The following panels document the overgrowing of this dislocation by further adsorbate material.

For lower values of negative misfit, like  $|\varepsilon| \lesssim 6\%$ , the adsorbate initially grows coherently with the substrate until a dislocation appears to release the strain. The mechanism of the dislocation formation is different now, as it can be seen in Fig. 4.4 for a system with misfit  $\varepsilon = -4.5\%$ , whose substrate film consists of the ten bottom layers. To avoid overhangs when growing a thicker adsorbate film, in this particular simulation the mechanism of downward funneling (section 3.5) was implemented.

In contrast to the case of positive misfit, in the pseudomorphic growth with negative misfit the mean distance of the adsorbate particles to their nearest neighbors is increased, compared to their undisturbed bulk lattice constant. Therefore, the adsorbate particles can react more flexibly on changes in the surface topology by slight changes in their positions without reaching the strong repulsive range of

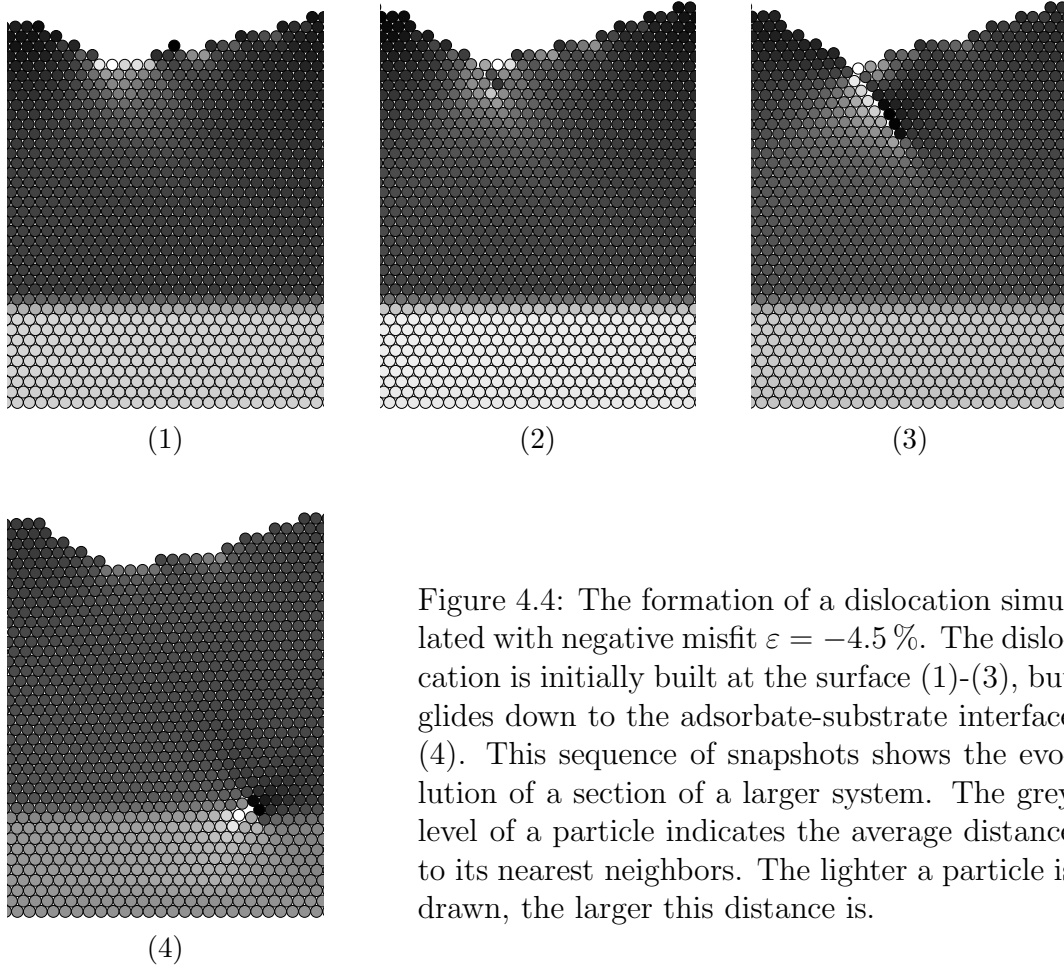


Figure 4.4: The formation of a dislocation simulated with negative misfit  $\varepsilon = -4.5\%$ . The dislocation is initially built at the surface (1)-(3), but glides down to the adsorbate-substrate interface (4). This sequence of snapshots shows the evolution of a section of a larger system. The grey level of a particle indicates the average distance to its nearest neighbors. The lighter a particle is drawn, the larger this distance is.

the interaction potential. Initially, the mean distance of the adsorbate particles directly between the two vicinal mounds is increased, indicated by their lighter color in the first image of Fig. 4.4. Due to further deposition of adsorbate particles and changes in the surface topology via surface diffusion, some particles are slightly dislocated from the perfect lattice structure (2).

In the further development of the system, particles in deeper layers are affected and a gliding dislocation extended about several monolayers emerges (3). This configuration of the system is only metastable and just due to further rearrangements of the surface, more and more particles are involved by this gliding dislocation and the system finally ends up with a dislocation direct on the substrate-adsorbate interface caused by two groups of particles sliding relative to each other.

The concerted motion of a relatively large number of atoms is the reaction of the metastable system to one thermally activated surface diffusion process and leads to insertion of an extra lattice row into an already continuous film. This

stable configuration is shown in Fig. 4.4, panel (4). The lateral position of such a dislocation is determined by the dislocation nucleation at the surface and does not show any periodicity, in contrast to the dislocations formed at the adsorbate-substrate interface in the case of high values of misfit. The corresponding Burgers vector of the dislocation formed in this way is not parallel to the interface and thus only part of the Burgers vector contributes to the strain relaxation. In the simulation often a second dislocation is formed at a  $60^\circ$  angle from that of the dislocation formed earlier. The Burgers circuit enclosing both dislocations yields a Burgers vector parallel to the interface.

Summarized, we can observe two principle different mechanisms of dislocation formation, depending on the magnitude of the negative misfit. The transition between both mechanisms is continuous, as the dislocation formation with misfit  $\varepsilon = -8.0\%$  in Fig. 4.5 shows. Again, the lateral spacings of the particles between the mounds are larger than particles part of the mounds which again leads to a gliding dislocation, see panel (4). This configuration is metastable and ends up in the stable configuration shown in panel (5). Compared to the dislocation nucleation shown in Fig. 4.4, the initial dislocation free adsorbate film only consists of few layers. Within the same simulation run of this system dislocations formed by the overgrowing mechanism, shown in Fig. 4.3, can be observed as well. The concrete mechanism for intermediate values of the misfit depends on the present local topology and the surface kinetics.

The different mechanisms of the dislocation formation presented in this section are qualitatively in good agreement with the results obtained in molecular dynamics simulations [111]. The mechanism of dislocation nucleation is different in tension and compression and associated with the surface roughness.

### 4.1.2 Behavior of the lattice spacings

The different lattice constants of the substrate and the adsorbate material affect the lattice spacing of the growing adsorbate film in heteroepitaxial growth systems. In pseudomorphic growth, the adsorbate grows coherently with the lateral lattice spacing of the substrate. If the lattice misfit is chosen to be positive, the adsorbate film is compressed in lateral direction and the vertical lattice spacing is shifted to higher values in order to reach the equilibrium distance given by the potential. The expected distance  $\Delta$  between two adsorbate layers is illustrated in Fig. 4.6. While the lateral distance  $r_0$  is the lattice constant of the substrate, the preferred distance of two particles of different layers is  $r_0(1 + \varepsilon)$ . A simple geometric consideration leads to a vertical lattice spacing

$$\Delta = r_0 \sqrt{\varepsilon^2 + 2\varepsilon + \frac{3}{4}}. \quad (4.2)$$

This calculated shift can be observed in our simulation as well. To this end, some layers of adsorbate material are grown pseudomorphically on a system con-



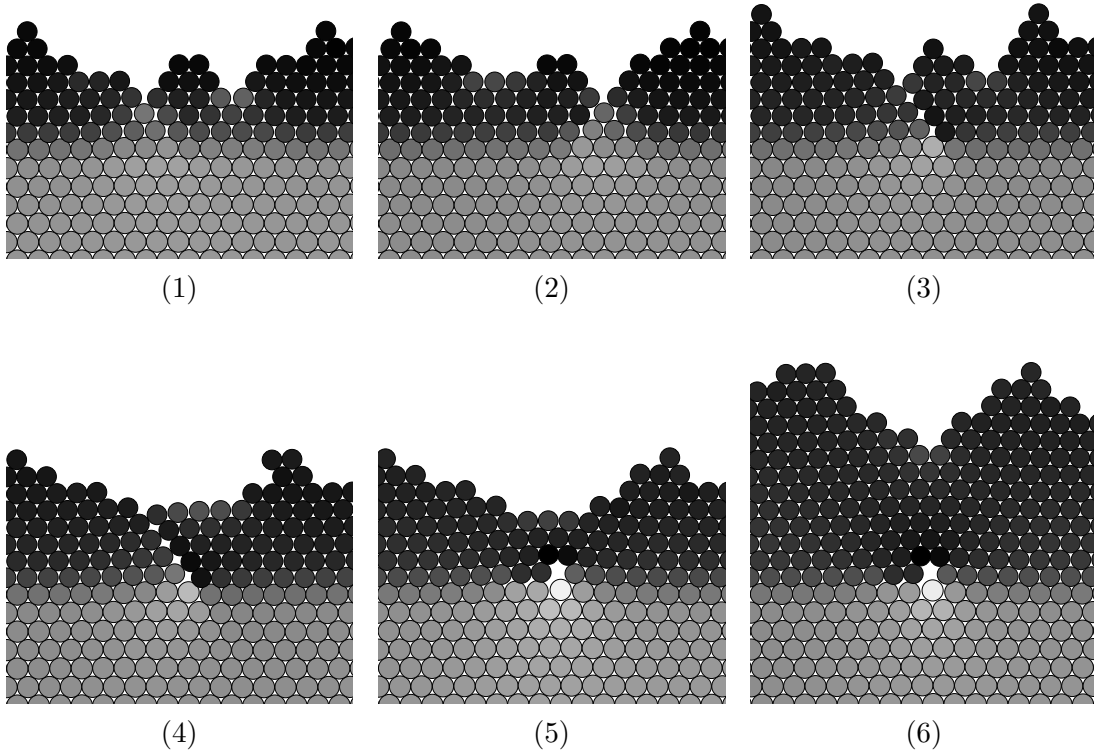


Figure 4.5: The formation of a dislocation simulated with negative misfit  $\varepsilon = -8.0\%$ . This sequence of snapshots shows the temporal evolution of a section of a larger system. The grey level of a particle indicates the average distance to its nearest neighbors. The lighter a particle is drawn, the larger this distance is.

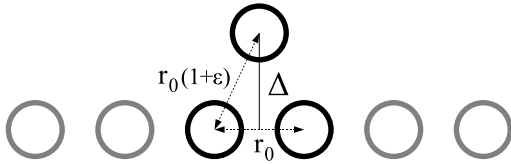


Figure 4.6: Illustration of the distance  $\Delta$  between a particle and the underlying compressed layer. The lateral distance is the substrate's equilibrium distance  $r_0$ .

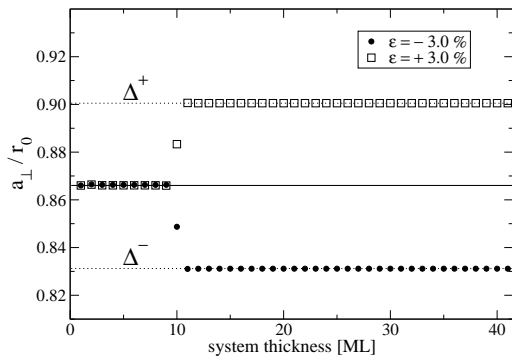


Figure 4.7: Development of the vertical lattice spacing with shift to  $a_{\perp} = \Delta^+$  for positive misfit and to  $a_{\perp} = \Delta^-$  for negative misfit, with  $|\varepsilon| = 3\%$ . The dotted line corresponds to the value calculated with Eq. (4.2). The substrate consists of the first ten layers.

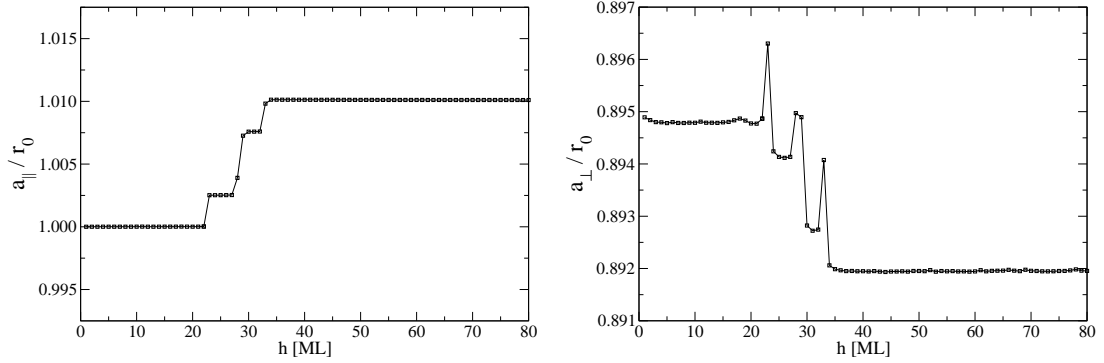


Figure 4.8: Development of the lateral lattice spacing  $a_{\parallel}$  and the vertical lattice spacing  $a_{\perp}$  as a function of the adsorbate film thickness  $h$  for positive misfit  $\varepsilon = +2.5\%$  and system size  $L = 400$ . The data results from a single simulation.

sisting of ten substrate monolayers. The system size was set  $L = 100$  which is sufficient for this comparison. In Fig. 4.7 the value calculated according to Eq. (4.2) is compared with a single simulation for negative and positive misfit. Here,  $a_{\perp}$  describes the vertical lattice spacing between two subsequent layers in units of the substrate's equilibrium distance  $r_0$ .

In the simulation, the vertical lattice spacing is calculated by taking the mean vertical distance of each particle to its closest neighbors in the next layer at the given thickness. In this case, only particles of one single layer close to the surface are taken into account. Accordingly, the lateral lattice spacing is the mean distance of each particle of this layer to its next neighbors in the same layer. As expected, the substrate is not much affected by the adsorbate film and the curve progression of  $a_{\perp}$  in the substrate for positive and negative misfit essentially coincide. The vertical lattice spacing of the first adsorbate layer to the adjacent top substrate layer can be seen as an intermediate case, since the equilibrium distance for the mixed interaction is the arithmetic mean and therefore lies in between. The adsorbate then grows coherently with the vertical lattice spacing  $a_{\perp} = \Delta^+$  in the case of positive and  $a_{\perp} = \Delta^-$  in the case of negative misfit.

At the critical thickness, the system starts to release the strain by introducing misfit dislocations after which for positive misfit the number of particles in one monolayer is reduced and the mean lateral distance is increased. Therefore the shift of the lateral lattice spacing is reduced and the adsorbate approaches its relaxed undisturbed bulk structure. Fig. 4.8 displays the development of the vertical and the lateral lattice spacings for a single system of size  $L = 400$ . The determination of the lattice spacing was always done during the growth simulation with downward funneling and the displayed values show the lattice spacings close to the surface as a function of the present adsorbate height. The value of each single shift which is caused by one single dislocation depends on the system size as it is averaged over all particles in one layer.

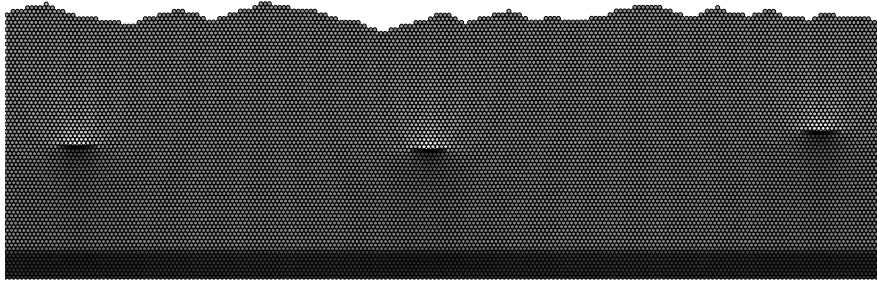


Figure 4.9: Section of the same system as in Figure 4.8 showing three dislocations. The first eight bottom layers represent the substrate.

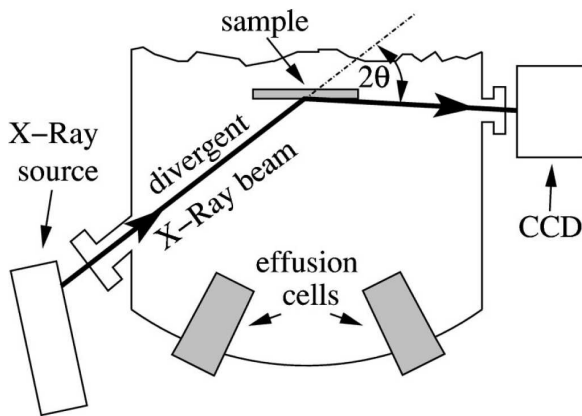


Figure 4.10: Experimental setup for RIX consisting of a conventional MBE chamber and x-ray source, providing divergent x-rays, and a CCD camera. The picture is taken from [114].

The increased value of the vertical lattice spacing  $a_{\perp}$  right before the sudden descent can be explained by the particles forming the dislocation. Here, two adsorbate particles of two successive layers have the same lateral position which results in an additional shift to a local vertical distance  $\tilde{\Delta} = r_0(1 + \varepsilon) > \Delta$ . The concurrent appearance of several dislocations at the critical adsorbate film thickness can be seen in the curves as close successive jumps. A look at a section of this simulated surface, shown in Fig. 4.9, reveals the emergence of several misfit dislocations within few adsorbate layers indicating the critical adsorbate height.

In experimental studies it has become possible to measure the vertical lattice spacings averaged over the whole adsorbate film during MBE growth by means of real-time in situ x-ray diffraction (RIX) [114]. In conventional methods the x-ray diffraction requires an extremely exact sample adjustment and an angular scan by rotating the sample and the detector which can last up to several minutes and does not allow for real-time monitoring. In this method, this inconvenience is circumvented by using a slightly divergent x-ray beam and observing an extremely asymmetric Bragg reflection leading to an exposure time of only few seconds which enables monitoring the epitaxial growth process, see Fig. 4.10.

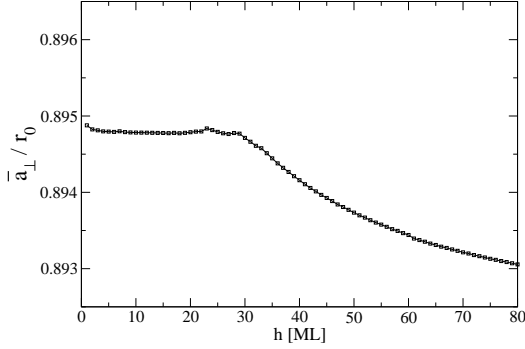


Figure 4.11: Development of the average vertical lattice spacing  $\bar{a}_\perp$  as a function of the adsorbate film thickness  $h$ . The data results from the same single simulation shown in Fig. 4.9 and Fig. 4.8.

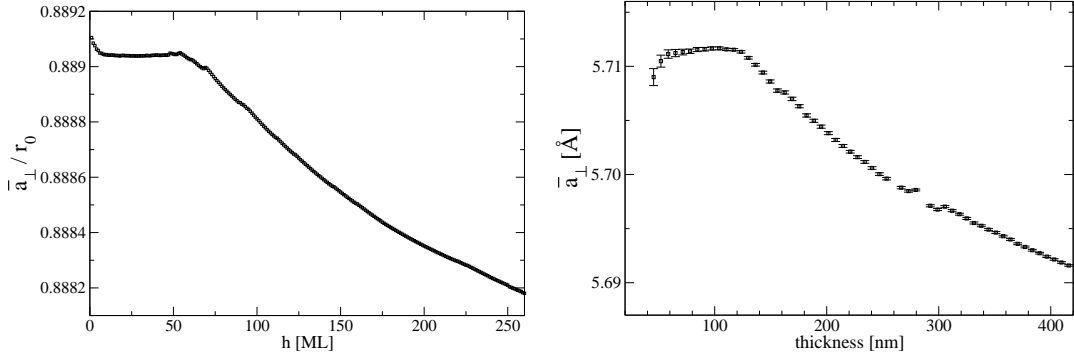


Figure 4.12: Development of the average vertical lattice spacing  $\bar{a}_\perp$  as a function of the adsorbate film thickness. The left curve results from KMC simulation with misfit  $\varepsilon = +2.0\%$ , averaged over 10 independent runs, the right shows experimental data of a ZnSe/GaAs system ( $\varepsilon \approx 0.31\%$ ), data taken from [114].

In the simulation, the average vertical lattice spacing  $\bar{a}_\perp$  is obtained by calculating the mean vertical distance of all adsorbate particles to their closest neighbors of the next layer, in contrast to the vertical lattice spacing  $a_\perp$ , where only particles of one single layer are considered. The average vertical lattice spacing  $\bar{a}_\perp$  for the same single simulation discussed above is displayed in Fig. 4.11. A qualitative comparison of the development of  $\bar{a}_\perp$  measured in experiment and obtained by simulations is displayed in Figure 4.12. The experimental curve results from epitaxial growth of a ZnSe epilayer on (001)GaAs which leads to a lattice misfit about  $\varepsilon \approx 0.31\%$ . The simulation results and the experimental findings are in good qualitative agreement.

In the pseudomorphic growth,  $\bar{a}_\perp$  keeps constant which can be identified as the plateau in the beginning of the growth. An occurring dislocation does not affect the mean particle distances of the already grown adsorbate film in a significant way. Since  $\bar{a}_\perp$  is averaged over the whole film it decreases slowly towards the undisturbed bulk value.

As discussed in the previous section for small negative misfits, dislocations formed at the surface glide down immediately to the substrate-adsorbate inter-

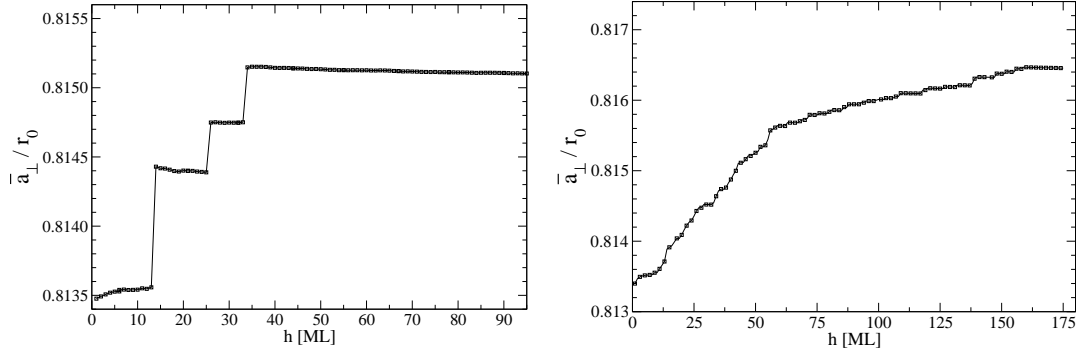


Figure 4.13: Development of the average vertical lattice spacing  $\bar{a}_{\perp}$  as a function of the adsorbate film thickness  $h$ . The misfit is  $\varepsilon = -4.5\%$  and the system size  $L = 400$ . The data is obtained by a single simulation run (left), and averaged over 20 independent runs (right).

face. Therefore, the whole adsorbate film is affected and a sudden change of  $\bar{a}_{\perp}$  can be expected. This expectation is confirmed by the simulation and shown in Figure 4.13. The curve for the single simulation run is discontinuous, since the lattice spacings of all adsorbate particles are affected by such a gliding dislocation which can be identified by the jumps in the curve. In addition, the right panel shows the progression averaged over 20 independent simulation runs which is approximately continuous and can be related to larger systems as well as to the expected experimental result.

## 4.2 Influence of buried dislocations

At the critical thickness, the strain is released by the formation of misfit dislocations. Due to the ongoing particle flux, more and more adsorbate material is deposited and the formed dislocations are totally overgrown. These buried dislocations still have influence on the subsequent growth, since they induce a periodic long-range elastic strain field at the free surface which can be applied for instance in the concept of self-organization. Here it is desired to produce large quantities of nanostructures in a controlled manner as it does not have the limitation of lithography. Without any lateral correlation, the fundamental limit is the random character of the nucleation of islands on the surface.

### 4.2.1 Positive misfit

To study the influence of buried dislocations on a quantitative level, all particles of a grown system are removed down to a certain film height above the dislocations yielding a flat surface. The potential energy surface, obtained within the frozen

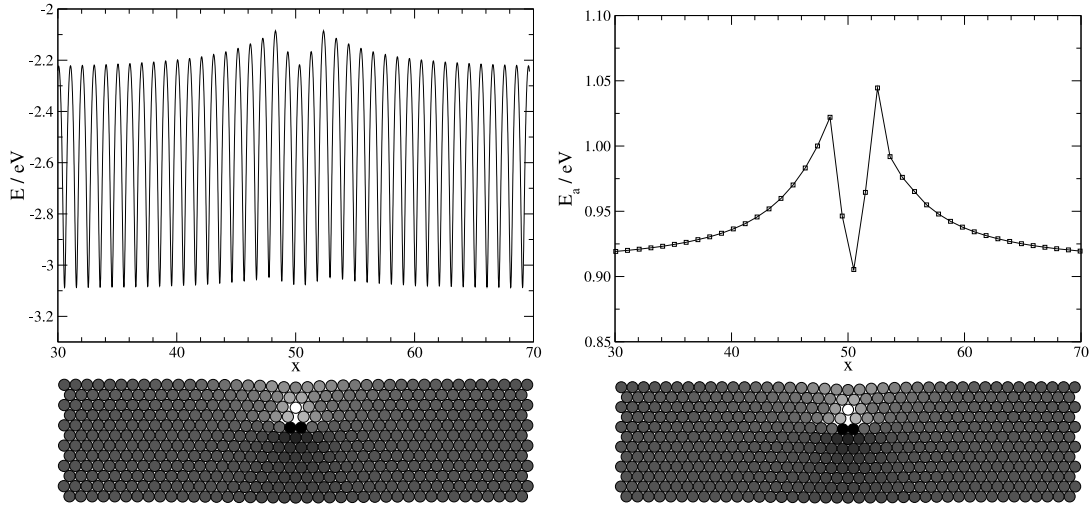


Figure 4.14: Potential energy surface of an adatom moving along the surface (left panel), and diffusion barrier  $E_a$  for particle jumps to the right at the lateral position  $x$  (right panel). Each corresponding section of a flattened system with misfit  $\varepsilon = +2.5\%$  shows the detailed position of its dislocation.

crystal approximation by moving a test particle on the flattened surface, is shown on the left panel of Fig. 4.14 for a system with positive misfit  $\varepsilon = +2.5\%$ .

The curve progression reveals a clear influence of the buried dislocation on the diffusion on top of the flattened surface. Its modulation is such that the transition state energies for particle hops toward the dislocation increase. Only right above the dislocation and, in this example situation, at the left and right neighbor sites the transition state energy is lowered.

The modulation of the potential energy surface also reveals a variation of the binding energy, but its magnitude is distinctly smaller, thus the diffusion barrier mainly depends on the transition energy variation. Consequently, in the vicinity of its lateral position the dislocation has mainly a repulsive influence on diffusing adatoms on the surface. This is confirmed by a look at the diffusion barrier for particle jumps to the right in the vicinity of the buried dislocation, shown on the right panel of Fig. 4.14. The closer a particle approaches the lateral position of the dislocation, the higher the necessary activation energy is. The converse effect arises if the particle moves away from the dislocation. As a consequence, the particles tend to move away from the dislocation. Only within a small range direct above the dislocation it has an attractive effect on diffusing particles.

The modulation of the diffusion barrier depends on the thickness of the adsorbate film above the dislocation. In Fig 4.15 the diffusion barrier for jumps to the right neighboring site is compared for several adsorbate film thicknesses above the dislocation. Firstly, we observe that the intensity of the modulation caused by the dislocation decreases with increasing film thickness. Secondly, the

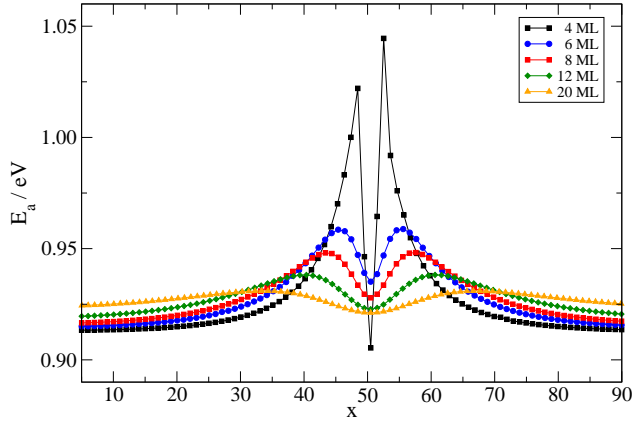


Figure 4.15: Activation energy for diffusion steps to the next right neighboring site on a flattened surface for different adsorbate film thicknesses above the dislocation at  $x = 50$ . The misfit of the system is  $\varepsilon = +2.5\%$ .

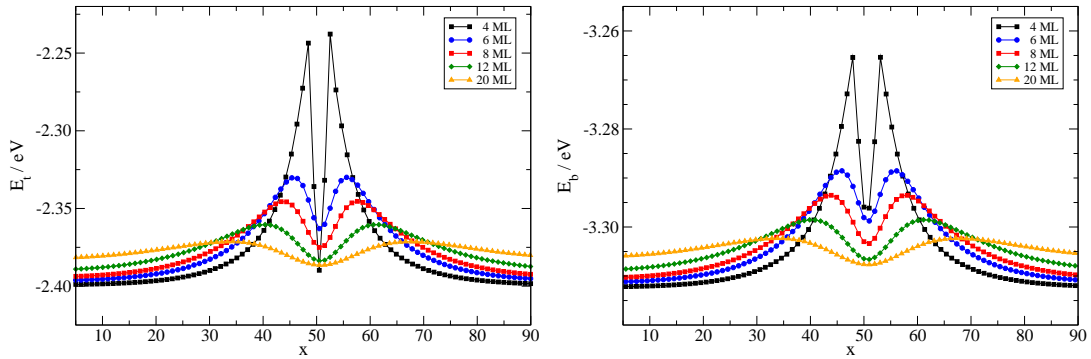


Figure 4.16: Transition state energy (left) and binding energy (right) on a flattened surface for different adsorbate film thicknesses above the dislocation at  $x = 50$ . The misfit of the system is  $\varepsilon = +2.5\%$ .

attractive range direct above the dislocation increases in the lateral direction with increasing film thickness. In order to fathom the origin of the diffusion barrier modulation, the according transition state energy  $E_t$  and the binding energy  $E_b$  modulation is shown in Fig. 4.16. Both curves have similar qualitative progression, but the variation amplitude of the binding energy is lower and therefore the diffusion barrier is dominated by the transition state energy.

In systems with higher misfit, several dislocations emerge at the critical film thickness and a diffusing particle is influenced by every dislocation in its environment. To analyze the interplay of these dislocations, a system with misfit  $\varepsilon = +5.0\%$  is grown and flattened at different adsorbate thicknesses. Due to the high value of the misfit, all dislocations are formed direct on the substrate-adsorbate interface ensuring that they have the same height and additionally a small and periodic lateral distance which leads to a regular modulation of the potential energy surface.

As one can see in Figure 4.17, showing a section of a larger system, the initial repulsive character of a single dislocation changes after few layers of adsorbate. The superposition of the contributions of all dislocations to the potential energy

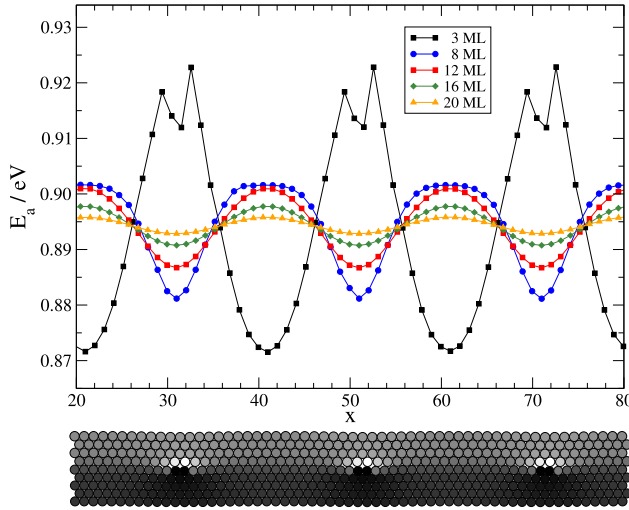


Figure 4.17: Activation energy for diffusion steps to the next right neighboring site on a flattened surface for different values of the adsorbate film thickness. The misfit of the system is  $\varepsilon = +5.0\%$ .

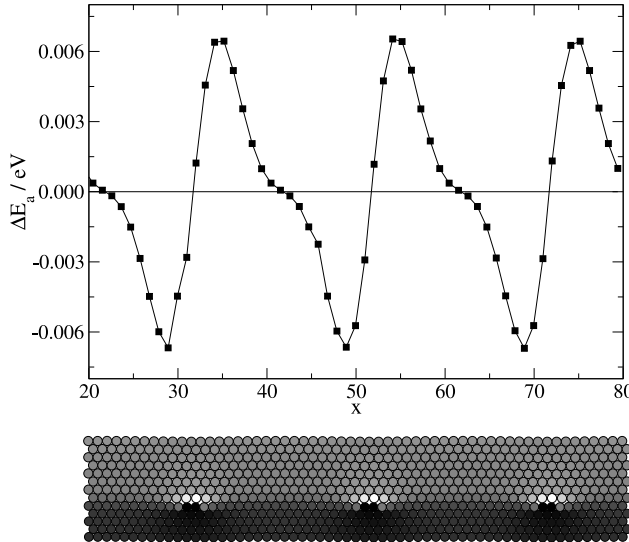


Figure 4.18: Difference of the activation energy for diffusion steps to the next right and left neighboring site on a flattened surface at an adsorbate film thickness  $h = 8 ML$ . The misfit of the system is  $\varepsilon = +5.0\%$ .

surface leads to a diffusion bias towards the lateral positions of the dislocations above about seven monolayers. This is confirmed by Fig. 4.18 showing the difference of the diffusion barrier for a jump to the right and to the left neighboring site against the lateral position of the surface particle for an adsorbate film thickness  $h = 8 ML$ . Right above the dislocations and exactly in between two dislocations this difference vanishes, which one would expect due to symmetry reasons. In all other cases the sign of the difference is such that diffusion towards the lateral position of the dislocation is favored.

The magnitude of the barrier difference is relatively small and the modulation of the diffusion barriers caused by buried dislocations dominates the lateral position of growing mounds for not too high temperatures and particle fluxes. This effect can be seen in the simulation if one grows adsorbate material on an initially flattened surface with an underlying dislocation network. The required



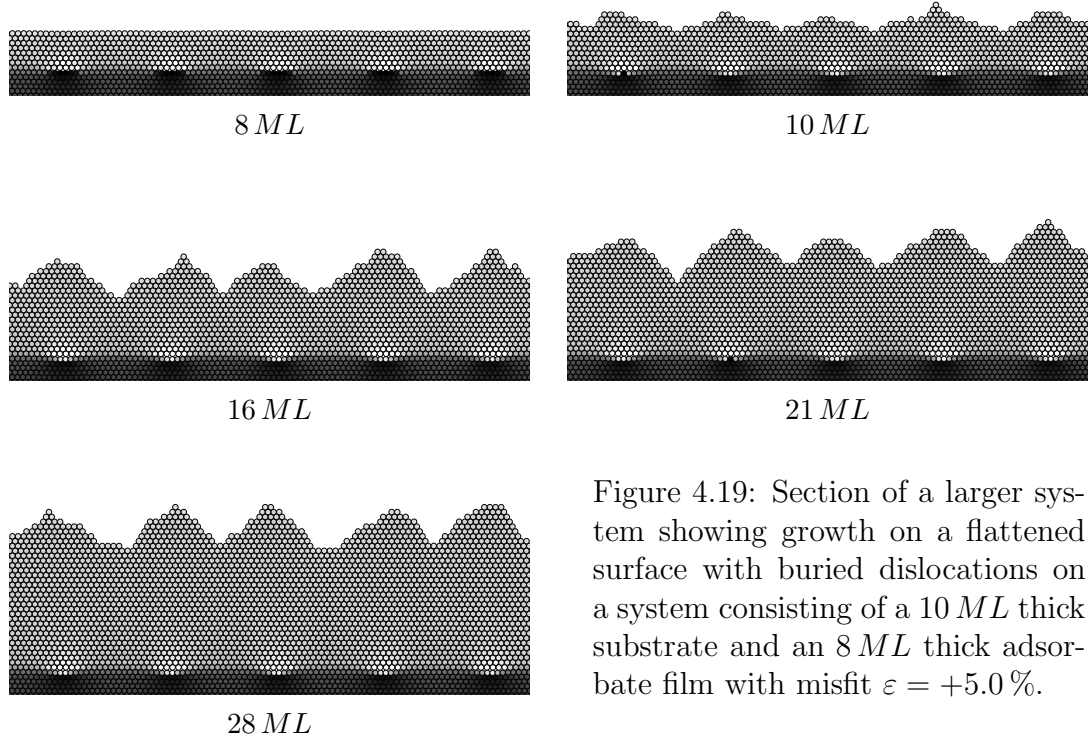


Figure 4.19: Section of a larger system showing growth on a flattened surface with buried dislocations on a system consisting of a 10 *ML* thick substrate and an 8 *ML* thick adsorbate film with misfit  $\varepsilon = +5.0\%$ .

growth conditions are a small particle flux and a low substrate temperature. Fig. 4.19 shows the temporal evolution of a system simulated with misfit  $\varepsilon = +5.0\%$ , substrate temperature  $T = 340\text{ K}$  and particle flux  $F = 1.0 \times 10^{-5} \text{ MLs}^{-1}$ . The preceding simulation delivering the network of buried dislocations was performed under equal growth conditions. Apart from statistical fluctuations, the correlation between the lateral position of the dislocations and the grown mounds is clearly apparent in the simulations up to several layers of deposited adsorbate material.

### 4.2.2 Negative misfit

In the case of negative misfit, the dislocations have the reverse influence on diffusing adatoms. The potential energy surface of test particle obtained within the frozen crystal approximation on a flattened surface is shown in Fig. 4.20 for a system with negative misfit  $\varepsilon = -8.0\%$  and eight monolayers of adsorbate material.

Again, the curve progression reveals a clear influence of the buried dislocation on the diffusion on top of the flattened surface. Its modulation is such that the transition state energies for particle hops toward the dislocation increase and reach a maximum right above the dislocation. Again, the variation of the binding energy shows the same qualitative behavior, but less intense and the diffusion barrier mainly depends on the transition state energy. The closer a

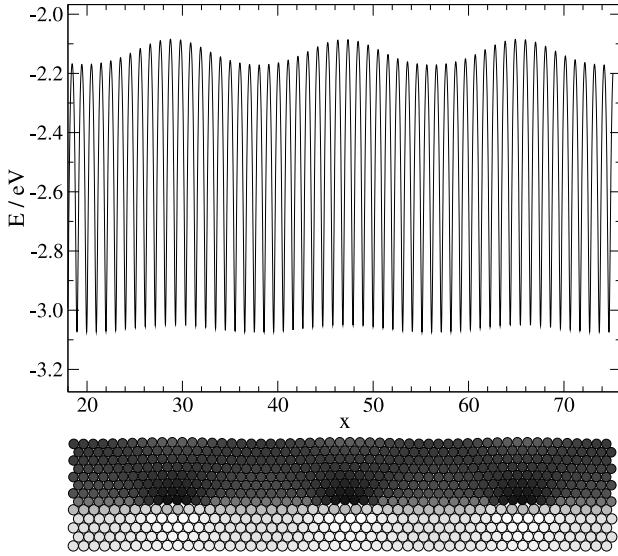


Figure 4.20: Potential energy surface of an adatom moving along the surface. The corresponding section of a flattened system with misfit  $\varepsilon = -8.0\%$  at an adsorbate film thickness  $h = 8 ML$  shows the detailed position of its dislocations.

particle approaches the lateral position of the dislocation, the higher the necessary activation energy is, while the converse effect arises, if the particle moves away from the dislocation. The dislocations are repulsive for diffusing adatoms on the surface and the particles preferably diffuse to lateral positions between the dislocations that are again located direct on the substrate.

The modulation of the diffusion barrier depends again on the thickness of the adsorbate film above the dislocation. In Fig 4.21 the diffusion barrier for jumps to the right neighboring site is compared for several adsorbate film heights. As expected, the intensity of the modulation caused by the dislocation decreases with increasing film thickness. At the dislocations' lateral positions the diffusion barrier is increased for all adsorbate film thicknesses. In the first few adsorbate layers an additional maximum of the activation energy can be observed in between two dislocations whose intensity decreases fast with the adsorbate film thickness and turns to be a minimum for thicker films.

The difference of the diffusion barrier for a jump to the right and to the left neighboring site against the lateral position of the surface particle is displayed in Fig. 4.22 for an adsorbate film thickness  $h = 8 ML$ . In the same manner as in the case of positive misfit, one can see that right above the dislocations and exactly in between two dislocations this difference vanishes due to symmetry reasons. In all other cases the sign of the difference is such that diffusion to lateral positions between dislocations is favored.

Again, the magnitude of the barrier difference is relatively small and the modulation of the diffusion barriers caused by buried dislocations dominates the lateral position of growing mounds at only low substrate temperatures and particle fluxes. According to the case of positive misfit, this effect can be seen in the simulation, if one grows adsorbate material on an initially flattened surface with a network of buried dislocations requiring a small particle flux and a low sub-

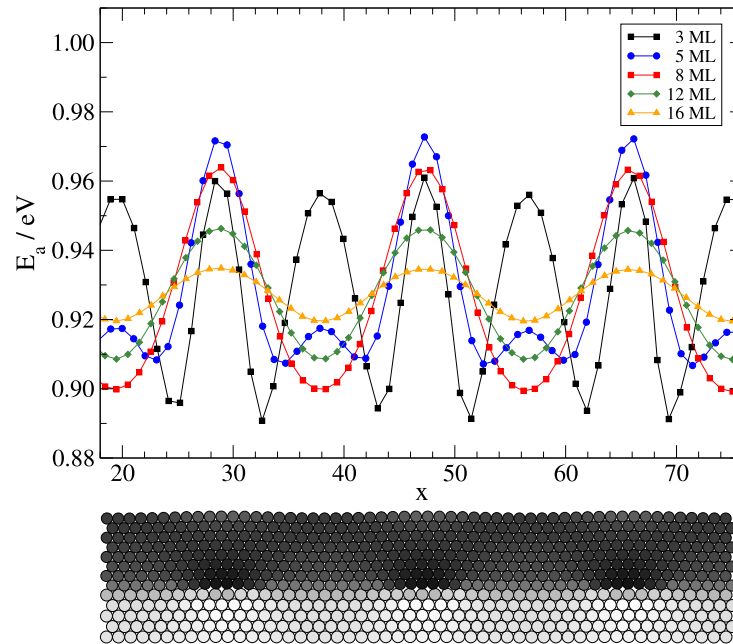


Figure 4.21: Activation energy for diffusion steps to the next right neighboring site on a flattened surface for different values of the adsorbate film thickness. The misfit of the system is  $\varepsilon = -8.0\%$ .

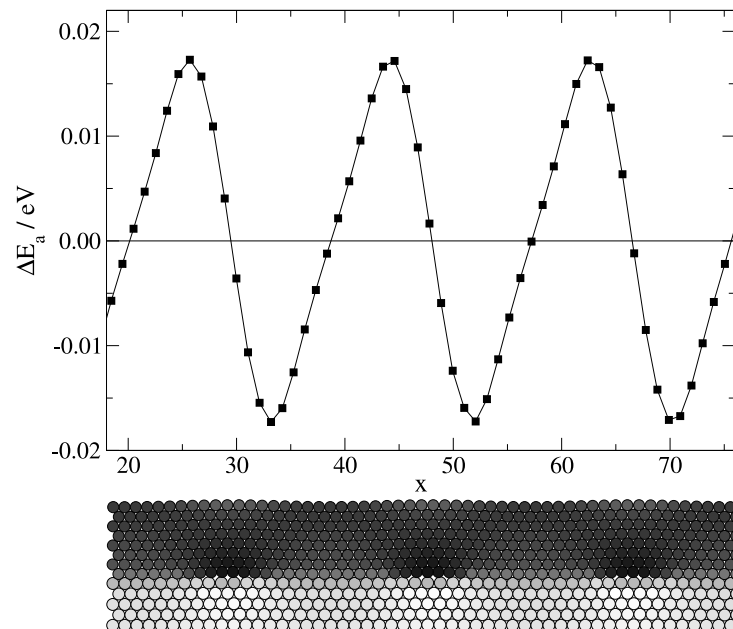


Figure 4.22: Difference of the activation energy for diffusion steps to the next right and left neighboring site on a flattened surface at an adsorbate film thickness  $h = 8 ML$ . The misfit of the system is  $\varepsilon = -8.0\%$ .

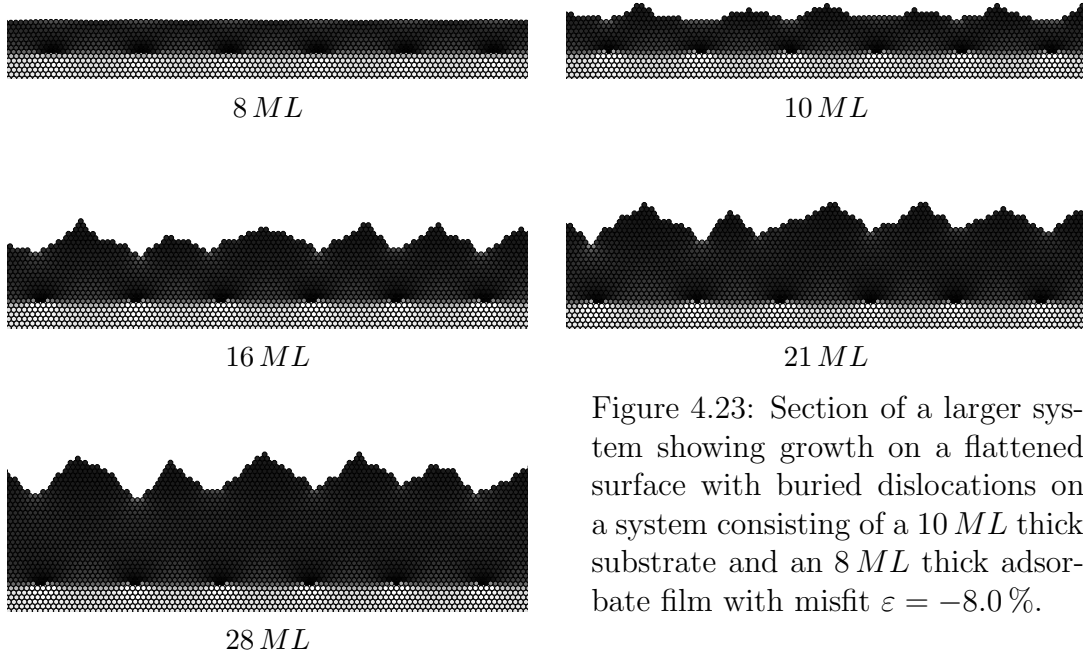


Figure 4.23: Section of a larger system showing growth on a flattened surface with buried dislocations on a system consisting of a 10  $ML$  thick substrate and an 8  $ML$  thick adsorbate film with misfit  $\varepsilon = -8.0\%$ .

strate temperature as growth conditions. Fig. 4.23 shows the temporal evolution of a system simulated with misfit  $\varepsilon = -8.0\%$ , substrate temperature  $T = 340 K$  and particle flux  $F = 1.0 \times 10^{-5} MLs^{-1}$ . The preceding simulation delivering the network of buried dislocations was performed under equal growth conditions. Apart from statistical fluctuations, the correlation between the lateral position of the dislocations and the grown mounds is clearly apparent in the simulations up to several layers of deposited adsorbate material.

### 4.3 Conclusions

In summary, we have analyzed the different mechanisms of the formation of misfit dislocations on the triangular two dimensional lattice. In the initial phase, one observes a pseudomorphic growth up to a critical thickness of the adsorbate film. The formation of dislocations depends strongly on the sign and the magnitude of the misfit. For positive misfit, the dislocations nucleate between two adjacent mounds and keep their vertical positions after they are built.

In addition, we have seen that the concrete mechanism also depends on the present local topology and the surface kinetics, since in the case of low particle flux and high misfit the dislocations can also nucleate at the edge of extended islands. This state is only metastable and the dislocation can glide laterally, induced by surface diffusion of particles on top of the island. The dislocation finally ends up at the lateral position of an existing mound, where the influence of the surface diffusion on the dislocation is negligibly small, due to the increased distance, and the particles of the mound stabilize the lateral position.

For high values of negative misfit, the observed mechanism is comparable to the case of positive misfit and the formation of dislocation is favored by the presence of mounds. In the case of small values of negative misfit, we can observe a different mechanism. Here, the dislocations are initially formed at the surface, but glide down to the substrate-adsorbate interface by the concerted motion of a large number of atoms leading to insertion of an extra lattice row into an already continuous film. The transition between these two observed mechanisms turned out to be continuous.

The tensile-compressive asymmetry originates from the strong anharmonicity of the interaction potential, particularly in the steeply rising repulsive core. An asymmetric behavior of positive and negative misfit is observed for example in [115].

Furthermore, we have seen that the dislocations affect the vertical and the lateral lattice spacings of the system. The average vertical lattice spacing approaches continuously the undisturbed bulk value when the misfit is positive. This observation is in qualitative agreement with experimental data. For negative misfit, however, the average vertical lattice spacing approaches the bulk adsorbate value in a discontinuous manner, since dislocations glide down to the adsorbate-substrate interface immediately after their nucleation. However, by averaging over many simulation runs, the influence of a single dislocation is reduced and the behavior is approximately continuous and can be related to larger systems as well as to the expected experimental result.

As a further result, we have shown that the dislocations also affect the subsequent growth of the film. We observe a clear correlation between the lateral positions of buried dislocations and the positions of mounds grown on the surface. The correlation depends decisively on the sign of the misfit. The interplay of the regularly arranged dislocations leads to a periodic modulation of the potential energy surface.

In the case of positive misfit, the mounds are preferentially formed laterally direct above buried dislocations whereas for negative misfit mounds grow between the lateral positions of the dislocations. The clear correlation of buried dislocations and nucleation of islands is subject of many other theoretical and experimental investigations [110, 116–120] and can find application in the idea of self-organization of nanopatterns or quantum dots whose periodicity is controlled by the underlying dislocation network, since the dislocations quite often arrange into highly ordered periodic patterns. The optimal growth temperature is crucial, since the self-organization can be destroyed at too high temperatures.



# Chapter 5

## Simulation of the three different growth modes

In the last chapter, we have investigated the formation of misfit dislocations as a strain relaxation mechanism as well as the resulting consequences on the further growth progression. The introduction of such lattice defects dominates the strain relaxation in sufficiently thick films.

However, the strain, caused by the lattice mismatch of the adsorbate and the substrate material, can also be relieved by the formation of three-dimensional islands which enables the particles to approach their preferred lattice spacing. The term island is commonly used to indicate spatial separated structures, in contrast to mounds that are formed due to the Ehrlich-Schwoebel instability. Whether coherently strained islands are observed prior to dislocation formation depends on the ratio between change in surface energy due to island formation and the energy of the dislocated interface [36].

Similar to the idea of self-organization of nanopatterns controlled by an underlying dislocation network, the tendency to form ordered arrays of strain-induced three dimensional grown islands can be applied in the concept of self-organized pattern formation as well. The strain-driven surface structures attracted researchers' interest because of their frequently shown uniformity. The formation of growth structures with a narrow size distribution is referred to as self-assembly and, if these structures in addition show the tendency to form ordered arrays, this process is called self-organization. The term self-organization in a strict sense is reserved to kinetically driven spontaneous ordering.

The nanoscale coherent islands, arranged in a regular array, are accompanied by a spatial quantization of electrons and holes in three dimensions and are promising for use in quantum dot light-emitting diodes (LEDs) and lasers. The shape, size and thickness distribution of small clusters are important parameters for efficient operation. Thus, to obtain the controllable shape and size of nanocrystals, it is necessary to study growth mechanisms such as growth mode and island evolution. The formation of dislocations, driven by strain relaxation

in mismatched systems, is a critical concern for nanocrystal applications, because it is related to carrier processes in nanocrystals.

In section 2.3 the epitaxial growth modes based on thermodynamic considerations are classified and distinguished according to the balance between the surface free energy of the adsorbate, the surface free energy of the substrate and the interface free energy. While in the *Frank–van der Merwe* growth mode the adsorbate grows layer-by-layer, in the *Volmer–Weber* growth mode three-dimensional adsorbate islands grow direct on the substrate. The *Stranski–Krastanov* growth mode can be seen as the intermediate case, where three-dimensional islands are formed on top of a wetting layer.

As epitaxial growth is per definition a non-equilibrium process determined by kinetic phenomena, growth morphologies will deviate more or less from the thermodynamic picture and metastable growth modes are possible. Keeping in mind that in the strict sense these equilibrium considerations can not be applied to MBE, we use the classification of growth modes in order to characterize the growing surface and distinguish between the different growth behaviors. The growth mode actually occurring in the growing system depends on the particular interaction potential as well as on the lattice mismatch between the adsorbate and the substrate material.

The interplay of the substrate-adsorbate interaction and the lattice misfit plays an important role in the simulation of the three epitaxial growth modes. In this chapter, the growth conditions and parameter settings leading to each growth mode are investigated.

## 5.1 Simulation model

In conformance with the last chapter, all following simulations were performed on the two dimensional triangular lattice with periodic boundary conditions in the direction parallel to the film-substrate interface, using the simulation model introduced in chapter 3. The system has a lateral extension of a few hundred lattice spacings and the substrate consists of 10 monolayers with three fix bottom layers stabilizing the crystal.

The pairwise interaction between the system particles is now described by the Morse potential, see Eq. (A.4). For faster calculations, it can be written in the form

$$U_{ij}(U_0, \sigma, r_{ij}) = U_0 e^{-a(r_{ij}-\sigma)} (e^{-a(r_{ij}-\sigma)} - 2), \quad (5.1)$$

depending on the distance  $r_{ij}$  of the two interacting particles  $i$  and  $j$ , where again  $U_0$  denotes the depth of the potential and the equilibrium distance between two isolated particles becomes  $r_0 = \sigma$ . The control parameter is set to  $a = 6.0$  yielding a fast decreasing potential with a steep attractive and a repulsive contribution which thus allows to set the cut-off distance to  $r_{cut} = 2.5 r_0$ . Due to the steep progression of the potential, slight deviations of the particle distance from the



exact potential minimum position lead to pronounced changes in the binding energy. Thus, the lattice misfit has strong influence on the potential energy.

The chosen form of the potential has the additional advantage that the resulting Ehrlich-Schwoebel barrier is comparably small and the effect of strain-induced island formation is not affected significantly by the Ehrlich-Schwoebel barrier and no further adjustment like removing the Schwoebel barrier by hand, proposed e.g. in [96, 121], is necessary.

To set the energy scale, in the following simulations the depth of the potential describing the adsorbate-adsorbate interaction is set to  $U_a = 0.5 \text{ eV}$ . An important parameter is the potential depth  $U_{as}$ , characterizing the adsorbate-substrate interaction, whose variation has decisive influence on the arising growth mode. The potential depth of interacting substrate particles is chosen to be the maximum of  $U_{as}$  and  $U_a$ ,

$$U_s = \max(U_{as}, U_a), \quad (5.2)$$

ensuring the stability of the substrate film and also justifying the simplification that substrate particles are not allowed to diffuse. Besides this condition, the exact choice of the substrate interaction strength  $U_s$  is of secondary importance, since the relation between  $U_{as}$  and  $U_a$  has the main influence on the appearing type of island growth mode. The parameter  $\sigma_{as}$  again is set to  $\sigma_{as} = (\sigma_a + \sigma_s)/2$  and  $\sigma_s = 1$ .

## The surface width

A useful tool to characterize the surface morphology of the epitaxially grown surface and to identify the occurring growth mode is the surface width  $w$ , also called roughness, which is defined as the root mean square deviation in the surface height  $h(x)$ :

$$w = \sqrt{\langle (h(x) - \langle h(x) \rangle)^2 \rangle}. \quad (5.3)$$

The averaging in the surface width (5.3) is generally done over the surface lattice sites at the lateral position  $x$ . To define the height  $h(x)$  on the triangular lattice, the crystal is divided into  $L$  columns perpendicular to the substrate-adsorbate interface, where  $L$  is the lateral system size and denotes the number of substrate particles in each monolayer. In the strict sense, the adsorbate particles are not exactly on lattice sites, since we have an off-lattice model. Nevertheless, the lateral positions of the rigid substrate atoms of the bottom layers can serve as reference sites, since the misfit is limited to values  $\varepsilon \ll 1$  and small deviations do not have notable influence.

The lateral position  $x$  of each column can then be assigned to one site of the according reference lattice and be written as  $x = na$ . While  $a$  represents the substrate lattice constant,  $n$  is an integer number with  $n \in [1; L]$ . The stacking of the triangular lattice is *ABAB*, which leads to  $2L$  possible lateral on-lattice particle positions depending on the present monolayer height, and one can

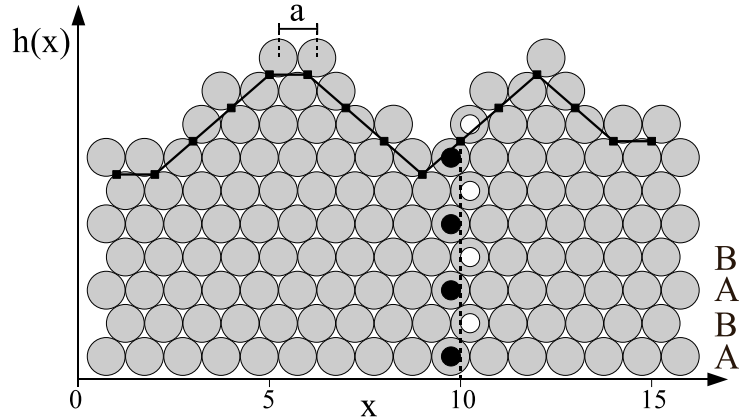


Figure 5.1: Example for the height definition on the triangular lattice. At  $x = 10$ , in units of the substrate lattice spacing  $a$ , the value of  $h(x)$  is the mean height of the two neighboring sub columns, which are marked with white and black circles. The continuous line connects the single determined values of  $h(x)$ , marked by black squares.

define  $2L$  “sub columns”. To determine the height  $h(x)$  of the  $L$  columns, two neighboring sub columns are combined and the resulting height  $h(x)$  is given by the mean height of these two sub columns. The height of each sub column is given by the highest vertical position of all particles with lateral position  $x = (n \pm 1/4)a$ . This definition of the height was proposed e.g. in [122] and is illustrated in Fig. 5.1.

In the presence of overhangs or voids, a further definition of the height besides this maximum definition is possible, but the concrete height definition does not influence the scaling behavior. Since overhangs and voids are rare in our simulation of island growth, and the surface width is mainly used to identify the growth mode, the maximum height definition is sufficient.

## 5.2 Influence of the misfit on submonolayer islands

Besides the potential depth  $U_{as}$  of the mixed interaction, the misfit  $\varepsilon$  plays an important role in the occurrence of island growth. A submonolayer island with a given lateral extension is strained due to the lattice mismatch of the adsorbate and the substrate material. In the absence of misfit dislocations, the system achieves lower energy if the adsorbate atoms form islands, within which they reside close to the potential well minima, caused by the underlying substrate, and the misfit is accommodated mainly by the compression or expansion of the inter-atomic spacings at the island edges. Thus, the strain built up in the islands

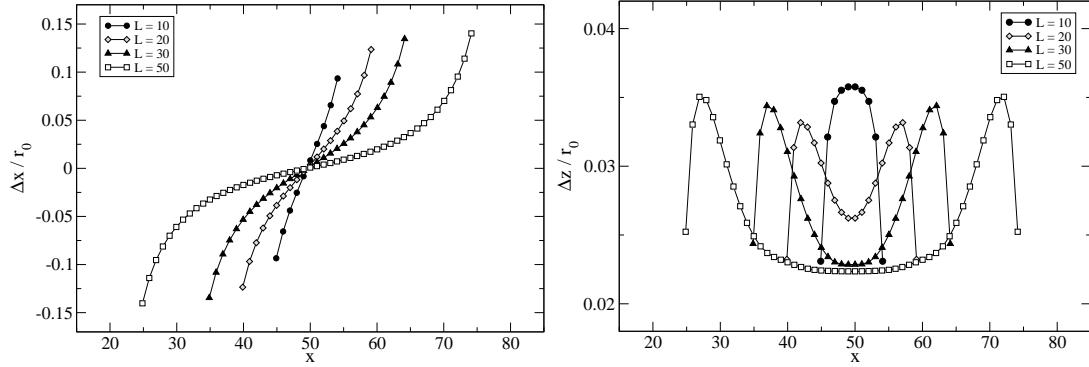


Figure 5.2: Displacement from the potential well minima position, caused by the underlying substrate, in lateral ( $\Delta x$ ) and vertical direction ( $\Delta z$ ) as a function of the lateral monolayer island size  $L$  with misfit  $\varepsilon = 4.0\%$ .

is released at the island edges. This effect is often observed at domain boundaries, which are called *light walls*, if the adsorbate density is lower than that within the domain, and *heavy walls* in the opposite case [10, 123].

To study the strain behavior by dint of our simulation model, a submonolayer island of adsorbate material is placed on top of a 10 layer thick substrate film and the system energy is minimized to its next local minimum. In order to isolate the influence of the misfit from energetic effects, we set  $U_a = U_{as} = U_s = 0.5 eV$ .

The displacement of the island particles from the potential well minima, caused by the underlying substrate, is plotted in Fig. 5.2 as a function of the island size for a system with positive misfit  $\varepsilon = 4.0\%$ . While the particles in the center of the island are blocked up in the lateral direction and change their lateral positions only slightly, the strain is released by the lateral displacement of the particles close to the island edge. The only possibility of a central particle is adjusting its position in the vertical direction, which is shifted to higher values in the case of small island sizes, e. g.  $L = 10$ . Since the outermost edge particles are displaced in the lateral direction, their vertical displacement is decreased.

The mobility of the island center particles is restrained and decreases with increasing island size. Thus, the displacement decreases in lateral as well as in vertical direction. Consequently, the binding energy of each island particle is affected as well and decreases with increasing island size. In Fig. 5.3 the binding energy distribution of island particles is shown for several island sizes for a system with misfit  $\varepsilon = 4.0\%$ . Again, one can see two trends: Firstly, the larger the submonolayer island is, the weaker the particles are bound. Secondly, particles closer to the island edge are bound stronger. This is confirmed by a look at the binding energy of the edge particle, shown in Fig. 5.4 for different values of the misfit. In the absence of misfit, the bond of the edge particle is independent of the island size, which confirms the expectation. In the presence of misfit, the strength of the bond decreases with increasing island size and increasing misfit.

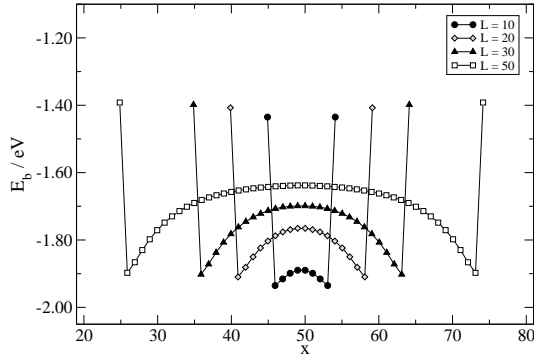


Figure 5.3: Binding energy distribution of island particles at the lateral position  $x$  for different island sizes  $L$  and misfit  $\varepsilon = 4.0\%$ .

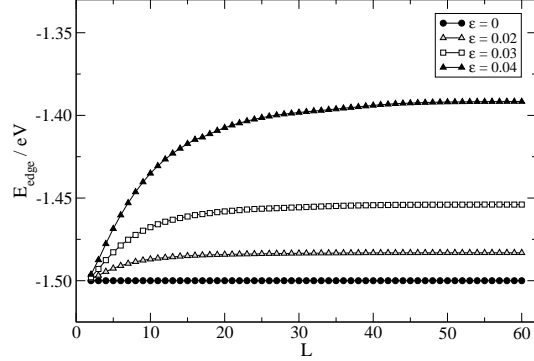


Figure 5.4: Binding energy of island edge particle as a function of the lateral island size  $L$  for different values of the misfit  $\varepsilon$ .

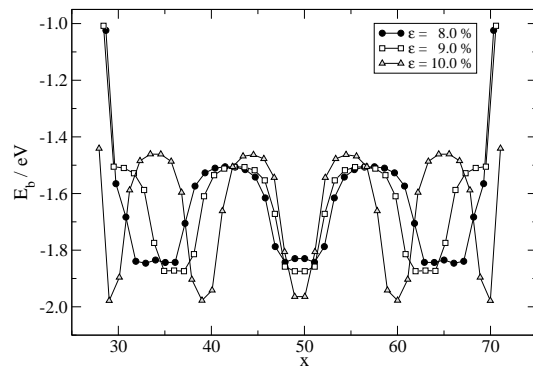
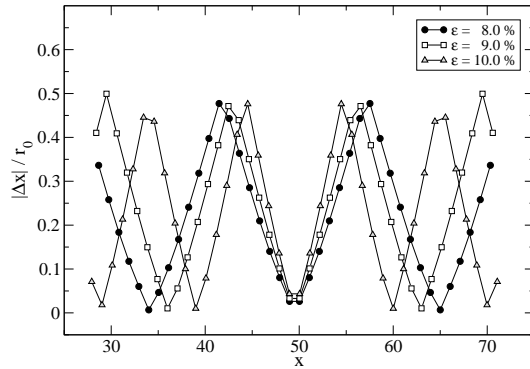


Figure 5.5: Lateral displacement from the potential well minima position (left) and binding energy distribution of island particles (right) as a function of the lateral position  $x$  for different values of the misfit  $\varepsilon$ . The island size is  $L = 40$ .

Thus, the probability to detach from a submonolayer island is strongly influenced by the misfit which therefore plays an important role in the growth of islands as a strain relaxation mechanism.

For high values of misfit ( $\varepsilon \gtrsim 5\%$ ), the relaxation of the prepared submonolayer island leads to misfit dislocations and the resulting lateral displacement of the island particles and their according binding energies, shown in Fig. 5.5, take approximately the expected periodicity of the distance  $d$  between misfit dislocations, see Eq. (2.4) in section 2.2. This is in conformance with the model proposed by Frenkel and Kontorova. The small deviations from this expected distance result from the missing rigidity of the substrate film which is deformed by the interaction with the adsorbate and prevents the formation of misfit dislocations for lower values of  $\varepsilon$ .

## 5.3 Volmer–Weber-like growth

In the Volmer–Weber (VW) growth mode, adsorbate particles are more strongly bound to each other than to substrate particles and the energy balance requires to minimize the area covered by the adsorbate material. As a consequence, the adsorbate grows in form of three-dimensional islands direct on the substrate. This mode is displayed by many systems of metals growing on insulators, including many metals on alkali halides, graphite and other layer compounds such as mica [5]. It is possible to use the VW growth mode to obtain PbTe quantum dots on BaF<sub>2</sub> [124] or to observe direct growth of CdTe quantum dots on hydrogenated Si(111) substrate using the *hot wall epitaxy* (HWE) technique [125]. Small coherent three-dimensional islands occur in the growth of Si on Ge(111) [126] and e.g. ZnTe on ZnSe [127].

In the simulation, the energetic preference can be achieved by choosing the mixed interaction of adsorbate and substrate particles weaker than the interaction of adsorbate particles with each other. If we set  $U_{as} = 0.7 \times U_a = 0.35 \text{ eV}$ , merely the energetic preference of adsorbate particles to form bonds with particles of the same type is sufficient to observe island growth. In the following, if not explicitly stated, the particle flux is set to  $F = 1.0 \text{ MLs}^{-1}$  and the substrate temperature to  $T = 400 \text{ K}$ .

### 5.3.1 Influence of the misfit on the diffusion process

In order to study the kinetic origin of the island formation, we build a multilayer adsorbate island onto the substrate surface with dimensions that typically occur in the growth simulation. Fig. 5.6 shows the potential energy surface of a test adsorbate particle diffusing across an adsorbate island with misfit  $\varepsilon = 4.0\%$ , obtained within the frozen crystal approximation.

As the chosen mixed interaction is weaker than the adsorbate-adsorbate interaction, both the potential energy of the binding site and the transition state potential energy are decreased on top of the island as well as on their slopes compared to diffusion on the substrate. As expected, the diffusion barrier is not affected by the orientation of the island surface and is the same for diffusion on the slope and on top of the island. The figure also documents the negligible influence of the only weakly pronounced Ehrlich Schwoebel barrier, which therefore can be excluded as the cause of island growth.

The origin of the adsorbate island formation can be understood by looking at the energetic situation of a particle put at the island edge, which is shown in Fig. 5.7. The key role plays the edge site at  $x \approx 38$ , labeled with (B). A particle can either detach again from the island ending up on site (A) or diffuse upward the island slope onto site (C). The transition state potential energy for jumps upward is lower than that for the detaching diffusion process and consequently particles tend to climb up the island slope. An additional lattice mismatch between the

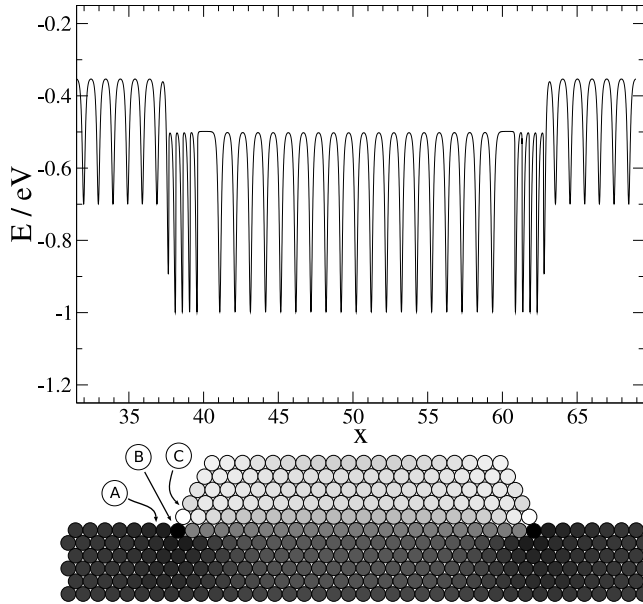


Figure 5.6: Potential energy surface of an adatom moving across a flat symmetric multilayer adsorbate island with 24 base particles and five layers height. The corresponding section of this system with misfit  $\varepsilon = 4.0\%$  shows the detailed position of the potential energy.

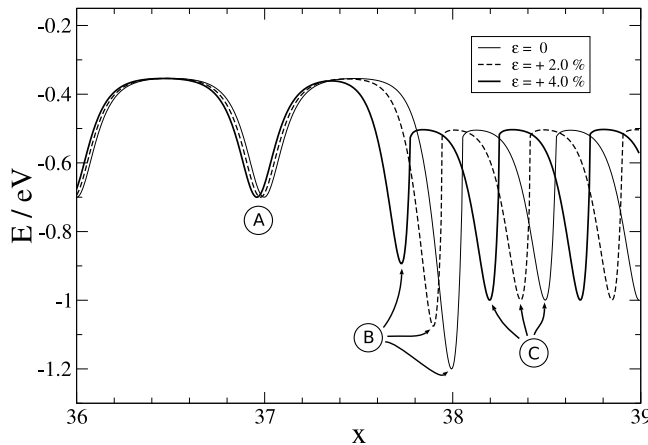


Figure 5.7: Potential energy surface of an adatom moving in the vicinity of the left edge of a flat symmetric multilayer adsorbate island with 24 base particles and five layers height for different values of the misfit  $\varepsilon$ . See system section shown in Fig. 5.6.

adsorbate and substrate amplifies this effect. In the absence of a lattice mismatch the value of the binding energy at the edge site (B) is higher than that of its both neighboring sites (A) and (C), hence the diffusion barrier for particle hops away from this site is higher than for jumps onto this site.

In the presence of a lattice mismatch, the situation is different. In the case of  $\varepsilon = 4.0\%$  the adsorbate particle is better bound at the first site of the island slope (C) than at the edge site (B). Hence, upward jumps are preferred to the according jumps back down and the formation of islands is favored.

Fig. 5.8 displays the difference of the activation energy for the jump to the right neighboring site and the corresponding jump back to the initial site. In all cases, the jump from (A) to the edge site (B) is energetically preferred to the corresponding jump back from (B) to (A), indicated by the negative sign of the energy difference  $\Delta E_a$ . While for the following upward diffusion step from (B)

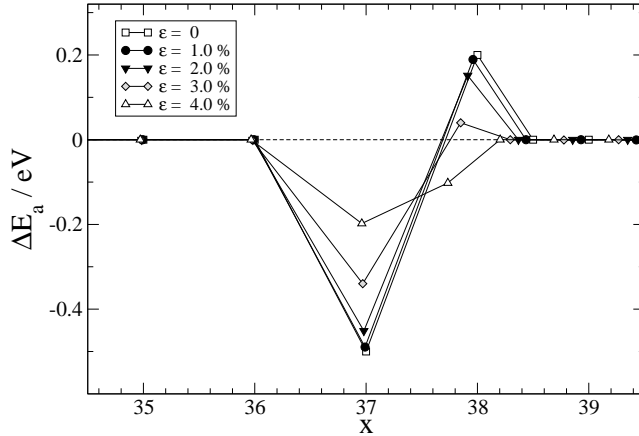


Figure 5.8: Difference of the activation energy for diffusion hops from  $x$  to the next right neighboring site and the corresponding back jump again along the surface shown in Fig. 5.6 for different values of the misfit  $\varepsilon$ .

to (C) the jump back downward from (C) to (B) is preferred in the absence of misfit, this tendency is diluted by increasing misfit and even flipped for the case  $\varepsilon = 4.0\%$  where  $\Delta E_a < 0$ . In conformance with the expectations the difference vanishes for diffusion on the substrate and on the island slope few steps away from the discussed position.

### 5.3.2 Characterization of the island growth

In the last section, the origin of the island growth was studied by energetic considerations. The growth of three dimensional islands is favored by choosing the mixed interaction weaker than the adsorbate-adsorbate interaction. It turned out that an additional lattice mismatch between the adsorbate and substrate amplifies this effect. In order to confirm the expectations gained by preliminary energetic considerations, the following growth simulations were performed on systems with lateral extension of  $L = 600$  atoms.

A typical evolution of VW island growth is shown in Fig 5.9. In the initial state, the diffusing particles nucleate to small islands whose contact area to the substrate is minimized by forming multilayer islands already for small island widths. Beyond this initial nucleation phase, the three-dimensional islands grow due to further deposited adsorbate material and end up in islands of similar shape and size. In the following sections, we discuss the island properties and quantify the evolution of the grown systems as well as the influence of certain parameters.

#### Island properties

The self-assembled islands that emerge during the growth can be characterized by their base width  $b$ , given by the number of atoms in the bottom island layer, and their height  $h$ . The tendency to grow adsorbate islands rather than wetting the substrate is amplified by an additional misfit and can be confirmed by the island properties.

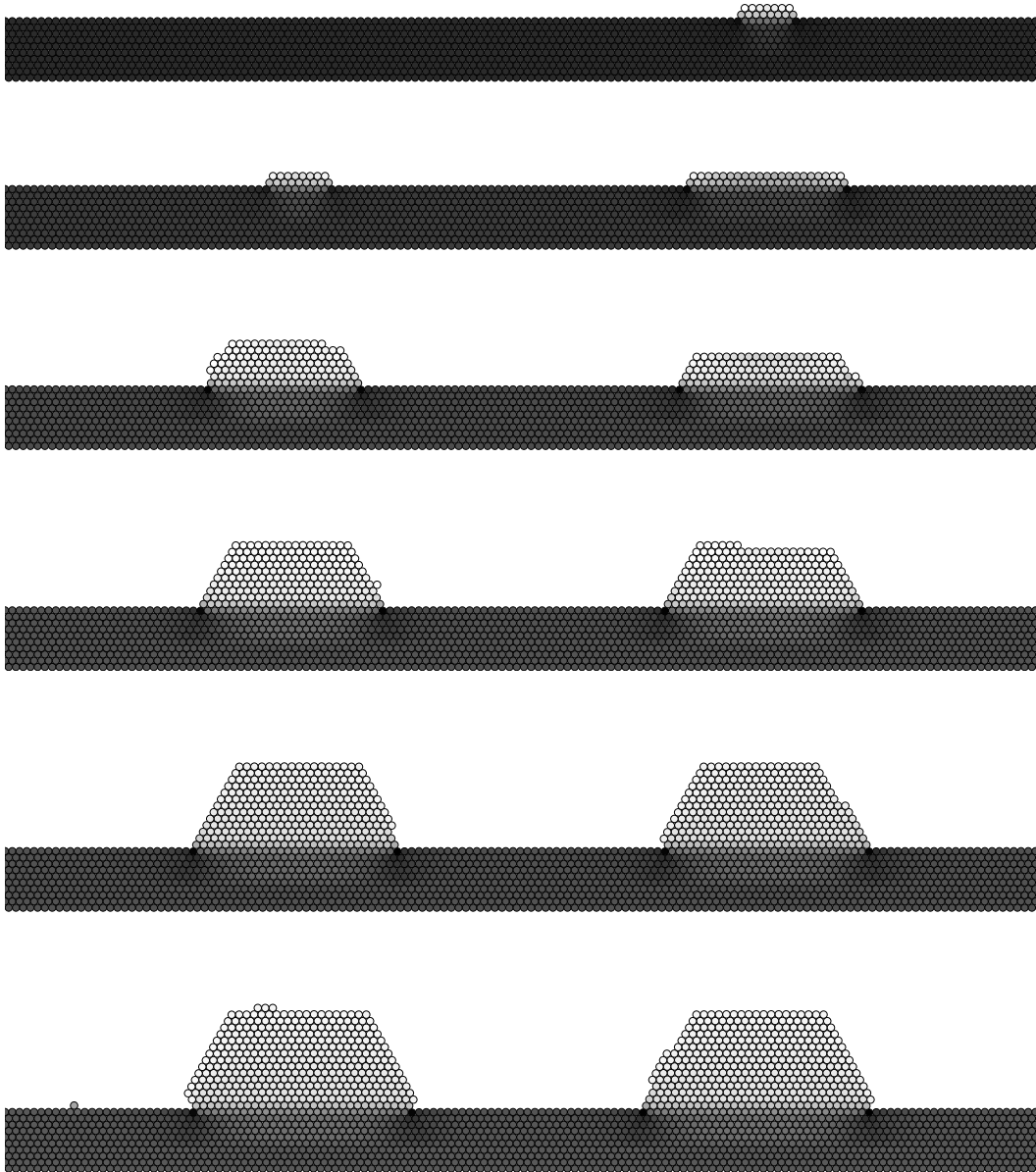


Figure 5.9: Formation of adsorbate islands on a 10 layers thick substrate film of a system simulated with positive misfit  $\varepsilon = 3.0\%$ . This sequence of snapshots shows the evolution of a section of a larger system for top down number of deposited adsorbate layers  $0.1ML$ ,  $0.3ML$ ,  $1.0ML$ ,  $2.0ML$ ,  $3.0ML$ ,  $4.0ML$ . The grey level of the particles indicates the average distance to its nearest neighbors. The lighter a particle is drawn, the larger this distance is.



The distribution of the island base size  $b$  is shown in Fig. 5.10 (top half) for different values of  $\varepsilon$  after the deposition of  $3ML$  adsorbate material. For each value of  $\varepsilon$ , 30 independent simulation runs were carried out. In conclusion, both the favored island base size and the width of the base size distribution decrease with increasing misfit. In consideration of Fig. 5.11 (left side) one can further conclude that for  $\varepsilon = 3.0\%$  the average base size  $\langle b \rangle$  is not affected much by the deposition of further adsorbate material, which consequently leads to a continuous increase of the island height. This is confirmed in Fig. 5.10 (bottom half), showing the distribution of the island height  $h$ , and in Fig. 5.11 (right side), showing the mean height  $\langle h \rangle$  against the amount of deposited adsorbate layers.

Fig 5.12 compares the island size distribution of a system with  $\varepsilon = 3.0\%$  for different numbers of deposited adsorbate layers. The size distribution is symmetric after one monolayer is deposited. After the initial nucleation phase, most of the newly deposited adsorbate material contributes to the island growth and only few new islands occur. However, the lateral growth of the islands is limited to a value  $b \approx 30$  and, since the probability for interlayer jumps increases with the lateral island size, most of the adsorbate particles end up on top of the islands. At  $n_{ads} = 4ML$  almost 35% of all multilayer islands have a base size of  $b = 30$  and not any beyond  $b = 32$  supporting the idea of critical base size  $b_c \approx 30$ .

Since an attaching particle is not bound well at the edge of islands of size  $b \geq b_c$ , a particle can either detach again or jump upward onto the island slope. However, the capacity of islands with  $b \approx b_c$  is limited and instead of growing laterally, which leads to the occupation of energetic uncomfortable edge sites, the islands tend to form overhangs for increasing values of  $n_{ads}$ .

Fig. 5.13 shows the left multilayer island of Fig. 5.9 after the deposition of further adsorbate material. In the case of  $n_{ads} = 6ML$ , overhangs have formed on both sides of the mound. The overhang on the left island side is even more pronounced for  $n_{ads} = 10ML$  which is driven by the system minimizing both the substrate area covered with adsorbate material, due to the preference of adsorbate particles to form bonds with particles of the same type, and the adsorbate surface itself yielding a multilayer island height  $h = 29ML$ .

The occurring overhangs are a good example for the necessity of taking into account all relevant diffusion processes. Without allowing the diffusion on the undersurface of overhangs, the observed island shape would be prevented.

### Behavior of the surface width

A useful tool for the characterization of the VW growth is the surface width (cf. section 5.1). The emergence of multilayer adsorbate islands leads to distinct differences in the surface height modulation and a strictly monotonic increasing surface width can be expected. Besides this qualitative behavior, the surface width is also appropriate to describe the VW growth on a quantitative level.

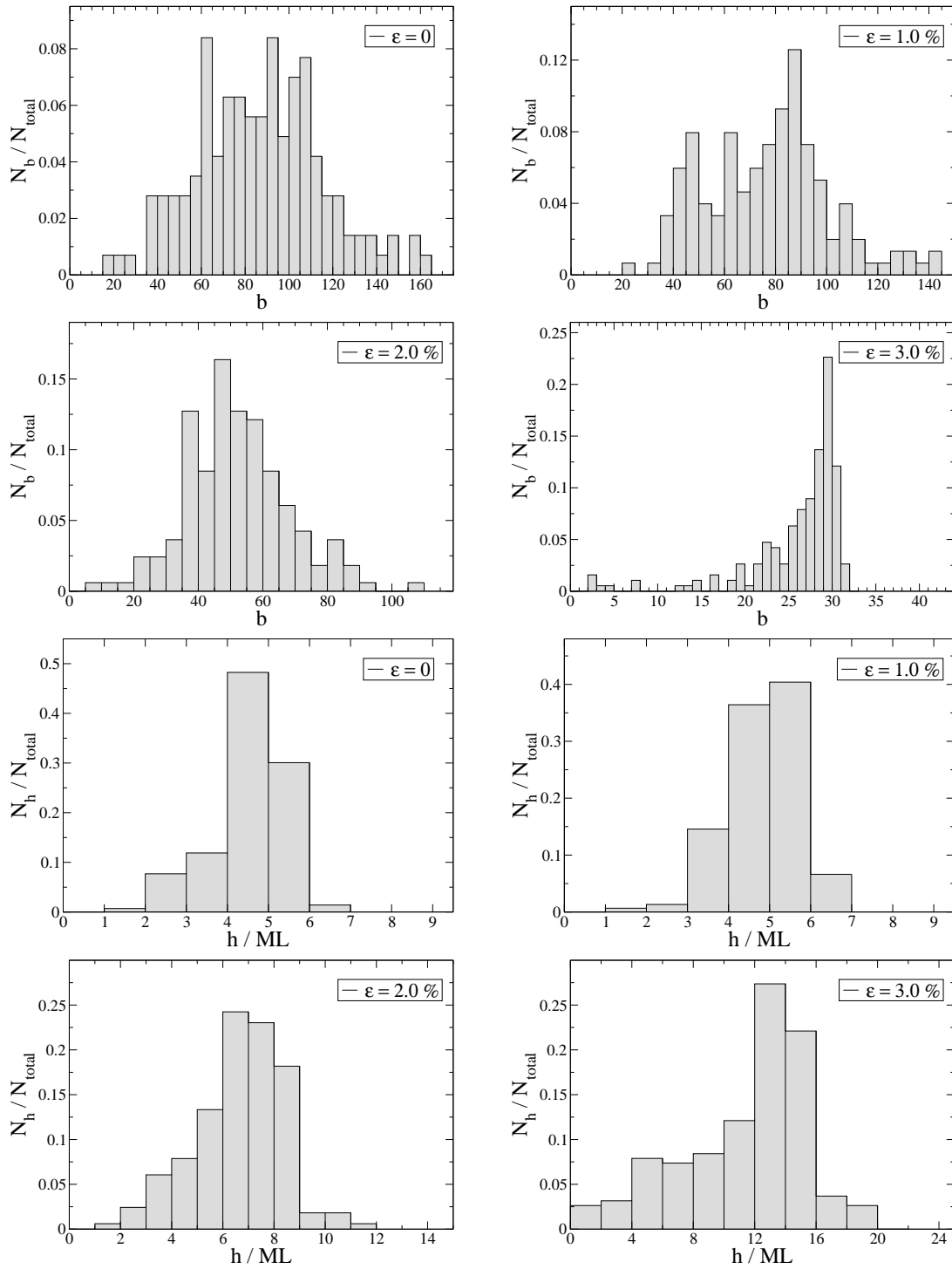


Figure 5.10: Distribution of the island base size  $b$  and height  $h$  after the deposition of  $3ML$  adsorbate material for different values of  $\varepsilon$ . The histograms show the part  $N_b/N_{total}$  of islands with base size  $b$  and  $N_h/N_{total}$  with height  $h$  of all  $N_{total}$  islands. Each bar refers to the abscissa printed at its bottom right side.

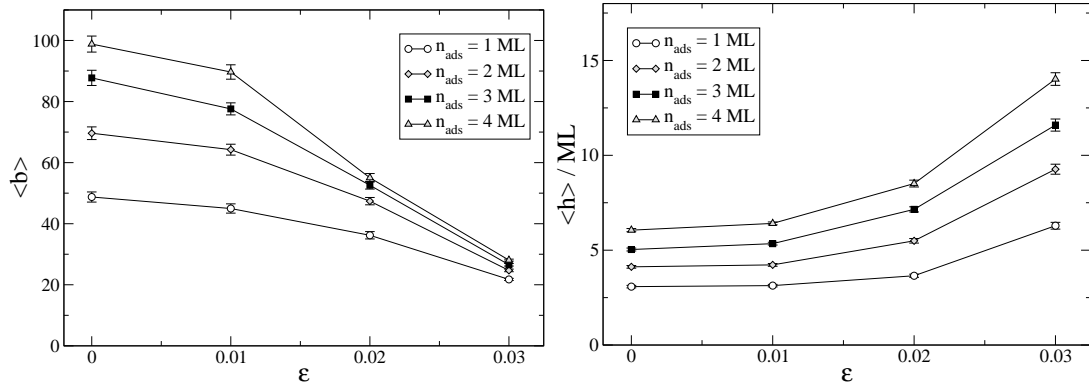


Figure 5.11: Average base size  $\langle b \rangle$  and mean island height  $\langle h \rangle$  of multilayer islands vs. the misfit  $\varepsilon$  for different numbers of deposited adsorbate layers  $n_{ads}$ . The error bars represent the standard errors of the simulation results.

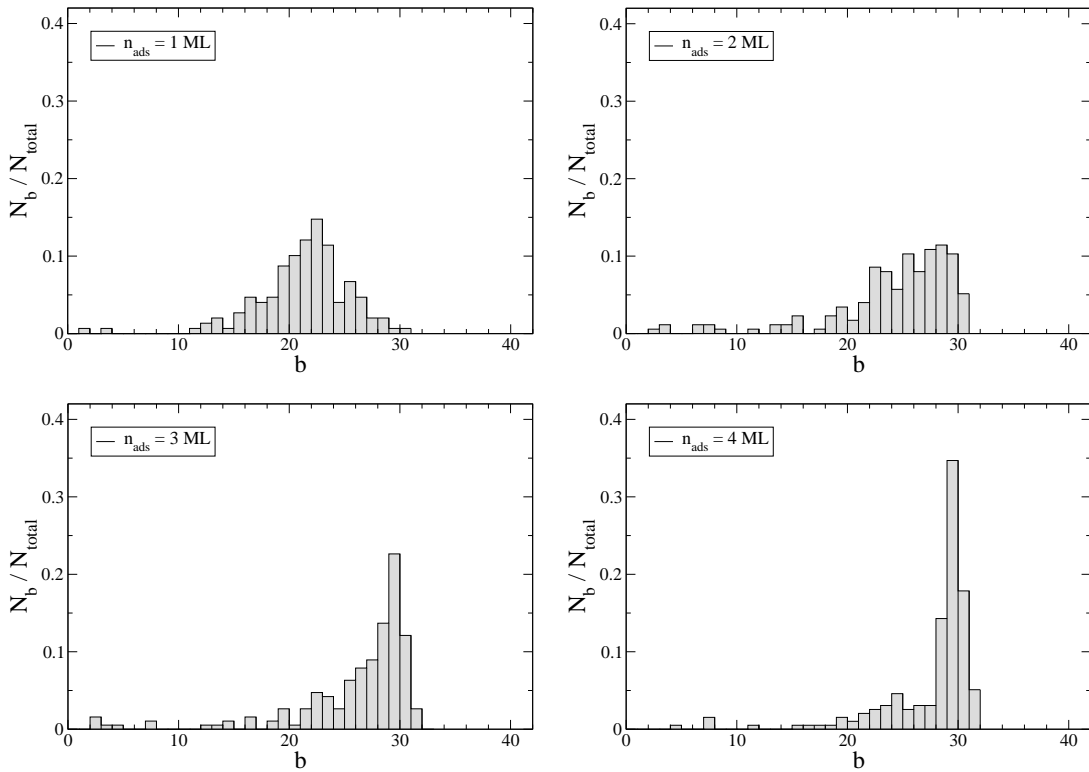


Figure 5.12: Distribution of the adsorbate island base size  $b$  for different numbers of deposited adsorbate layers  $n_{ads}$  with misfit  $\varepsilon = 3.0\%$ . The histograms show the part  $N_b / N_{total}$  of islands with base size  $b$  and  $N_h / N_{total}$  with height  $h$  of all  $N_{total}$  islands. Each bar refers to the abscissa printed at its bottom right side.

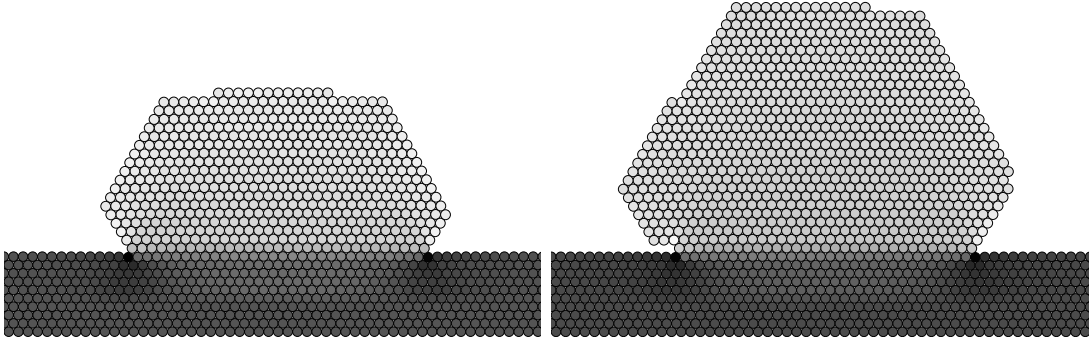


Figure 5.13: Adsorbate island shown on the left in Fig. 5.9 after the deposition of 6  $ML$  (left) and 10  $ML$  (right) of adsorbate material.

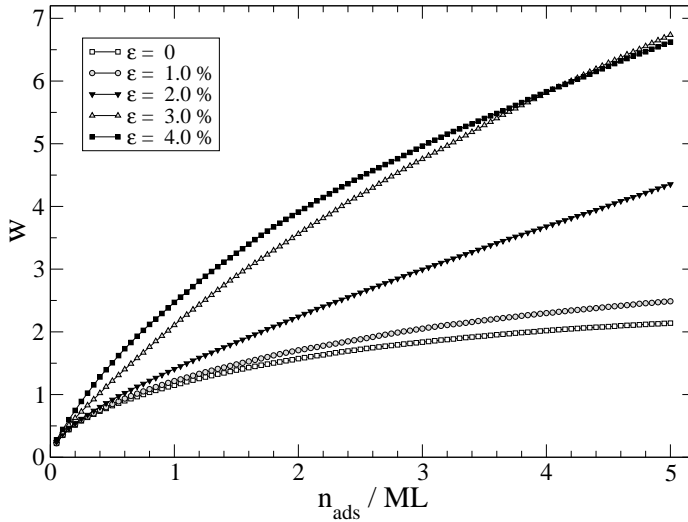


Figure 5.14: Surface width  $w$  vs. the number of deposited adsorbate layers  $n_{ads}$  for different values of the misfit  $\varepsilon$ .

Fig. 5.14 shows the evolution of the surface width  $w$  for different values of  $\varepsilon$ . The surface width increases strictly monotonic with the number of deposited adsorbate particles. Additionally, higher values of  $\varepsilon$  result in a faster increase of  $w$  which is consistent with the island size and height distribution discussed above. However, this performance is disturbed, expressed by an intersection point of the curves for  $\varepsilon = 3.0\%$  and  $\varepsilon = 4.0\%$  at  $n_{ads} \approx 4.1 ML$  caused by the diminishing steepness of the latter curve. For the comparable high misfit  $\varepsilon = 4.0\%$  the island formation mechanism is no longer sufficient to relieve strain during deposition, consequently the strain relief sets in by introducing misfit dislocations and the coherently strained growth is disturbed.

The misfit dislocations, which are formed at the adsorbate-substrate interface, effect a plastic strain relaxation. Thus, only a reduced further elastic strain relaxation by forming multilayer islands is necessary to relieve the residual strain after the introduction of dislocations which is in good agreement with experimental findings [128].

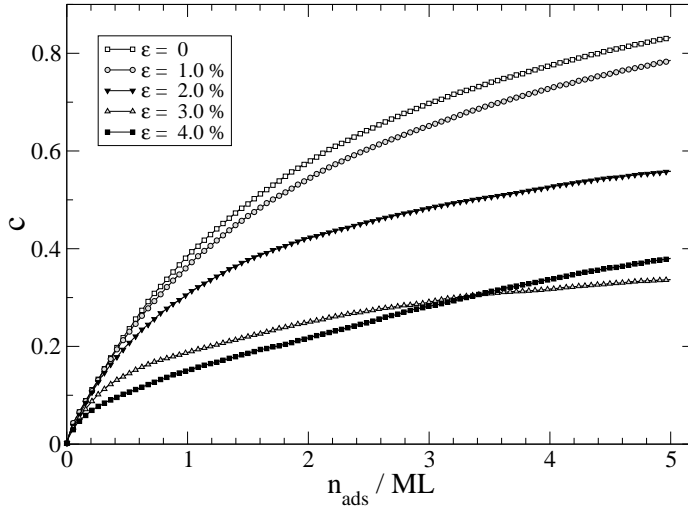


Figure 5.15: substrate area coverage  $c$  vs. the number of deposited adsorbate layers  $n_{ads}$  for different values of the misfit  $\varepsilon$ .

### Behavior of the substrate coverage

A further indicator to characterize the island growth on a quantitative level is the area coverage of the substrate. Fig. 5.15 shows the evolution of the substrate area coverage  $c$  for different values of the misfit  $\varepsilon$ . After the initial island nucleation phase, the adsorbate islands begin to grow in the VW growth mode. Beyond the critical island base size, the main part of the newly deposited adsorbate particles contribute to the island height growth and the lateral island size changes only moderately, indicated by a reduced slope of the curve.

Higher values of  $\varepsilon$  abet upward jumps yielding a smaller slope of the area coverage, which is again consistent with the observed island properties and the behavior of the surface width. For  $\varepsilon = 3.0\%$  the substrate area coverage is only about one third after the deposition of  $5 ML$  adsorbate material.

Again, the case  $\varepsilon = 4.0\%$  breaks this rule, which is caused by the introduction of misfit dislocations and disturbs the coherent growth of strained islands.

### 5.3.3 Transition from layer-by-layer to VW growth

In the last section, we have seen that the lateral island size decreases with increasing lattice mismatch. Besides the misfit, an important condition of the VW growth mode is choosing the adsorbate-substrate interaction potential depth  $U_{as}$  smaller than the potential depth  $U_a$ , which regulates the adsorbate adsorbate interaction strength.

In the discussed case  $U_{as} = 0.7 U_a$ , an additional misfit influences the lateral extension and the height of the islands, but it cannot prevent the island formation itself and therefore the current type of growth mode is not affected. By increasing  $U_{as}$ , but still fulfilling the condition  $U_{as} < U_a$ , one would expect the adsorbate islands to be laterally more extended and it might be possible to find a set of growth parameters so that the islands laterally coalesce before island growth takes



Figure 5.16: Evolution of a system simulated with zero misfit. This sequence of snapshots shows the evolution of a section of a larger system for top down number of deposited adsorbate layers 1.0 *ML*, 2.0 *ML*, 3.0 *ML*, 5.0 *ML*. The darker particles represent the substrate, the lighter particles are adsorbate particles.

place and the VW growth is replaced by the layer-by-layer Frank–van der Merve (FM) growth mode.

The identification of the growth mode can be done with the help of the surface width. In the case of layer-by-layer growth, the surface width initially increases and reaches a maximum at a coverage of about  $c \approx 0.5 \text{ ML}$ , starts decreasing again due to coalescence of the submonolayer islands and ends up in a minimum close to zero after the deposition of a full monolayer. This behavior is repeated for the following layers and therefore the surface width shows an oscillation with period one monolayer.

In order to observe layer-by-layer growth in the simulation, in the following we set  $U_{as} = 0.9 U_a = 0.45 \text{ eV}$  and the temperature  $T = 450 \text{ K}$ . Under this growth conditions and in the absence of a lattice misfit, the system is unable to master the 2d-3d transition and instead of observing island growth the system grows, besides some statistical fluctuations, layer-by-layer which is exemplarily shown in Fig. 5.16.

If the lattice constants of the adsorbate and the substrate differ, the misfit abet upward jumps of the island edge particles and for high enough chosen values the FM-like growth is replaced by the VW-like growth. The system sections shown in Fig. 5.17 are obtained after the deposition of 3 *ML* adsorbate material for different values of  $\varepsilon$ . In the case of  $\varepsilon = 2.0 \%$ , the system cannot perform the VW island growth, since the transition rate from monolayer to bilayer is insufficient

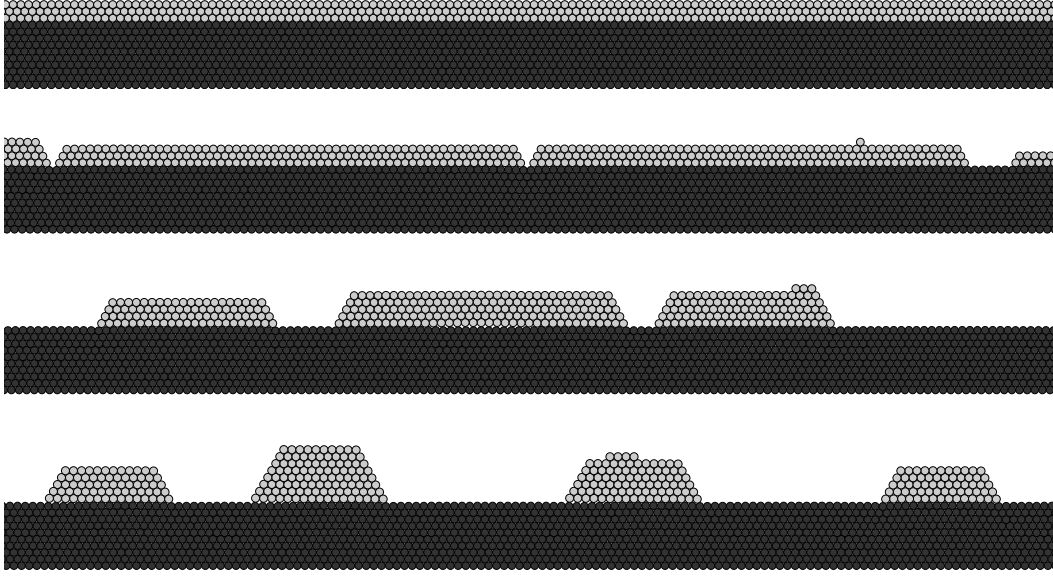


Figure 5.17: Surface topology after the deposition of 3 *ML* adsorbate material for different values of  $\varepsilon$ . This sequence of snapshots shows sections of a larger system for top down misfit  $\varepsilon = 2.0\%$ ,  $3.0\%$ ,  $4.0\%$ ,  $5.0\%$ . The darker particles represent the substrate, the lighter particles are adsorbate particles.

and monolayer islands coalesce instead. However, for increasing misfit upward jumps become more and more probable. While for  $\varepsilon = 3.0\%$  the islands are quite flat and close to each other, compact multilayer adsorbate islands are formed for  $\varepsilon = 5.0\%$ . The observed influence of the misfit supports the assumption of a transition from layer-by-layer to island growth under the present growth conditions.

For a more quantitative investigation, Fig. 5.18 compares the evolution of the surface width for different values of  $\varepsilon$ . While for  $\varepsilon \leq 2.0\%$  the system still grows layer-by-layer with the expected oscillating progression of the surface width with period 1 *ML* and minima at complete deposited layers, for  $\varepsilon \geq 4.0\%$  clear island growth can be attested by the strictly monotonic increasing progression of  $w$ . The case  $\varepsilon = 3.0\%$  can be seen as intermediate. The change from an oscillating to a monotonic increasing progression of the surface width for increasing misfit documents the transition from layer-by-layer to VW growth and is also reported e.g. in [129] based on a solid-on-solid model with cubic lattice where elastic effects are incorporated using a ball and spring type model.

The observed transition can also be clearly seen in Fig. 5.19, showing the surface width after the deposition of 5 *ML* adsorbate material for different values of  $\varepsilon$ . Up to  $\varepsilon = 2.0\%$  the surface width shows a constant low progression, but increases fast when increasing  $\varepsilon$  from  $3.0\%$  to  $4.0\%$ .

The behavior of the substrate area coverage  $c$ , which is displayed as a function

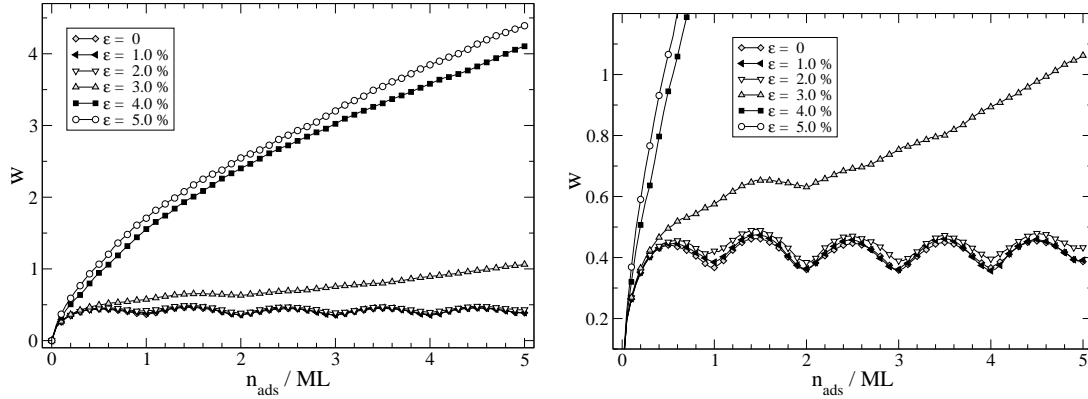


Figure 5.18: Surface width  $w$  vs. the number of deposited adsorbate layers  $n_{ads}$  for different values of the misfit  $\epsilon$ . The right figure shows the section of the oscillating curve progression for moderate misfit.

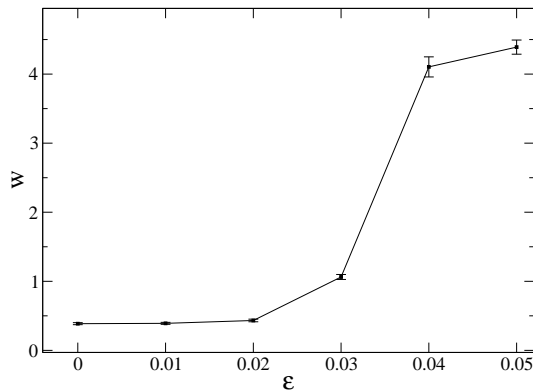


Figure 5.19: Surface width  $w$  for different values of  $\epsilon$  after the deposition of 5  $ML$  adsorbate material. The error bars represent the standard errors of the simulation results.

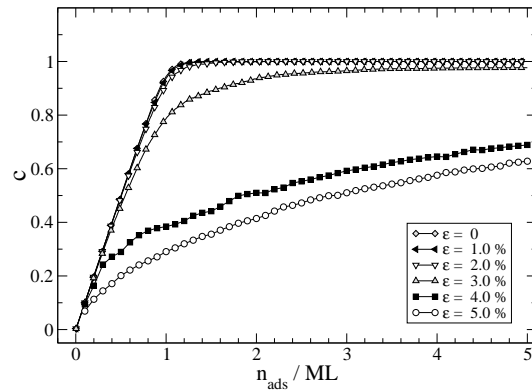


Figure 5.20: Substrate area coverage  $c$  vs. the number of deposited adsorbate layers  $n_{ads}$  for different values of the misfit  $\epsilon$ .





Figure 5.21: Surface topology after the deposition of 3 *ML* adsorbate material for different substrate temperatures with misfit  $\varepsilon = 2.0\%$ . This sequence of snapshots shows sections of a larger system for top down temperature  $T = 450\text{ K}, 550\text{ K}, 600\text{ K}$ . The darker particles represent the substrate, the lighter particles are adsorbate particles.

of the number of deposited adsorbate layers  $n_{ads}$  for different values of  $\varepsilon$  in Fig. 5.20, confirms the necessity of a sufficiently high misfit to perform the transition from FM to VW growth as well. For each value of  $\varepsilon$ , a different number of independent simulation runs were carried out. This number depends on the simulation time needed for a single run, since simulating layer-by-layer growth is much faster than island growth. For  $\varepsilon \leq 2\%$  the substrate is almost completely covered by adsorbate particles after the deposition of the first adsorbate layer which documents a layer-wise growth behavior. The complete coverage of the substrate with adsorbate material is slightly delayed, which is caused by fluctuations and can be explained by the kinetic origin of the observed growth.

In contrast to the real FM growth mode, introduced by Bauer and based on thermodynamic considerations, MBE takes places far away from equilibrium. Besides the misfit also the substrate temperature has influence on the observed transition. The probability of monolayer islands to perform the monolayer-bilayer transition, by upward jumps of their edge particles, increases strongly with the temperature, since the diffusion rate depends exponentially on the temperature, see Eq. (2.2). The influence of the temperature on the growth behavior can be seen in Fig. 5.21 showing systems grown at different substrate temperatures and misfit  $\varepsilon = 2.0\%$ . While layer-by-layer growth takes place at  $T = 450\text{ K}$ , we observe the formation of islands for higher temperatures, whereas the islands formed at  $T = 600\text{ K}$  are more pronounced and show smaller lateral extensions and increased heights compared to the case  $T = 550\text{ K}$ . This effect is originated by the increased rate for upward jumps.

Again, a more qualitative comparison shows the behavior of the surface width in Fig. 5.22 (left). While the oscillating progression of the curve obtained at  $T = 450\text{ K}$  indicates layer-by-layer growth the monotonic increasing progression at higher temperatures results from the VW growth. Again, the behavior of

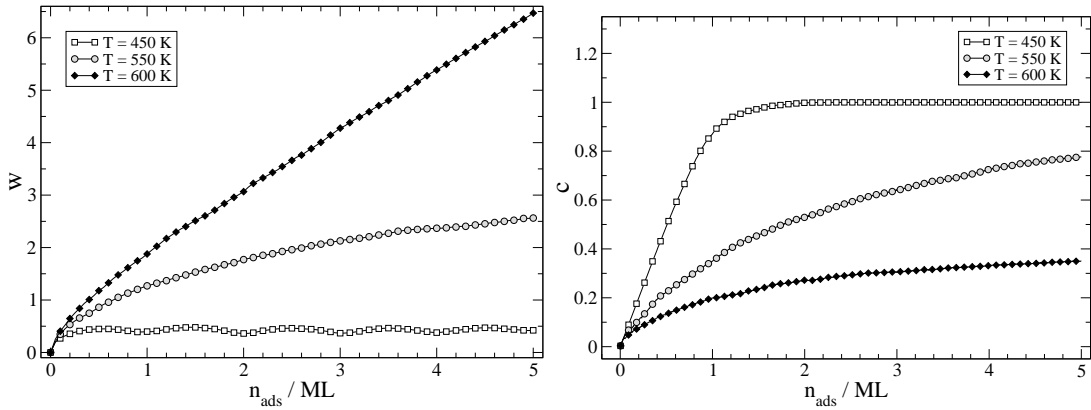


Figure 5.22: Surface width  $w$  (left) and substrate area coverage  $c$  (right) vs. the number of deposited adsorbate layers  $n_{ads}$  for three different substrate temperatures with misfit  $\varepsilon = 2.0\%$ .

the substrate area coverage, shown in Fig. 5.22 (right), is in accordance with the observed transition from layer-by-layer to island growth when increasing the temperature. For each temperature, up to 30 independent simulation runs were carried out. The chosen temperature values do not aim at identifying the type of transition or even determine a possible critical temperature, since this would exceed the available computing time. The shown temperature dependency reveals that the growth will not follow the true layer-by-layer mechanism, which means complete coverage of the substrate by one monolayer before the next one nucleates, since the thermodynamics favor island growth. This pseudo FM mode is induced by the limited mobility of the adatoms, thus flat adsorbate films grown at low temperatures are metastable and upon heating they will break up and agglomerate into islands.

The observed transition from layer-wise to VW growth by increasing the substrate temperature is in agreement with previous studies in theory [130, 131] and experiment [132]. In the latter Si is grown layer-wise on Ge at low temperatures, while VW growth is observed at higher temperatures.

## 5.4 Stranski–Krastanov-like growth

Besides the two observed layer-by-layer and VW like growth mode, thin crystalline films can also grow in the Stranski–Krastanov (SK) growth mode, which can be seen as the intermediate mode (cf. section 2.3). In the FM growth mode, the film atoms are more strongly bound to the substrate than to each other. Consequently, each layer is fully completed before the next layer starts to grow and strictly two-dimensional growth takes place. This energetic condition is also given in the SK mode, however the system is also affected by the lattice mismatch

which leads to elastic strain. In the initial phase, the system grows layer-by-layer, but with decreasing influence of the substrate and increasing strain, the formation of islands on the formerly grown wetting layer becomes favorable. The resulting increase of surface energy is overcompensated by a decrease of strain energy due to the elastic strain relaxation towards the bulk lattice constant in the upper parts of the grown islands.

The SK growth mode is topic of many studies in theory and experiment. Special progress in the understanding of strain-induced nanostructure self-organization has been obtained in the SK growth of semiconductors that has been stimulated by numerous experimental studies to grow quantum-dot arrays for optoelectronic applications. The growth of pure Ge or  $\text{Si}_{1-x}\text{Ge}_x$  alloys on Si(001) represents one of the most extensively studied systems of semiconductor heteroepitaxy [133–135]. Further prominent examples of SK systems are III-V [136, 137] and II-VI [138, 139] semiconductor compounds.

The realization of SK growth in the simulation can be achieved by choosing the mixed interaction of adsorbate and substrate particles stronger than the interaction of adsorbate particles with each other. If we set  $U_{as} = 4.0 U_a = 2.0 eV$ , an energetic preference of adsorbate particles to form bonds with substrate particles is accomplished. In the following, if not explicitly stated, the particle flux is set to  $F = 1.0 MLs^{-1}$  and the substrate temperature to  $T = 600 K$ .

### 5.4.1 Stable wetting layer

By choosing  $U_{as} > U_a$ , the diffusion of adsorbate particles is found to be slower on the substrate than on subsequent adsorbate layers. The energetic situation is depicted in Fig. 5.23 showing the potential energy surface of a test adsorbate particle diffusing across an adsorbate monolayer island with misfit  $\varepsilon = 4.0 \%$ , obtained within the frozen crystal approximation.

As the chosen mixed interaction is stronger than the adsorbate-adsorbate interaction, both the potential energy of the binding site and the transition state potential energy are increased on top of the island compared to diffusion on the substrate. The figure also documents the negligible influence of the only weakly pronounced Ehrlich Schwoebel barrier. One can further conclude that upward jumps are quite improbable, since the activation energy for particle interlayer hops from the island edge site, labeled with (B), onto the island site (C) is quite large and the particle preferentially detaches to the site labeled with (A). The jumps down from (C) to (B) however can be easily performed and by taking the slow diffusion on the substrate into account, a stable wetting monolayer can be expected. The misfit between the adsorbate and the substrate cannot influence this behavior decisively and only effects a weaker bond of the island edge particles.

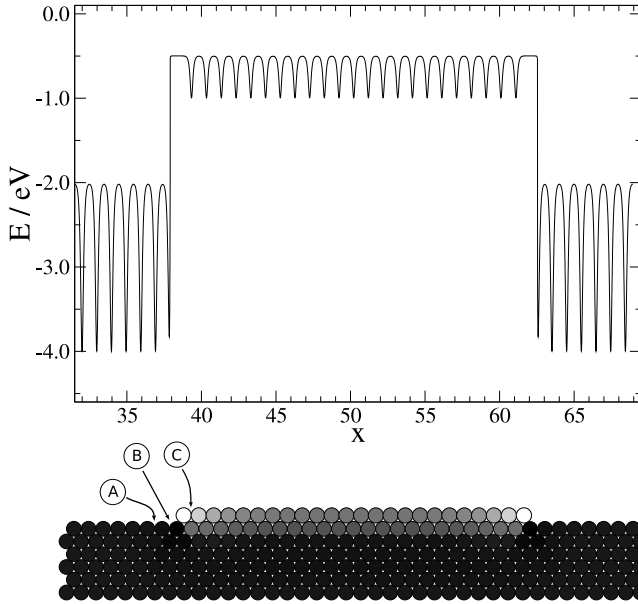


Figure 5.23: Potential energy surface of an adatom moving across a flat symmetric monolayer adsorbate island consisting of 24 particles. The corresponding section of this system with misfit  $\varepsilon = 4.0\%$  shows the detailed position of the potential energy.

### 5.4.2 Influence of the misfit on the island growth

After the stable wetting monolayer has formed, the adatoms begin to nucleate to new islands on top of it. Due to the steep form of the chosen potential, the influence of the underlying substrate film decreases fast with the adsorbate film thickness and the system is affected by the strain.

Fig. 5.24 shows the potential energy surface of a test adsorbate particle diffusing on the wetting layer across an adsorbate monolayer island, obtained within the frozen crystal approximation. Just like the previous situation, the island consists of 24 adsorbate particles and has the same lateral position.

The differences between diffusion on top of the island and aside the island is less pronounced than in the situation without a wetting layer which is shown in Fig. 5.23. By comparing the two curves, the role of the lattice mismatch becomes apparent. Firstly, the edge particle of the island is worse bound in the case of non-vanishing misfit. Secondly, the transition state potential energy for detaching is decreased. Thus, diffusion away from this site is clearly preferred, compared to the case without misfit. With increasing lateral extension, the monolayer islands on top of the wetting layer become more and more unstable. Besides detaching again, the edge particles also perform jumps on top of the island. This is repeatedly done until two diffusing particles nucleate on top of the island. This newly formed island is less unstable, since it is laterally less extended.

The diffusion on top of such an island is affected by both the misfit and the island height. The diffusion barrier  $E_a$  for a particle on top of a multilayer island placed on the first wetting layer as a function of the lateral particle position  $x$  is shown for different values of  $\varepsilon$  in Fig. 5.25 and for different values of the island height in Fig. 5.26.

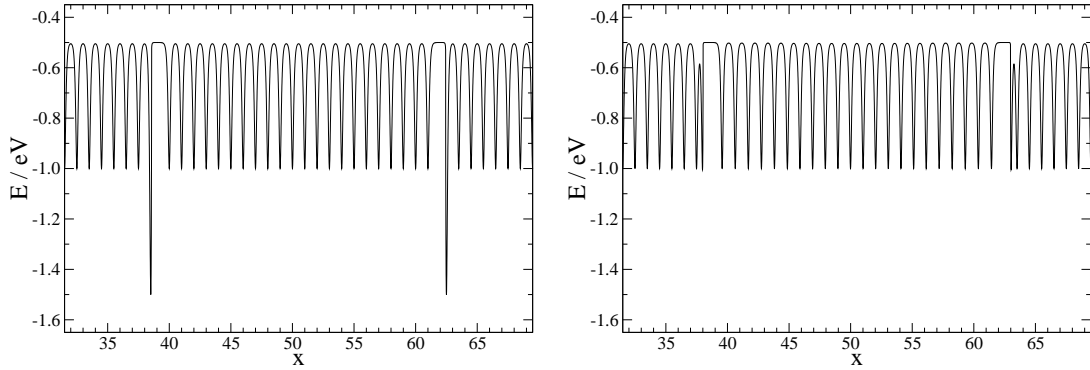


Figure 5.24: Potential energy surface of an adatom moving across a monolayer adsorbate island, consisting of 24 particles, on top of the wetting monolayer without misfit (left) and  $\varepsilon = 6.0\%$  (right).

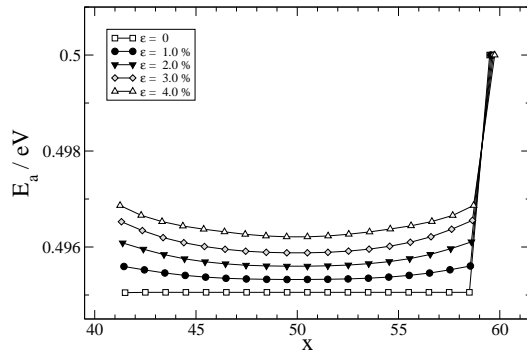


Figure 5.25: Activation energy for particle hops to the right on top of a multilayer island with 24 base particles and four layers height placed on the first wetting layer as a function of the lateral position  $x$  for different values of  $\varepsilon$ . The rightmost barriers correspond to downward jumps at the island edge.

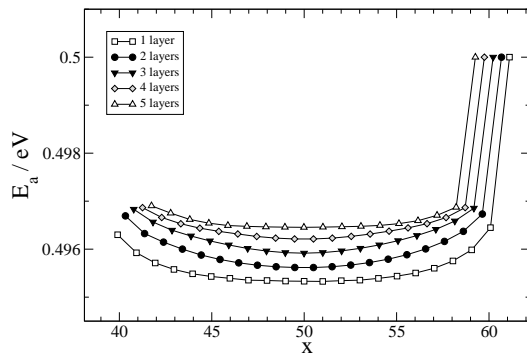


Figure 5.26: Activation energy for particle hops to the right on top of a multilayer island placed on the first wetting layer as a function of the lateral position  $x$  for different values of the island height. The rightmost barriers correspond to downward jumps at the island edge. The misfit is  $\varepsilon = 4.0\%$ .

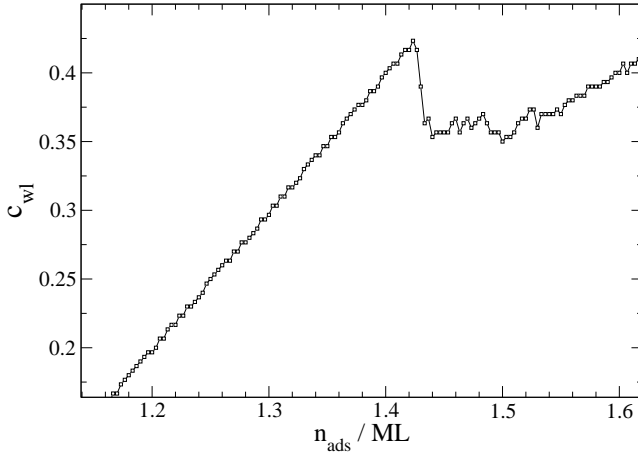


Figure 5.27: Wetting layer area coverage  $c_{wl}$  vs. the total number of deposited adsorbate layers  $n_{ads}$ .

In consideration of the island's symmetry, one can conclude that the misfit leads to a diffusion bias towards the island center which is more pronounced for higher misfits and for higher island heights. The intensity of this modulation is relatively small and the main influence on the island formation results from the weaker bonds of the island edge particles. Epitaxial strain relaxation at the island edges of systems grown in the SK mode was reported in several theoretical studies, e.g. [140, 141].

The first step in the formation of multilayer islands is the rearrangement of monolayer islands to bilayer islands. A possible process is that the material for the bilayer island comes almost completely from the original monolayer island, found by Monte Carlo simulations in [141, 142], but also confirmed in experimental studies, e.g. Moison et al. [143] reported that the coverage suddenly decreases when three-dimensional InAs islands begin to form on GaAs. One monolayer thick InAs islands were suggested to act as precursors for the formation of thicker structures on GaAs.

The phenomenon monolayer islands serving as necessary precursors for multilayer islands can be observed in our simulations as well. Just like Moison, a sudden decrease of the wetting layer area coverage  $c_{wl}$  occurs, displayed in Fig. 5.27 for a system simulated with  $\varepsilon = 4.0\%$ . Initially, the coverage increases monotonically with slope  $m = 1$ , since all particles deposited on the wetting layer are part of monolayer islands. Note that the number of deposited adsorbate layers  $n_{ads}$  also includes the wetting layer. At about  $n_{ads} \approx 1.42$ , the wetting layer coverage decreases from  $c_{wl} \approx 0.42$  to  $c_{wl} \approx 0.35$  but starts increasing again at about  $n_{ads} \approx 1.5$  with slope  $m < 1$ . Fig. 5.28 shows one of the corresponding islands formed in the considered example simulation. The initial flat monolayer island, consisting of 25 particles, is unstable and upward jumps of the edge particles become favorable. After the formation of a stable nucleus on top of the one monolayer thick island, it ends up in a symmetric bilayer island. This island only consists of the former monolayer island particles which confirms the idea of

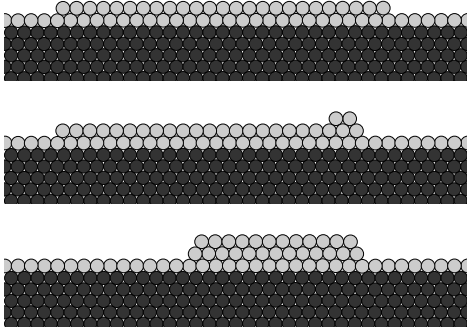


Figure 5.28: Bilayer island formation in the simulated system of Fig. 5.27. The sequence of snapshots shows top down the temporal evolution of a section of a larger system. The darker particles represent the substrate, the lighter particles are adsorbate particles.

monolayer islands serving as precursors for bilayer islands.

The typical evolution of the SK island growth is exemplarily shown in Fig 5.29. After the deposition of the first layer, a stable wetting layer has formed. In the further growth progression, several monolayer islands nucleate on top of it. By comparing the cases  $n_{ads} = 1.7 ML$  and  $n_{ads} = 2.4 ML$  one can see that, despite the additional amount of adsorbate particles in the system, the occurring multilayer island on the right is laterally less extended than the monolayer island at the same position in the temporal earlier case. This is concordant with the observed formation mechanism displayed in Fig. 5.28 and the monolayer islands act as precursors for the multilayer islands.

The monolayer island in the middle, see case  $n_{ads} = 1.7 ML$ , is not able to perform the transformation from mono- to bilayer, instead the detaching edge particles are incorporated in the neighboring multilayer islands. In the following, the islands grow due to further deposited adsorbate material and end up in islands of similar shape and size.

### 5.4.3 Transition from layer-by-layer to SK growth

In the last section, we have seen that the lattice mismatch between substrate and adsorbate is an indispensable condition to observe SK growth. In several investigations a critical misfit for the transformation from layer-by-layer to SK growth is reported [140, 141, 144, 145]. To investigate the misfit dependency of the island growth, simulations were performed for different values of the misfit.

The grown surfaces displayed in Fig. 5.30 show representatively the influence of the misfit after the deposition of five layers of adsorbate material. By looking at the case  $\varepsilon = 1.0\%$ , the system cannot perform the SK island growth for low values of  $\varepsilon$ , since the resulting increase of surface energy by formation of mounds cannot be compensated by the decrease of the strain energy due to the elastic strain relaxation. Under the given growth conditions, the system cannot perform SK growth in the case  $\varepsilon = 1.5\%$ . While for  $\varepsilon = 3.0\%$  and  $\varepsilon = 4.0\%$  the previous discussed SK growth can be attested, for the case  $\varepsilon = 2.0\%$  no clear declaration can be made, but one cannot exclude a possible critical misfit in the range  $1.0\% < \varepsilon < 2.0\%$ . However, the assumption of a transition from

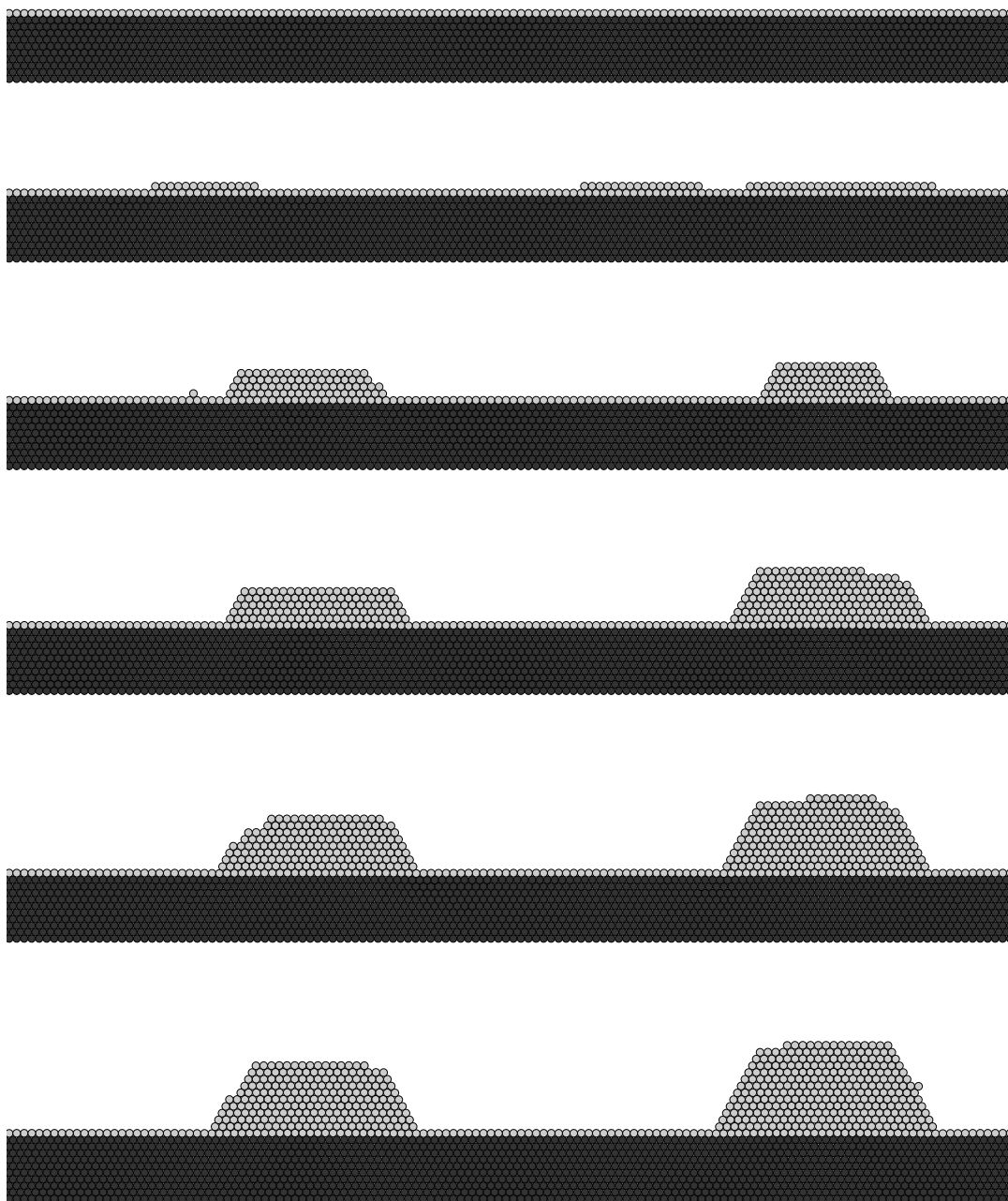


Figure 5.29: Formation of adsorbate islands on the wetting layer with misfit  $\varepsilon = 3.0\%$ . This sequence of snapshots shows the evolution of a section of a larger system for top down number of deposited adsorbate layers  $1.0 ML$ ,  $1.7 ML$ ,  $2.4 ML$ ,  $3.0 ML$ ,  $4.0 ML$ ,  $5.0 ML$ . The darker particles represent the 10 layer thick substrate film, the lighter particles are adsorbate particles.



layer-by-layer to SK island growth is justified.

For a more quantitative investigation, Fig. 5.31 compares the evolution of the surface width for different values of  $\varepsilon$ . Independent of the misfit, the first deposited layer forms a flat stable wetting layer, indicated by the maximum at half and the minimum at full first layer coverage.

In the following, for moderate values of  $\varepsilon$ , the system grows layer-by-layer with the expected oscillating surface width of period  $1 ML$  and minima at complete deposited layers. Due to statistical fluctuations, slight deviations from the perfect oscillation can be observed, as epitaxial growth is per definition a non-equilibrium process determined by kinetic phenomena and growth morphologies will deviate more or less from the thermodynamic picture. For  $\varepsilon \geq 2.0\%$  SK island growth can be supposed. The change from an oscillating to a monotonic increasing progression of the surface width on the wetting layer for increasing misfit documents the transition from layer-wise to SK growth which is also supported by Fig. 5.33 showing the surface width after the deposition of  $5 ML$  adsorbate material for different values of  $\varepsilon$ . Up to  $\varepsilon = 1.5\%$ , the surface width shows a constant and low progression, but increases fast when increasing  $\varepsilon$  from  $3.0\%$  to  $4.0\%$ .

The kinetic processes determining the morphology of the surface depend on the temperature and the particle flux. The formation of islands is facilitated at high temperatures and hindered at low temperatures. The right image of Fig. 5.32 displays the temporal evolution of the surface width of systems with  $\varepsilon = 3.0\%$  at different temperatures. While for the case  $T = 600 K$  SK growth can be attested, for  $T = 400 K$ , and below, the limited mobility of the adatoms even leads to a delayed complete wetting of the substrate, identifiable by the increased value of  $w$  at  $n_{ads} = 1 ML$  and one can observe layer-wise growth instead. The observed statistical fluctuations result from the limited number of 10 independent runs. The system grows layer-wise with rough character due to the formation of broad adjacent islands of low height. The grown films are metastable and upon heating they will break up and agglomerate into multilayer islands.

On the left side of Fig. 5.32, the temperature dependency of the surface width is shown for  $\varepsilon = 2.0\%$ . While the oscillating progression of the curves obtained at  $T \leq 500 K$  indicates layer-by-layer growth, the monotonic increasing progression at higher temperatures is evidence of SK growth. Similar to the temperature behavior of the VW growth, see section 5.3.3, the temperature dependency for  $\varepsilon = 2.0\%$  reveals that the growth will not follow the true layer-by-layer mechanism, as the thermodynamics favor island growth. This pseudo FM mode is originated by the limited mobility of the adatoms and the flat adsorbate films grown at low temperatures are metastable. Thus, islands will form when the system is heated up.

Due to the fast increase of the roughness  $w$  for high substrate temperatures, the existence of a critical temperature can be supposed which is reported e.g. in [130,132] and also supported by Fig. 5.34 showing the surface width after the deposition of  $5 ML$  adsorbate material as a function of the substrate temperature

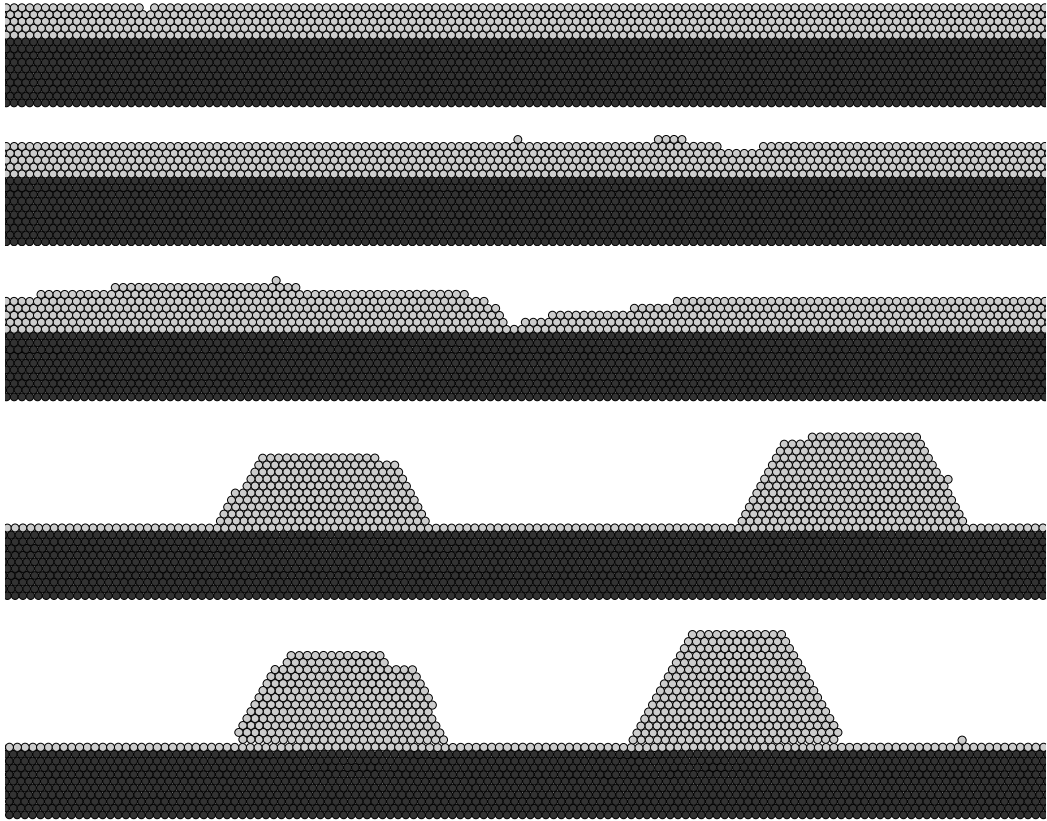


Figure 5.30: Surface topology after the deposition of 5  $ML$  adsorbate material for different values of  $\varepsilon$ . This sequence of snapshots shows sections of a larger system for top down misfit  $\varepsilon = 1.0\%$ ,  $1.5\%$ ,  $2.0\%$ ,  $3.0\%$ ,  $4.0\%$ . The darker particles represent the substrate, the lighter particles are adsorbate particles.

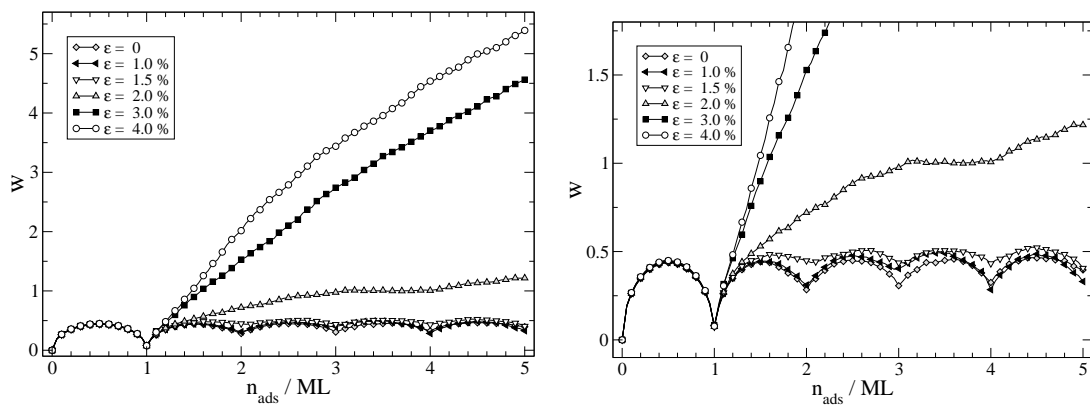


Figure 5.31: Surface width  $w$  vs. the number of deposited adsorbate layers  $n_{ads}$  for different values of  $\varepsilon$ . The right figure shows the section of the oscillating curve progression for moderate values of the misfit.

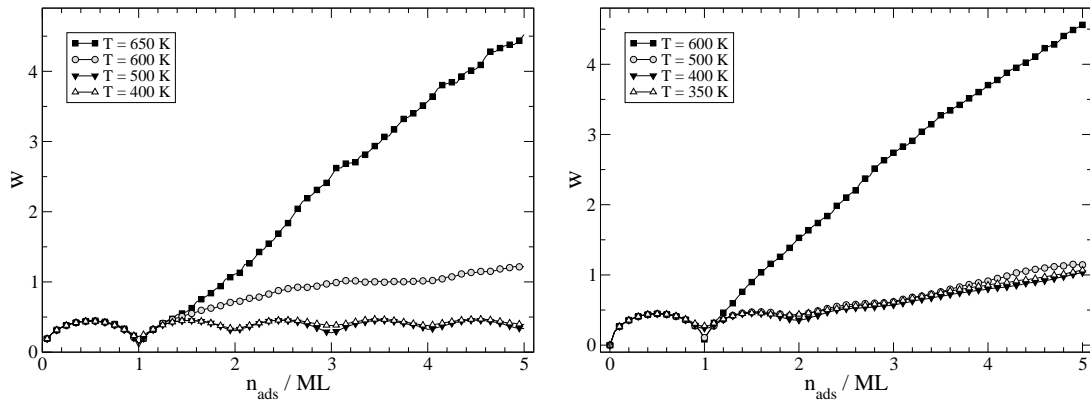


Figure 5.32: Surface width  $w$  vs. the number of deposited adsorbate layers  $n_{ads}$  for different values of the substrate temperature  $T$ . The misfit is  $\varepsilon = 2.0\%$  (left) and  $\varepsilon = 3.0\%$  (right).

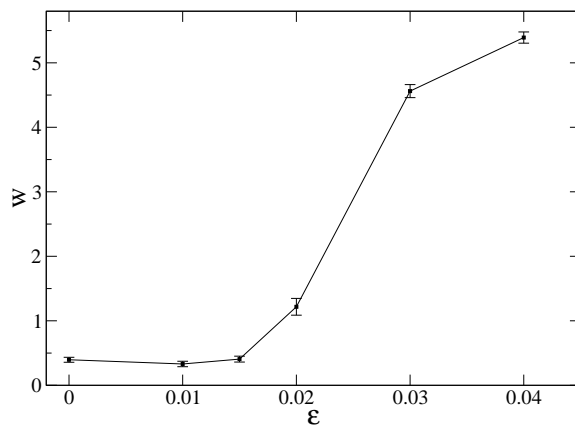


Figure 5.33: Surface width vs.  $\varepsilon$  after the deposition of  $5 ML$  adsorbate material at  $T = 600 K$ . The error bars represent the standard errors of the simulation results.

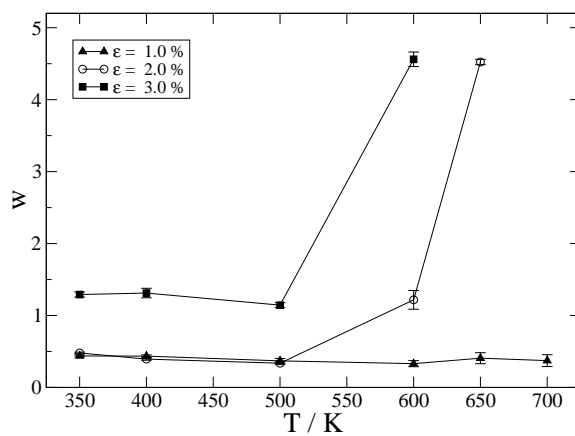


Figure 5.34: Surface width vs. substrate temperature after the deposition of  $5 ML$  adsorbate material for different values of  $\varepsilon$ . The error bars represent the standard errors of the simulation results.

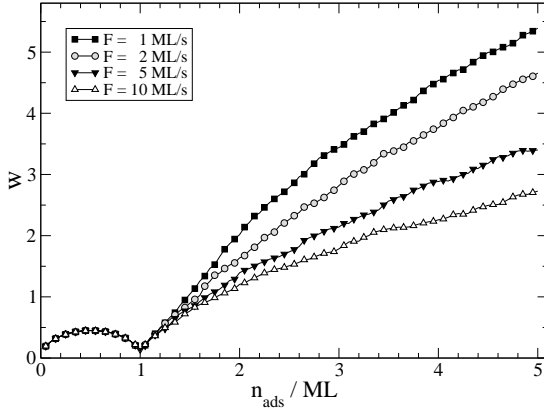


Figure 5.35: Surface width  $w$  vs. the number of deposited adsorbate layers  $n_{ads}$  for different values of the particle flux  $F$ .

$T$  for several values of  $\varepsilon$ . The case  $\varepsilon = 1.0\%$  breaks the rule and no SK growth can be observed even for very high temperatures. The resulting increase of surface energy cannot be compensated by a decrease of strain energy due to the elastic strain relaxation. Thus, the system is not able to perform the transition from layer-by-layer to SK growth in the case  $\varepsilon = 1.0\%$  which is obviously below the critical misfit. Instead, layer-by-layer growth can be observed independent of the substrate temperature, which is a necessary condition for the Frank–van der Merve growth mode [130].

However, an exact determination of the critical misfit as well as a possible critical temperature cannot be realized due to the high computer time costs (a single run simulating SK growth under typical growth conditions can last up to several weeks on the present desktop PCs).

A further instrument to restrain the island growth is increasing the particle flux which reduces the available time for particles to do jumps onto the islands. Fig. 5.35 shows the temporal evolution of the surface width of systems with  $\varepsilon = 4.0\%$  for different values of the particle flux  $F$ . Similar to the case of low temperatures, a high particle flux hinders the system to grow in the SK mode with well pronounced islands resulting a less steep progression of  $w$ .

## 5.5 Conclusions

In summary, we have demonstrated that it is possible to adjust within our simulation model each of the three epitaxial growth modes: Volmer–Weber, Frank–van der Merve or layer-by-layer, and Stranski–Krastanov growth mode.

As epitaxial growth is a process far from thermodynamic equilibrium and determined by kinetic phenomena, the occurring growth morphologies deviate from the thermodynamic picture and cannot be applied to MBE in the strict sense. However, the classification of these metastable growth modes is useful to characterize the growing surface and to distinguish between different growth behaviors.

The emerging growth mode principally depends on two parameters. The most important role plays the relation of the interaction of adsorbate particles with each other, represented by the potential depth  $U_a$ , and the interaction of adsorbate particles with substrate particles, given by  $U_{as}$ . The second important parameter is the lattice mismatch between adsorbate and substrate, represented by the misfit  $\varepsilon$ .

By choosing  $U_a > U_{as}$ , an energetic preference of adsorbate particles to form bonds with particles of the same type is present. In the thermodynamic limit, the energy balance requires to minimize the area covered by the adsorbate material. Consequently, the adsorbate grows in form of three-dimensional islands direct on the substrate showing a regular shape and size distribution.

Since epitaxial growth is governed by surface kinetics, the transition from VW to layer-wise growth can be controlled by both the lattice misfit and the substrate temperature indicated by critical values of  $\varepsilon$  and  $T$  at given growth conditions. However, only a pseudo FM growth mode can be adjusted, since flat adsorbate films grown at low temperatures are metastable and will break up upon heating and agglomerate into islands. In the thermodynamic limit, merely the condition  $U_a > U_{as}$  leads to the formation of adsorbate islands.

If  $U_a < U_{as}$ , the energy balance requires to maximize the area covered by the adsorbate material and adsorbate particles prefer to form bonds with substrate particles. Here, the interplay of the substrate-adsorbate interaction and the lattice misfit plays an important role.

Below a critical misfit  $\varepsilon_c$ , layer-by-layer growth takes place during the entire growth independent of the substrate temperature, because any deviation from perfect layer-wise growth would increase the deposit surface area and cause an unnecessary increase of the total free energy. Thus, we observe the FM growth mode.

Above the critical misfit  $\varepsilon_c$ , the formation of islands on the formerly grown wetting layer becomes favorable. The resulting increase of surface energy is overcompensated by a decrease of strain energy due to the elastic strain relaxation towards the bulk lattice constant in the upper parts of the grown islands.

Again, the transition from SK to layer-wise growth can be controlled kinetically by both the lattice misfit and the substrate temperature. At a given  $\varepsilon > \varepsilon_c$ , a critical temperature  $T^*$  can be found above which SK growth takes places. At a given moderate, but high enough chosen, temperature, SK growth can be attested above a critical misfit  $\varepsilon^* > \varepsilon_c$ . The lowest possible value  $\varepsilon^* = \varepsilon_c$  is valid at high temperatures at which the adatom mobility is not limited. The flat adsorbate films grown at low temperatures are metastable for  $\varepsilon > \varepsilon_c$  and will break up upon heating and agglomerate into islands.



# Chapter 6

## Growth on bcc(100) surfaces

In the previous chapters, we have investigated the influence of strain in epitaxial systems represented on the triangular lattice. The limitation to two dimensions enables us to simulate systems with a lateral extension of several hundred atoms and the deposition of few hundred monolayers. At this point, we want to overcome that limitation by extending our model to the more realistic three dimensional case, which allows in principle for different possible lattice structures. For the majority of crystalline metals the face-centered cubic (fcc) is the usual lattice structure which is therefore topic of many investigations in theory and experiment, e.g. [32, 96, 97].

A further possible lattice structure is the simple cubic, since models with simple cubic symmetry allow for a straightforward implementation [58, 89, 95]. However, due to their conceptual simplicity these models are unsuitable to describe properties of real materials faithfully.

Another common three dimensional cubic Bravais lattice is the body centered cubic (bcc) which is the lattice structure for iron and the alkali metals. Amongst others, they play an important role in the research in magnetic thin films, where new phenomena such as enhanced magnetization at surfaces, surface and interface anisotropy have been discovered. A growing interest is focused on nanostructured films made of objects of reduced lateral dimensions like magnetic dots. These systems are of interest for fundamental investigations of magnetization processes in reduced dimensions, but also for potential applications to prospective super high-density recording media based on individual dots. Besides lithography, which is the conventional fabrication technique of such dot arrays, self-organization and self-assembly are alternatively elegant ways to produce objects of small extension and high structural quality.

The growth of iron films on tungsten have been extensively investigated in the past [98–100]. A number of studies have been reported for the self-assembled epitaxial growth of Fe islands on Mo [146–148].

In this work, we investigate the influence of the lattice misfit on growth in the submonolayer regime, since the misfit strongly affects the appearing monolayer

islands in size as well as in shape and therefore it has effect on the whole surface morphology. In order to isolate purely strain effects from those originated by the anisotropy of the surface orientation, we focus on the bcc(100) surface orientation, granting an atomic arrangement of fourfold symmetry, which is topic of many studies of epitaxial growth systems [149–152]. The main focus of this chapter is the introduction of the method allowing for off-lattice KMC simulations on the bcc lattice, which will be applied to investigate the effect of strain.

## 6.1 Simulation model

In the following, we present a model allowing for the off-lattice simulation of epitaxial growth in three dimensions on the bcc(100) surface. In conformance with the previous chapters, we use in principle the simulation method introduced in chapter 3. The necessary modifications compared to the two-dimensional realization will be discussed below.

### Definition of the potential

In contrast to the triangular and the fcc lattice structure, where the atoms are closed packed, the bcc lattice structure is unstable when using simple pair potentials in the form presented in appendix A. In order to stabilize the bcc lattice, and overcome this inconvenience, we adapt the idea of introducing an anisotropic potential. Schroeder and Wolf proposed an anisotropic potential [103] to stabilize the simple cubic lattice structure, which was successfully applied e.g. in [58, 89, 95, 103, 153].

However, the detailed realization of the anisotropic potential and its implementation in our model will be different. In the bcc lattice structure, each particle has eight nearest and six next nearest neighbors. The most important condition for the used potential is that the global relaxation procedure has to end up in a local system energy minimum when arranging particles in the bcc structure. The motivation of a stabilizing modification is as follows. Without any modification of the potential and by simply using the Lennard–Jones potential in its ordinary form, the bcc lattice is mechanically unstable to shear. Stabilizing the bcc structure just with the help of rigid boundary conditions is no solution to the problem: wrong predictions for structural stability are certainly accompanied by wrong predictions for other properties of interest.

When looking at the black particle in Fig. 6.1, the condition above is fulfilled if the modified pair potential leads to an energy minimum for the characteristic distance vectors  $\vec{a}$ , pointing to the blue particle, and  $\vec{b}$ , pointing to the red particle, with  $|\vec{b}| = \frac{\sqrt{3}}{2}|\vec{a}|$ .

We accomplish this by introducing an anisotropic distance  $\bar{r}_{ij}$  depending on the particular distance  $r_{ij}$  of two interacting particles  $i$  and  $j$ , but additionally



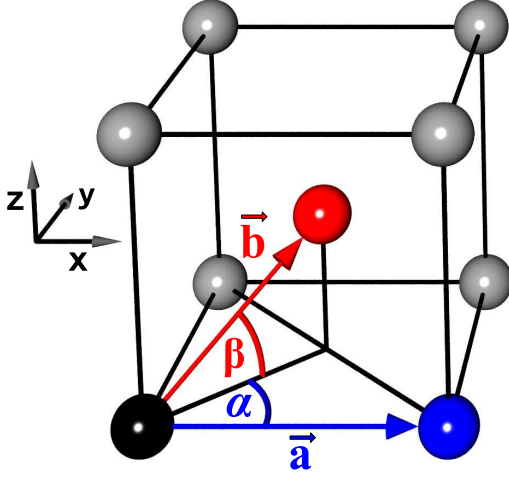


Figure 6.1: Illustration of the characteristic distances in the bcc lattice.

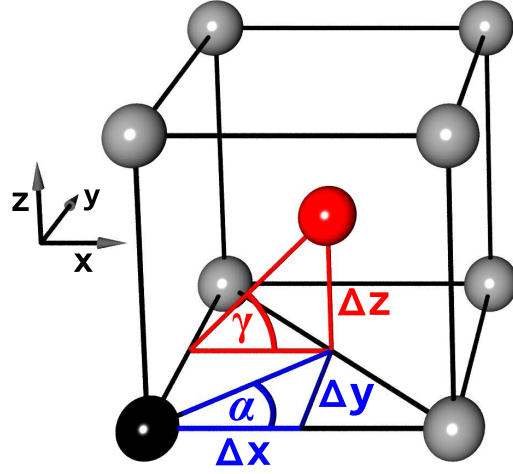


Figure 6.2: Illustration of the components of the distance vector and the relevant angles in the bcc lattice.

on the orientation in space, here denoted by the angles  $\alpha$  and  $\beta$ :

$$\bar{r}_{ij} = \bar{r}_{ij}(r_{ij}, \alpha, \beta). \quad (6.1)$$

Thus, by using the pair potentials presented in appendix A, the resulting interaction energy is given by  $U_{ij}(\bar{r}_{ij})$  with additional condition:

$$\left. \frac{\partial U_{ij}(\bar{r})}{\partial \bar{r}} \right|_{\bar{r}=\bar{a}} = \left. \frac{\partial U_{ij}(\bar{r})}{\partial \bar{r}} \right|_{\bar{r}=\bar{b}} \stackrel{!}{=} 0. \quad (6.2)$$

In Fig. 6.2, the distance vector pointing from the black to the red particle can be composed by the three components  $\Delta x$ ,  $\Delta y$  and  $\Delta z$ . With the two angles  $\alpha$  and  $\gamma$  the situation is described unambiguously. To this end, a pseudo angle  $\phi_x$  is introduced satisfying the relation

$$\cos^2 \phi_x := \cos \alpha \cos \gamma \quad (6.3)$$

$$= \frac{(\Delta x_{ij})^2}{\sqrt{((\Delta x_{ij})^2 + (\Delta y_{ij})^2) ((\Delta x_{ij})^2 + (\Delta z_{ij})^2)}}, \quad (6.4)$$

where  $\Delta x_{ij} = x_j - x_i$  denotes the  $x$ -component of the distance vector  $\vec{r}_{ij}$  of two interacting particles  $i$  and  $j$ . For overview reasons, we further define the factor

$$f_x = \frac{\sqrt{3}}{2} + \left(1 - \frac{\sqrt{3}}{2}\right) \cos^2(2\phi_x). \quad (6.5)$$

By cyclic permutation of  $x$ ,  $y$  and  $z$  the according factors  $f_y$  and  $f_z$  can be obtained and the anisotropic distance  $\bar{r}_{ij}$  fulfilling Eq. 6.2 can be written as

$$\bar{r}_{ij} = \sqrt{\left(\frac{\Delta x_{ij}}{f_x}\right)^2 + \left(\frac{\Delta y_{ij}}{f_y}\right)^2 + \left(\frac{\Delta z_{ij}}{f_z}\right)^2}. \quad (6.6)$$

The particle interaction then can be described by the now anisotropic potential  $U(\bar{r}_{ij})$ . This potential is not rotationally invariant, but for the purpose of simulating a single adatom on a crystal surface with bcc symmetry this is perfectly justified; the crystal surface breaks rotational invariance anyway and the adatom feels the directional bonds sticking out of the surface along the lattice directions.

In the following simulations, the particle interaction is described by the Lennard-Jones 12-6 potential (cf. section 3.2 ) used in the form

$$U_{ij}(U_0, \sigma, \bar{r}_{ij}) = 4 U_0 \left[ \left(\frac{\sigma}{\bar{r}_{ij}}\right)^{12} - \left(\frac{\sigma}{\bar{r}_{ij}}\right)^6 \right], \quad (6.7)$$

where  $\bar{r}_{ij}$  denotes the effective distance given by (6.6). To set the energy scale in the simulation, the potential depth is  $U_0 = 0.4 eV$  which leads to a diffusion barrier of about  $1.1 eV$  for an isolated adsorbate particle on a plane substrate surface. The concrete choice of the potential depth is of secondary importance, since the diffusion rates described by the Arrhenius law, see Eq. (2.2), are determined by the linear ratio of the potential depth and the substrate temperature. Additionally, the main focus of this work is giving qualitative insights rather than a material specific quantitative description. In order to isolate the influence of the misfit from energetic effects, we set  $U_s = U_a = U_{as}$ .

The properties we demand on our defined potential can be confirmed by a look at Fig. 6.3 which displays the variation of the equilibrium distance  $r_0$  when changing the distance vector orientation of two interacting particles. By rotating the distance vector  $\vec{r}_{ij}$  in the  $xy$ -plane, while keeping  $\Delta z = 0$ , the equilibrium distance  $r_0 = a = |\vec{a}|$  is obtained for the cases  $\alpha = 0^\circ, 90^\circ, 180^\circ, 270^\circ, 360^\circ$ , which one would expect, since these are the corner sites of the cubic shown in Fig. 6.1.

By rotating the distance vector  $\vec{r}_{ij}$  in the plane given by the  $z$ -axis and the bisecting line of the  $x$ - and  $y$ -axis ( $\alpha = 45^\circ$ ), the equilibrium distance  $r_0 = a$  is obtained for the cases  $\alpha = 90^\circ$  and  $\alpha = 180^\circ$  which are the two particles direct above and below, see Fig. 6.4. The case  $\beta = \beta_0 \approx 35.264$  represents the relation of the red and the black particle shown in Fig. 6.1. Thus, the equilibrium distance is  $r_0 = \frac{\sqrt{3}}{2}a \approx 0.867a$ , also valid for the cases  $\beta = -\beta_0$  and  $\beta = 180 \pm \beta_0$ , which confirms the conditions of our anisotropic potential. Additionally, the observed transition is continuously differentiable, a further indispensable condition for our potential.

Now, this potential can be implemented in our simulation model and enables us to calculate the potential energy surface of an isolated adatom moving on a

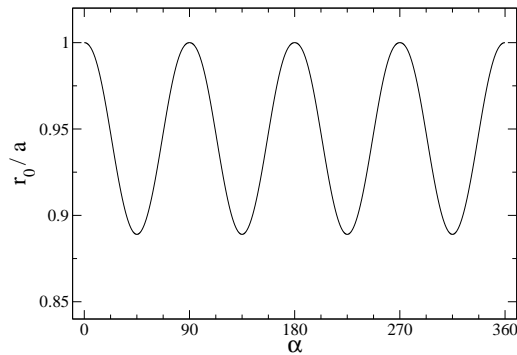


Figure 6.3: Equilibrium distance  $r_0$  in units of the distance vector  $a = |\vec{a}|$ , depicted in Fig. 6.1, as a function of the angle  $\alpha$  in the  $xy$ -plane ( $\beta = 0^\circ$ ).

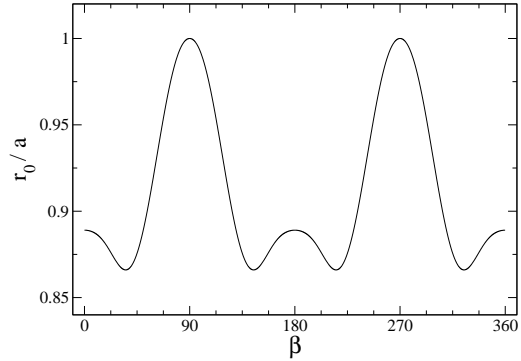


Figure 6.4: Equilibrium distance  $r_0$  in units of the distance vector  $a = |\vec{a}|$ , depicted in Fig. 6.1, as a function of the angle  $\beta$  in the plane which is given by the  $z$ -axis and the bisecting line of the  $x$ - and  $y$ -axis ( $\alpha = 45^\circ$ ).

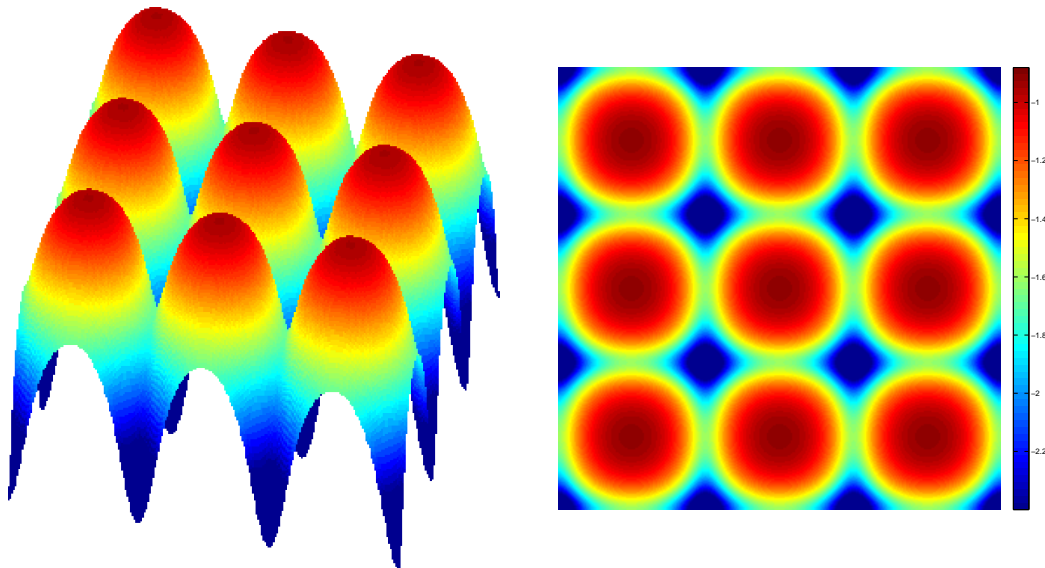


Figure 6.5: Potential energy surface of a test particle moving on the plane  $bcc(100)$  surface given as surface plot (left) and contour plot (right).

plane bcc(100) surface. The PES obtained within the frozen crystal approximation is displayed in Fig. 6.5. The figure approves the possibility to define a pair potential yielding a stable bcc structure. One can clearly see the resulting binding and transition sites, indicated by the corresponding color given in the legend. Each binding site is connected via one bridge site to four neighboring hollow binding sites. Since we focus on growth in the submonolayer regime, usually four hopping directions have to be taken into account. The determination of the neighboring binding site as well as the calculation of the transition state energy, which is needed for the calculation of the diffusion rates, are performed in the manner described in chapter 3 and applied to the triangular lattice in the previous chapters.

## 6.2 Influence of the misfit

As we have seen in the previous chapters, the lattice misfit  $\varepsilon$ , which results from the different lattice constants of the adsorbate and the substrate material, has strong influence on the potential energy surface of an adatom and therefore affects the whole surface morphology. In this section, we study the influence of the misfit on growth typical diffusion processes as well as the effect of strain on submonolayer islands. Afterwards, the consequences arising out of these strain effects are investigated in the submonolayer growth regime with respect to the island density and the occurring shape of islands.

### 6.2.1 Influence on the potential energy

The most general and most frequently observed diffusion process is the diffusion of an isolated adatom on the plane substrate surface. Fig. 6.6 shows the binding site potential energy and the transition state potential energy as a function of the misfit for that scenario. Both curves decrease monotonically for increasing misfit. In the considered range, the progression is approximately linear which is in good agreement with theoretical and experimental findings [37, 97, 153, 154]. Fig. 6.7 shows the resulting activation energy as a function of the misfit, again a monotonic decrease can be observed.

In the temporal evolution of the growing system, the adatoms nucleate to submonolayer islands which are strained due to the lattice mismatch between adsorbate and substrate. To study the strain behavior by means of our simulation model, we place a symmetric submonolayer island of adsorbate material on top of the substrate and minimize the system energy to its next local minimum. Fig. 6.8 shows exemplarily a strained symmetric island of size  $L = 11$  with  $\varepsilon = 12.0\%$  which is chosen to be that high due to illustration purposes. One can clearly see that the strain built up in the islands is released at the island edges, indicated by the increased lateral particle distance towards the island edges. Additionally,

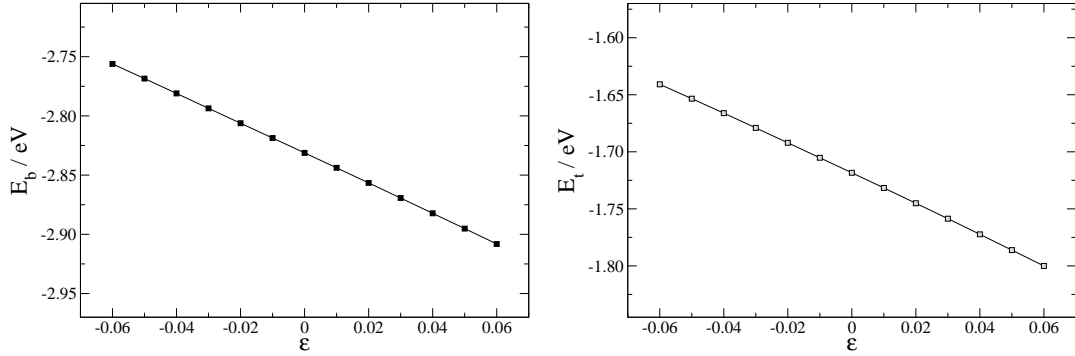


Figure 6.6: Binding energy  $E_b$  (left) and transition state  $E_t$  (right) vs. misfit  $\epsilon$  for an isolated adatom on top of the substrate.

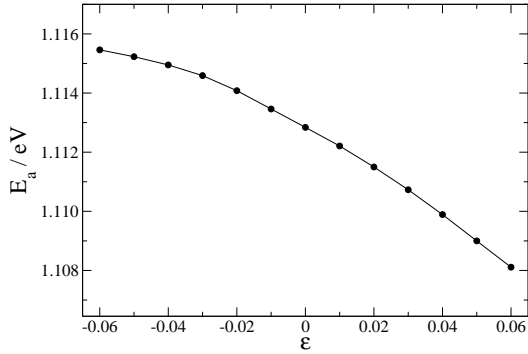


Figure 6.7: Activation energy  $E_a$  as a function of the misfit  $\epsilon$  for an isolated adatom on top of the substrate.

the strain relief is performed in a symmetric way, independent of the orientation of the island edge.

This qualitative observation is confirmed quantitatively by a look at the particle row in the center of the island, marked by the black dashed line in Fig. 6.8. The displacement of these island particles from the potential well minima, caused by the underlying substrate, is plotted in Fig. 6.9 as a function of the island size for a system with positive misfit  $\epsilon = 4.0\%$ . The behavior is in accordance with the two dimensional case discussed in section 5.2. While the particles in the center of the island are blocked up in the lateral direction and change their lateral positions only slightly, the strain is released by the lateral displacement of the particles close to the island edges. The only possibility of a particle in the center is adjusting its position in the vertical direction, but keeping the lateral position of the fourfold hollow sites. This observed strain relief behavior is in good agreement with the reported behavior of strain relief of heteroepitaxial bcc-Fe(001) films [155]. Since the outermost edge particles are displaced in the lateral direction, their vertical displacement is decreased.

For large islands, the restrained mobility of the island center particles leads to decreased displacement in lateral as well as in vertical direction for increasing island size. Note that the relaxation towards island corners is even more pronounced.

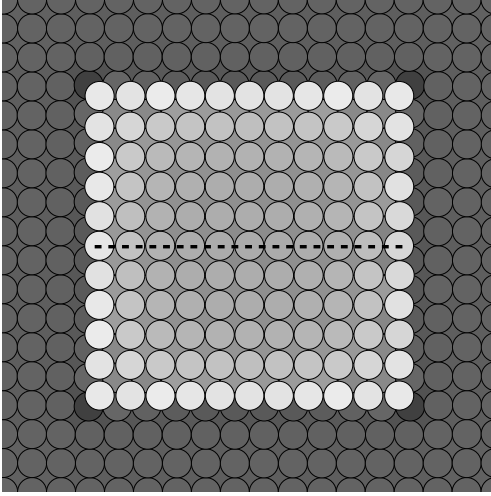


Figure 6.8: Strained adsorbate island of size  $L = 11$  placed on top of the substrate. The misfit is chosen to be  $\varepsilon = 12.0\%$ . The snapshot shows a section of a larger system. The grey level of a particle indicates the average distance to its nearest neighbors. The lighter a particle is drawn, the larger this distance is.

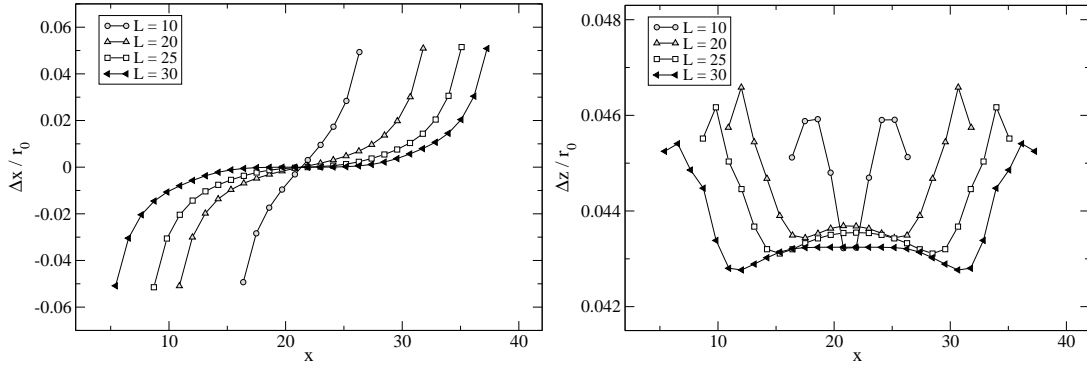


Figure 6.9: Displacement from the potential well minima position, caused by the underlying substrate, in lateral ( $\Delta x$ ) and vertical direction ( $\Delta z$ ) as a function of the lateral monolayer island size  $L$  with misfit  $\varepsilon = 4.0\%$ .

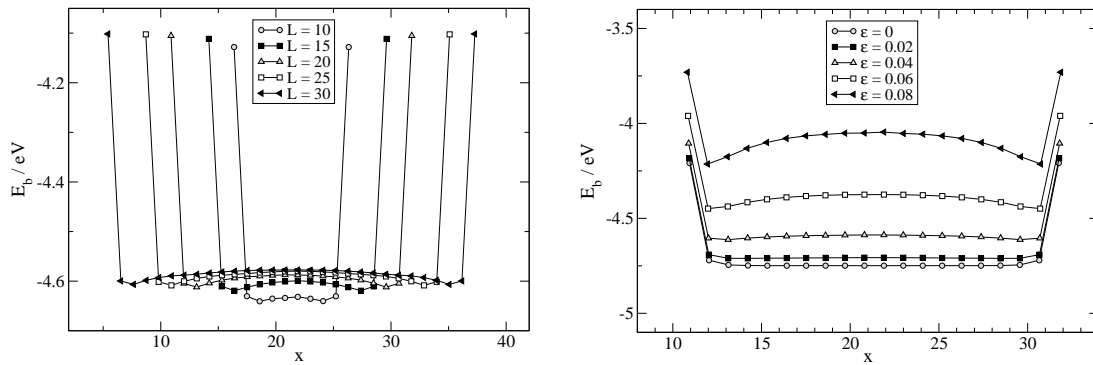


Figure 6.10: Binding energy distribution of island particles at the lateral position  $x$  for different island sizes  $L$  and misfit  $\varepsilon = 4.0\%$ .

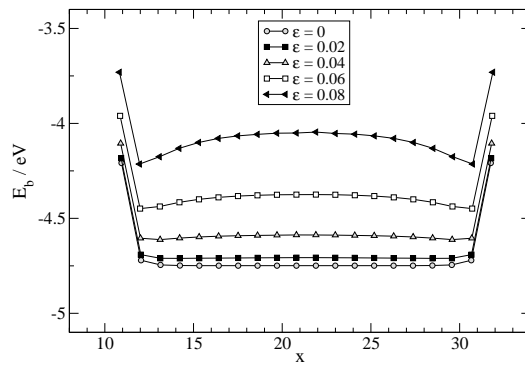


Figure 6.11: Binding energy distribution of island particles at the lateral position  $x$  for different values of  $\varepsilon$  and island size  $L = 20$ .

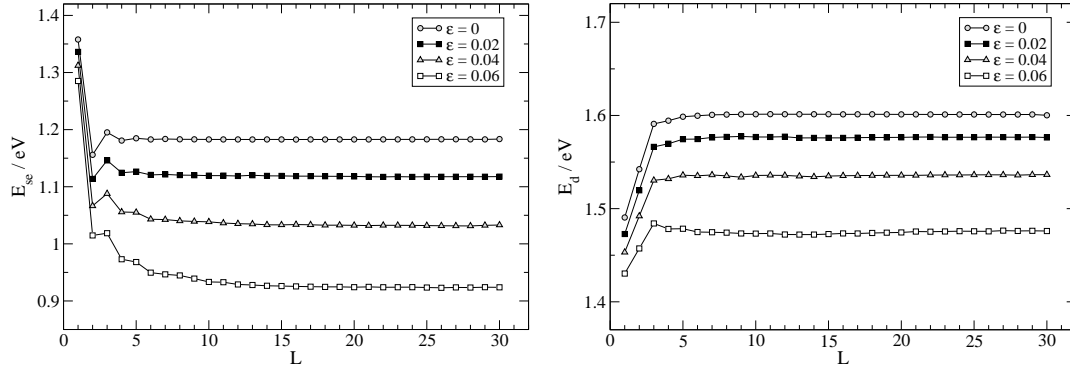


Figure 6.12: Activation energy for step edge diffusion  $E_{se}$  (left) and for the process of particles detaching from the step edge  $E_d$  (right) vs. island size  $L$  for several values of  $\varepsilon$ .

In Fig. 6.10 the binding energy distribution of island particles is shown for several island sizes with misfit  $\varepsilon = 4.0\%$ . The larger the submonolayer island is, the weaker the particles are bound. In addition, particles closer to the island edge are bound stronger. This effect is amplified for higher values of  $\varepsilon$ , see Fig. 6.11.

Besides the diffusion of an isolated particle on the plane surface, a frequently appearing kinetic process is the step edge diffusion. The strain relaxation at the island edges directly influences both the step edge diffusion and the detaching process of a particle from the edge which are displayed in Fig. 6.12.

For very small island sizes the particle feels the limited size of the island which thus affects the considered barriers. For larger islands, the step edge diffusion barrier and the barrier for detaching decrease with increasing misfit, since island edge particles are displaced due to the strain relaxation, as discussed above. For high enough chosen  $\varepsilon$  the step edge diffusion is even faster than the diffusion of an isolated particle on the plane substrate surface. This behavior is also observed in off-lattice simulations on the fcc lattice [97].

### 6.2.2 Characterization of submonolayer islands

The described influence of the misfit on growth in submonolayer regime affects the nucleating adsorbate islands. The strain in islands favors the step edge diffusion and one expects that the higher the misfit is chosen the smoother the island edges are. Furthermore, islands should appear more compact with smoother edges in the presence of misfit.

At this point, we set the particle flux to  $F = 0.001 MLs^{-1}$ . Fig. 6.13 shows typical surface topologies grown with and without lattice misfit for two different substrate temperatures, simulated on a system consisting of a  $12 ML$  thick substrate film with lateral size  $L = 40$  and periodic boundary conditions in the two

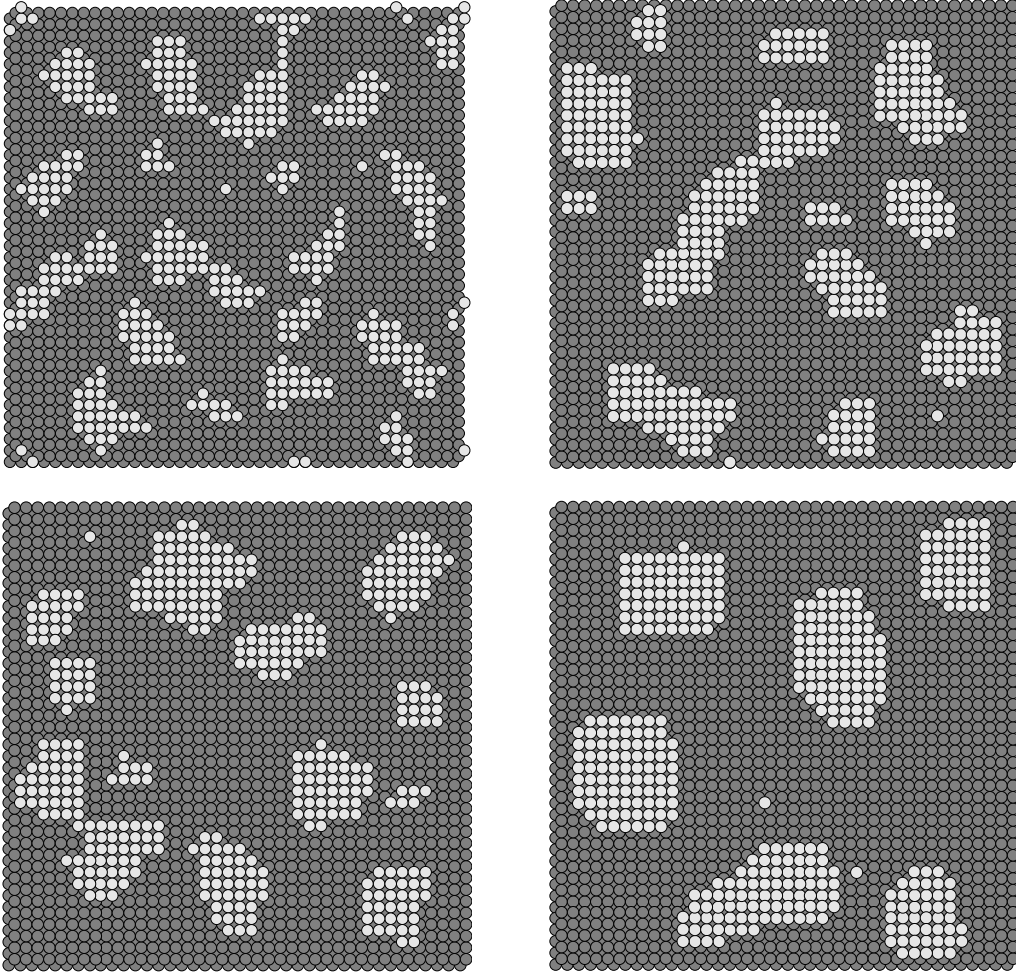


Figure 6.13: Surface topology at substrate coverage  $c = 0.25 ML$  with misfit  $\varepsilon = 0$  (left) and  $\varepsilon = 6.0\%$  (right), and substrate temperature  $T = 500 K$  (top) and  $T = 550 K$  (bottom). The darker particles represent the substrate, the lighter particles are adsorbate particles.

lateral directions. Due to the facilitated step edge diffusion, the adsorbate islands grown with  $\varepsilon = 6.0\%$  reveal a more compact shape with smooth edges compared to the system grown without misfit whose islands are more ramified. In addition, a smoothing effect on the island edges can also be achieved by increasing the substrate temperature, see Fig. 6.13. In the following, the substrate temperature is set to  $T = 500 K$ .

The smoothing effect of the misfit on the island shape, caused by the decreased step edge diffusion barrier, can be documented in a more quantitative way by the part of all adsorbate particles belonging to the border of islands. The ratio of border particles to all adsorbate particles as a function of the substrate coverage  $c$  is displayed in Fig 6.14 for different values of  $\varepsilon$ .



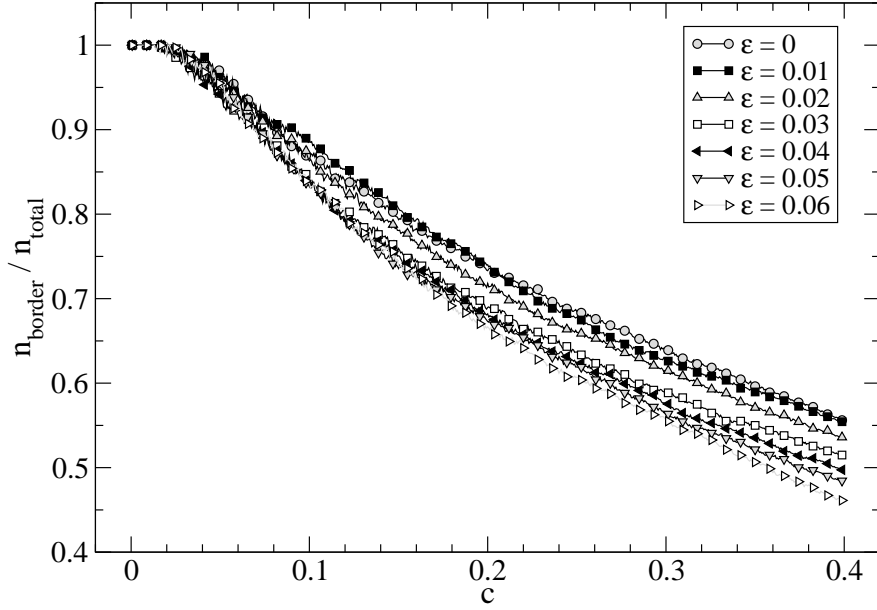


Figure 6.14: Ratio of number of border particles  $n_{border}$  to total number of adsorbate particles  $n_{total}$  as function of the substrate coverage  $c$  for different values of  $\varepsilon$ . For each value of  $\varepsilon$ , at least 10 independent simulation runs were carried out.

Here, border particles are defined as particles with less than four in-plane nearest neighbors, thus including all particles with at least one free lateral neighboring site. In the initial phase, all adsorbate particles can be identified as border particles, since monolayer islands just have nucleated. In the further evolution, the part of border particles decreases monotonically in all cases, whereas the higher the misfit is the faster the part of border particles decreases, originated by the facilitated step edge diffusion and yielding compacter islands. Besides the statistical fluctuations which appear especially in the initial growth phase, the described behavior becomes clearly apparent at substrate coverage  $c > 0.3 ML$ .

### 6.2.3 Evolution of the island density

Besides the smoothing effect on the island shape, we have seen that the misfit also affects the diffusion of isolated adatoms on the substrate, see Fig. 6.7. The activation energy decreases with increasing misfit and we can presume that also the monolayer island density decreases which is supported by comparing the two misfit cases shown in Fig. 6.13.

The island density is a proper tool for the characterization of the nucleation kinetics and the development of the system in the submonolayer regime. At the beginning of the deposition, the so-called nucleation regime, the density of nuclei steadily increases as a function of the coverage. In the further progress,

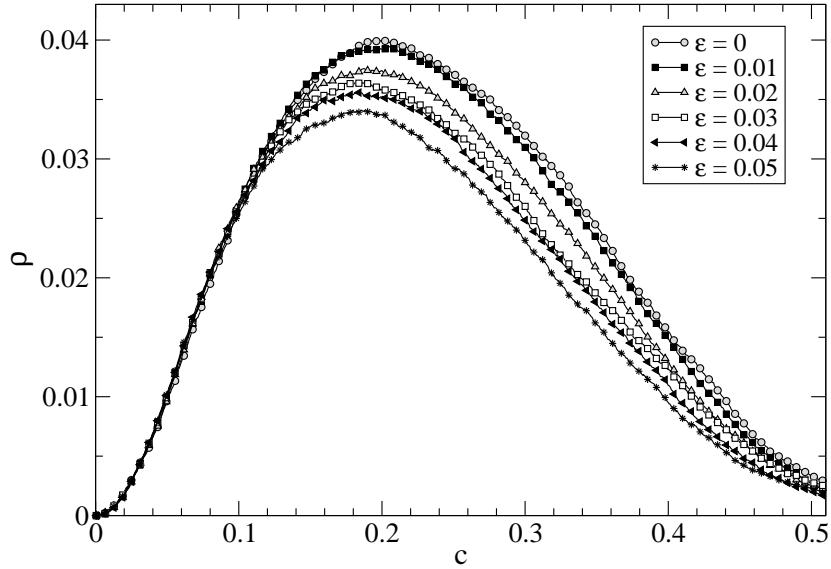


Figure 6.15: Island density  $\rho$  vs. substrate coverage  $c$  for different values of  $\varepsilon$ . For each value of  $\varepsilon$ , at least 10 independent simulation runs were carried out.

it becomes more probable that diffusing particles attach already existing islands rather than forming new ones. In this aggregation regime, the density stays more or less constant for a wide range of coverage.

Due to the ongoing deposition of further adsorbate material, the islands grow laterally and begin to coalesce which leads to a decrease of the island density. The saturation island density  $\rho_{sat}$ , given by the maximum of the curve, is determined by the ratio of diffusivity to the deposition flux and therefore a measure for the adatom mobility [156]. The island density is defined as the number of adsorbate islands per available lattice sites on the substrate and is given in our simulations as  $\rho = N_{island}/L^2$ . The mean island distance can be regarded as an estimate for the mean free path of the diffusing particles.

Due to the high computer time costs, we are limited to comparable small system sizes, and in the following we set  $L = 60$ . To ensure that a sufficiently high number of islands occur in the submonolayer regime we set the particle flux  $F = 1 MLs^{-1}$  and the substrate temperature  $T = 520 K$ . This set of parameters yields a reduced adatom mobility and the low mean free path, which needs to be significant smaller than the system size to exclude finite size effects, favors frequent nucleation of islands. As a consequence, the island density increases fast at the beginning of the growth and the saturation island density can be identified as a maximum rather than a constant plateau. Fig. 6.15 shows the island density  $\rho$  as a function of the substrate coverage for different values of  $\varepsilon$ . In the initial phase, the island density increases fast due to the nucleation of islands and the trend becomes apparent for substrate coverage at above  $c \approx 0.1 ML$ . Due to

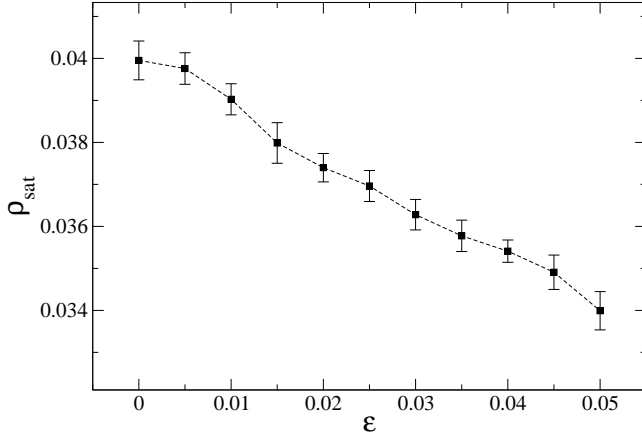


Figure 6.16: Saturation island density  $\rho_{sat}$  vs. misfit  $\varepsilon$  simulated at substrate temperature  $T = 520 K$ . For each value of  $\varepsilon$ , at least 10 independent simulation runs were carried out. The error bars represent the standard errors of the simulation results.

the facilitated surface diffusion, the island density slope decreases and ends up in a smaller saturation island density when increasing the misfit, which is in accordance with the behavior displayed in Fig. 6.7. In addition, the higher the misfit is chosen, the earlier the saturation density is reached.

The saturation island density  $\rho_{sat}$  is displayed in Fig. 6.16 as a function of the misfit. The values are obtained by fitting the relevant regime close to the maximum approximately with a quadratic function. The error bars only represent the standard errors of the simulation results and do not include the additional uncertainty caused by the fit. As a qualitative result, one can see that the island density decreases with  $\varepsilon$ , however the limited amount of data does not allow to determine the functional behavior, since the island density is affected by both the adatom mobility and the smoothing character caused by step edge diffusion. If a more qualitative analysis is desired, the consideration of more simulation runs and larger systems is indispensable. However, this would demand a lot of computer power and goes beyond the scope of this work.

The island density is also affected by the substrate temperature. The adatom mobility is increased at higher temperatures and a higher free mean path is expected. The influence of the temperature on the island density behavior, which can be seen in Fig. 6.17, confirms our expectation: the saturation island density decreases with increasing temperature.

## 6.3 Conclusions

In this chapter, we have extended our simulation model to the more realistic three dimensional case. Since we are interested in the off-lattice simulation of epitaxial growth on the bcc(100) lattice, the form of the interaction potential used to describe growth on the two dimensional triangular lattice, applied in the previous chapters 4 and 5, is inapplicable for the three dimensional bcc lattice structure representation. Based on this condition, an adjustment of the particle

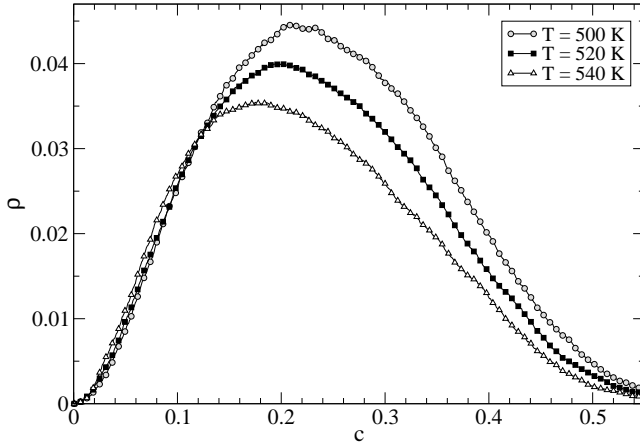


Figure 6.17: Island density  $\rho$  vs. substrate coverage  $c$  for three different values of  $T$  in the absence of misfit. For each value of  $T$ , at least 10 independent simulation runs were carried out. The error bars represent the standard errors of the simulation results.

interaction potential is required in order to provide for a stable bcc structure when minimizing the system energy.

To this end we have introduced an anisotropic potential yielding a stable bcc lattice structure within the off-lattice representation, motivated by the fact that the crystal surface breaks rotational invariance and the adatom feels the directional bonds sticking out of the surface along the lattice directions.

By applying this adjusted model to heteroepitaxial growth in the submonolayer regime, we have investigated the effect of strain, caused by the lattice misfit between adsorbate and substrate, on the surface morphology. We have shown that the strain built up in submonolayer islands is mainly released at the island edges, indicated by the particle displacement from the potential well minima, caused by the underlying substrate.

The lattice misfit has strong influence on the diffusion process which affects the adatom mobility on the plane surface as well as the situation at the island edges. The saturation island density decreases with increasing misfit and increasing substrate temperature. Furthermore, in the presence of misfit the step edge diffusion is facilitated which leads to less ramified island edges and to a more compact island shape.

# Chapter 7

## Conclusions and outlook

In the framework of this thesis, we have investigated the influence of strain on heteroepitaxial growth. Due to the different lattice constants of the adsorbate and the substrate material, the resulting long-range elastic strain has pronounced effect on the entire crystal. The computational realization of heteroepitaxial growth was accomplished by means of Kinetic Monte Carlo simulations. By using an off-lattice simulation model, the particles are not restricted to predefined lattice sites which thus enables us to study strain effects in systems with lateral extension of several hundred atoms and the deposition up to few hundred layers of adsorbate material. Our model is capable of reproducing various important aspects observed in experimental studies. In order to give reliable information about the observed growth phenomena maintained by statistical manifestations, the main part of this work was realized on the two dimensional triangular lattice, which can be treated as a cross section of the real three dimensional case.

As a first result, we have seen that one possible strain relaxation mechanism is the introduction of misfit dislocations above a critical adsorbate film thickness. The detailed formation of dislocations depends strongly on the sign and the magnitude of the misfit. For positive values of the misfit, as well as for moderate values of negative misfit, the dislocations nucleate between two adjacent mounds and keep their vertical positions after they are built. In the case of small values of negative misfit the formation mechanism is different. The dislocations are initially formed at the surface, but glide down to the substrate adsorbate interface by the concerted motion of a large number of atoms leading to insertion of an extra lattice row into an already continuous film. The transition between these two observed mechanisms turned out to be continuous, while the tensile-compressive asymmetry originates from the strong anharmonicity of the interaction potential, particularly in the steeply rising repulsive core. In addition, the observed formation mechanism is determined by the surface kinetics, since the formation of dislocation is favored by the presence of mounds.

Furthermore, we have shown that the dislocations immediately affect the vertical and the lateral lattice spacings of the system indicating the strain relaxation.

The average vertical lattice spacing approaches continuously the undisturbed bulk value when the misfit is positive. This is in qualitative agreement with experimental data. For negative misfit, the average vertical lattice spacing approaches the bulk adsorbate value in a discontinuous manner when looking at a single system, since dislocations glide down to the adsorbate-substrate interface immediately after their nucleation and therefore affect the whole grown film. However, the influence of a single dislocation is reduced in larger systems, as well as when averaging over many simulation runs, and the behavior is approximately continuous.

The misfit dislocations additionally affect the subsequent growth of the adsorbate film. We observe a clear correlation between the lateral positions of buried dislocations and the positions of mounds grown on the surface which depends decisively on the sign of the misfit. The interplay of the regularly arranged dislocations leads to a periodic modulation of the potential energy surface whose intensity decreases with increasing film thickness. In the case of positive misfit the mounds are preferentially formed laterally direct above buried dislocations, in the case of negative misfit mounds grow between the lateral positions of the dislocations. The optimal growth temperature is crucial since the self-organization can be destroyed at too high temperatures.

An alternative strain relaxation mechanism is the formation of three dimensional islands enabling the adsorbate particles to approach their preferred lattice spacing. In summary, we have demonstrated that it is possible to adjust within our simulation model each of the three epitaxial growth modes: Volmer–Weber, Frank–van der Merve or layer-by-layer, and Stranski–Krastanov growth mode. The two decisive parameters are the lattice misfit and the strength of the mixed interaction of adsorbate and substrate particles.

By choosing the interaction of adsorbate particles to each other stronger than to substrate particles, and in accordance with energetic considerations in the thermodynamic limit, the Volmer–Weber growth mode can be realized. A key role in this scenario play the surface kinetics. Layer-wise growth can be adjusted by growing metastable flat adsorbate films at low temperatures which break up upon heating and agglomerate into islands. This transition can also be accomplished by increasing the lattice misfit when choosing the particle flux and the substrate temperature in an appropriate manner.

By choosing the interaction of adsorbate particles to each other weaker than to substrate particles, the interplay of the mixed interaction and the lattice misfit plays the decisive role. Below a critical misfit, layer-by-layer growth takes place during the entire growth independent of the substrate temperature, because any deviation from perfect layer-wise growth would increase the deposit surface area and cause an unnecessary increase of the total free energy. Thus, the Frank–van der Merve growth mode is observed. Above the critical misfit the formation of islands on a stable wetting layer becomes favorable and Stranski–Krastanov growth occurs. The resulting increase of surface energy is overcompensated by

---

a decrease of strain energy due to the elastic strain relaxation towards the bulk lattice constant in the upper parts of the grown islands. For misfit values beyond the critical misfit the transition from SK to layer-wise growth can be controlled kinetically, since flat adsorbate films grown at low temperatures are metastable and will break up upon heating and agglomerate into islands.

Besides the two dimensional realization, we extended our model to three dimensions and investigated the effect of strain on growth on bcc(100) surfaces. To this end, we have introduced an anisotropic potential yielding a stable bcc lattice structure within the off-lattice representation. We have shown that the strain built up in submonolayer islands is mainly released at the island edges and the lattice misfit has strong influence on the diffusion process on the plane surface as well as on the situation at the island edge. The misfit facilitates the step edge diffusion leading to less ramified island edges and to a more compact island shape.

In conclusion, the formation of nanostructures controlled by an underlying dislocation network as well as the tendency to form ordered arrays of strain-induced three dimensional grown islands can be applied in the concept of self-organized pattern formation. Whether coherently strained islands are observed prior to dislocation formation depends on the ratio between change in surface energy due to island formation and the energy of the dislocated interface.

In summary, we were able to gain insight into relevant mechanisms of self-organized island formation and to identify the decisive control parameters, but still leaving interesting questions. One point of interest is the implementation of unconsidered kinetic processes like the intermixing of substrate and adsorbate, the possibility of concerted moves, the exchange diffusion process as well as the desorption of adatoms, which are disregarded so far due to the enormous expenditure of simulation time.

A further interesting point is investigating the dislocation formation as well as the simulation of the growth modes in the more realistic three-dimensional case. Besides regarding larger systems with different possible lattice structures, the pair potentials should be replaced by more realistic empirical potentials, which is currently beyond computational means.

Nevertheless, our model is capable to regard the typical time and length scales of epitaxial growth which cannot be delivered by means of density functional theory or molecular dynamics. Furthermore, it gives insight in details of the underlying atomistic mechanisms through which e.g. dislocations occur which is not delivered within the continuum elastic theory.





# Appendix A

## Pair-potentials

In order to determine the rates for the relevant kinetic processes in heteroepitaxial growth, one has to calculate the potential energy of the system for a given surface configuration.

In this work the interaction of the particles is described by simple pair potentials that are numerically easy to handle and enable the simulation of heteroepitaxial growth in a satisfying time and length scale. The chosen potential reflects the behavior of neutral atoms and molecules showing a repulsive behavior in the limit of short distances, an attractive behavior at intermediate distances and is zero in the limit of long distances [157].

### A.1 The Lennard–Jones potential

A simple model representing the desired behavior is the Lennard–Jones potential [158] given in the general form [159]

$$U_{ij}(U_0, r_0, r_{ij}) = U_0 \left[ \frac{m}{n-m} \left( \frac{r_0}{r_{ij}} \right)^n - \frac{n}{n-m} \left( \frac{r_0}{r_{ij}} \right)^m \right] \quad n > m \quad (\text{A.1})$$

depending on the distance  $r_{ij}$  of the two interacting particles  $i$  and  $j$ , where  $U_0$  denotes their dissociation energy and  $r_0$  the equilibrium distance. In this form, the potential has four adjustable parameters,  $n$ ,  $m$ ,  $U_0$ , and  $r_0$ , which can be evaluated from available physical property data for all materials whose crystal structure is body-centered cubic, face-centered cubic or close-packed hexagonal [159]. In Fig. A.1 the potential is plotted for different values of  $m$  and  $n$ . The higher these two parameters are chosen the steeper the form of the potential valley is. The most common form of the Lennard–Jones potential is the case  $n = 12$  and  $m = 6$ , motivated by van der Waals interactions, and can be written as

$$U_{ij}(U_0, \sigma, r_{ij}) = 4 U_0 \left[ \left( \frac{\sigma}{r_{ij}} \right)^{12} - \left( \frac{\sigma}{r_{ij}} \right)^6 \right], \quad (\text{A.2})$$

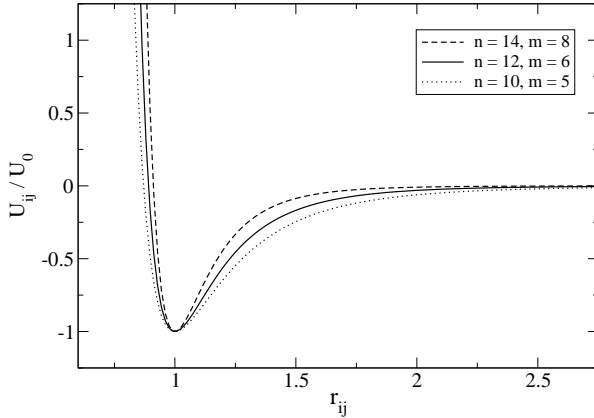


Figure A.1: Lennard–Jones potential for different values of  $n$  and  $m$  and  $r_0 = 1$ .

where  $\sigma$  is the distance at which the potential is equal to zero and specifies the different material properties in the model. The equilibrium distance of two isolated particles is direct proportional to  $\sigma$  in the form

$$r_0 = 2^{1/6} \sigma. \quad (\text{A.3})$$

The Lennard–Jones potential is a relatively good approximation and often used to describe the properties of gases and it is particularly accurate for noble gases with fitted values of  $U_0$  and  $\sigma$  [160]. In quantum mechanical terms the repulsive behavior is due to the overlap of the electronic wave functions of the two considered atoms where the electrons repel because of their negative charge. The origin of the attraction is the electron correlation, due to induced dipole-dipole interaction. This attraction varies as the inverse sixth power of the distance between the two atoms [157].

## A.2 The Morse potential

Besides the Lennard–Jones potential, an alternative and often used pair potential obeying the general requirements is the Morse potential [161], first proposed in the form

$$U_{ij}(U_0, \sigma, r_{ij}) = U_0 e^{-2a(r_{ij}-\sigma)} - 2U_0 e^{-a(r_{ij}-\sigma)}, \quad (\text{A.4})$$

depending on the distance  $r_{ij}$  of the two interacting particles  $i$  and  $j$ , where again  $U_0$  denotes the depth of the potential, and the equilibrium distance between two isolated particles becomes  $r_0 = \sigma$ . The parameter  $a$  controls the steepness of the potential, which is illustrated in Fig. A.2. High values of  $a$  lead to a potential with a steeper attractive and a steeper repulsive contribution.

If one is also interested in changing the degree of anharmonicity, a more generalized form, proposed by Markov and Trayanov [162], can be used

$$U_{ij}(U_0, \sigma, r_{ij}) = U_0 \left( \frac{\nu}{\nu - \mu} e^{-\mu(r_{ij}-\sigma)} - \frac{\mu}{\nu - \mu} e^{-\nu(r_{ij}-\sigma)} \right), \quad (\text{A.5})$$

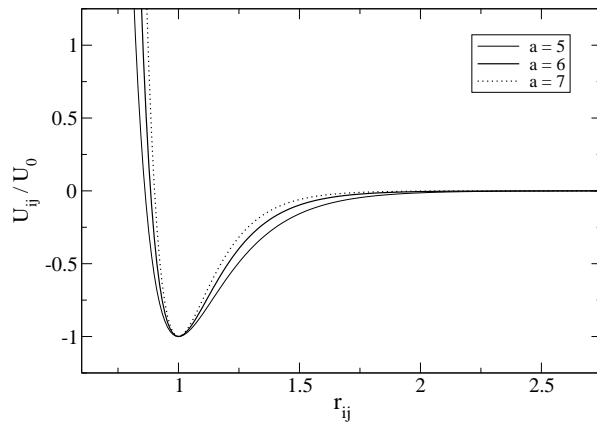


Figure A.2: Morse potential for different values of  $a$  and  $\sigma = 1$ .

where fitting parameters  $\nu$  and  $\mu$  replace  $a$ . In the limit of small distances the Morse potential stays finite, in contrast to the Lennard–Jones potential, but still sufficient high to represent the repulsive character by a proper choice of the parameter  $a$ . Especially in the repulsive region of van der Waals interactions, the Morse potential gives a better fit than the Lennard–Jones potential [163]. The behavior of the attractive part of the potential is very similar for both functions.



# Bibliography

- [1] P. M. Chaikin and T. C. Lubensky. *Principles of condensed matter physics*. Cambridge University Press, Cambridge, 1995.
- [2] L. Royer. Recherches expérimentales sur l'épitaxie ou orientation mutuelle de cristaux d'espèces différentes. *Bull. Soc. franç. Minér. Crist.*, 51:7–159, 1928.
- [3] M. A. Herman. *Semiconductor Superlattices*. Akademie- Verlag, Berlin, 1986.
- [4] K. Ploog. Molecular beam epitaxy of semiconductor quantum wells and superlattices. *J. Cryst. Growth*, 79:887–899, 1986.
- [5] M. A. Herman and H. Sitter. *Molecular Beam Epitaxy - Fundamentals and Current Status*. Springer, 2nd edition, Berlin, 1996.
- [6] W. Braun. *Applied RHEED. Reflection High-Energy Electron Diffraction During Crystal Growth: Reflection High-energy Electron Diffraction During Crystal Growth*. Springer, Berlin, 1999.
- [7] E. H. C. Parker (editor). *The Technology and Physics of Molecular Beam Epitaxy*. Plenum Press, New York, 1985.
- [8] A. L. Barabási and H. E. Stanley. *Fractal Concepts in Surface Growth*. Cambridge University Press, Cambridge, 1995.
- [9] A. Pimpinelli and J. Villain. *Physics of Crystal Growth*. Cambridge University Press, Cambridge, 1998.
- [10] K. Oura, V. G. Lifshits, A. A. Saranin, and M. Katayama A. V. Zotov. *Surface Science - An Introduction*. Springer, Berlin, 2003.
- [11] G. Le Lay and R. J. Kern. Physical methods used for the characterization of modes of epitaxial growth from the vapor phase. *J. Cryst. Growth*, 44:197–222, 1978.

- 
- [12] E. Bauer. Phänomenologische Theorie der Kristallabscheidung an Oberflächen. *Zeitschrift für Kristallographie*, 110:372 – 431, 1958.
- [13] A. Madhukar. Far from equilibrium vapour phase growth of lattice matched III-V compound semiconductor interfaces: Some basic concepts and monte-carlo computer simulations. *Surf. Sci.*, 132:344–374, 1983.
- [14] T. Michely and J. Krug. *Islands, Mounds and Atoms - Patterns and Processes in Crystal Growth far From Equilibrium*. Springer, Berlin, 2004.
- [15] W. F. Egelhoff and I. Jacob. Reflection high-energy electron diffraction (RHEED) oscillations at 77 K. *Phys. Rev. Lett.*, 62(8):921–924, 1989.
- [16] J. W. Evans, D. E. Sanders, P. A. Thiel, and A. E. DePristo. Low-temperature epitaxial growth of thin metal films. *Phys. Rev. B*, 41(8):5410–5413, 1990.
- [17] Y. Shim and J. G. Amar. Effects of shadowing in oblique-incidence metal (100) epitaxial growth. *Phys. Rev. Lett.*, 98(4):046103, 2007.
- [18] M. Walther, M. Biehl, and W. Kinzel. Formation and consequences of misfit dislocations in heteroepitaxial growth. *Phys. Stat. Sol. (c)*, 4(9):3210–3220, 2007.
- [19] M. Biehl, F. Much, and C. Vey. Off-lattice Kinetic Monte Carlo simulations of heteroepitaxial growth. In A. Voigt, editor, *Multiscale Modeling in Epitaxial Growth, International Series of Numerical Mathematics*, volume 149, pages 41 – 57. Birkhäuser, 2005.
- [20] M. Ahr. *Surface properties of epitaxially grown crystals*. PhD thesis, Bayerische Julius-Maximilians-Universität Würzburg, Würzburg, 2002.
- [21] J. W. Evans. Factors mediating smoothness in epitaxial thin-film growth. *Phys. Rev. B*, 43(5):3897–3905, 1991.
- [22] F. Bechstedt. *Principles of Surface Physics*. Springer, Berlin, 2003.
- [23] P. J. Feibelman. Diffusion path for an Al adatom on Al(001). *Phys. Rev. Lett.*, 65(6):729–732, 1990.
- [24] J. D. Wrigley and G. Ehrlich. Surface diffusion by an atomic exchange mechanism. *Phys. Rev. Lett.*, 44(10):661–663, 1980.
- [25] G. Kellog and P. J. Feibelman. Surface self-diffusion on pt(001) by an atomic exchange mechanism. *Phys. Rev. Lett.*, 64(26):3143–3146, 1990.

- 
- [26] C. Chen and T. T. Tsong. Displacement distribution and atomic jump direction in diffusion of ir atoms on the ir(001) surface. *Phys. Rev. Lett.*, 64(26):3147–3152, 1990.
- [27] J. P. Hirth and J. Lothe. *Theory of Dislocations*. Krieger Publishing Company, 1992.
- [28] A. T. Blumenau. *The Modelling of Dislocations in Semiconductor Crystals*. PhD thesis, Universität Paderborn, Paderborn, 2002.
- [29] J. de la Figuera, K. A. K. Schmid, K. Pohl, N. C. Bartelt, C. B. Carter, and R. Q. Hwang. Glide and Climb of Dislocations in Ultra-Thin Metal Films. *Mat. Sci. Forum*, 426-432:3421, 2003.
- [30] J. W. Matthews. The Observation of Dislocations to Accommodate the Misfit between Crystals with Different Lattice Parameten. *Philos. Mag.*, 6(71):1347–1349, 1961.
- [31] J. W. Matthews. The Climb and Glide of Misfit Dislocations. *Philos. Mag.*, 8(88):711–713, 1963.
- [32] W. Palmberg and T. N. Rhodin. Auger electron spectroscopy of fcc metal surfaces. *J. Appl. Phys.*, 39(5):2425–2432, 1968.
- [33] D. C. Jackson, T. E. Gallon, and A. Chambers. A model for the auger electron spectroscopy of systems exhibiting layer growth, and its application to the deposition of silver on nickel. *Surf. Sci.*, 36(2):381–394, 1973.
- [34] D. E. Jesson. Morphological evolution of strained semiconductor films. In Z. Zhang and M. G. Lagally, editors, *Morphological Organization in Epitaxial Growth and Removal*, pages 195–212, Singapore, 1998. World Scientific.
- [35] B. Voigtländer. Fundamental processes in Si/Si and Ge/Si epitaxy studied by scanning tunneling microscopy during growth. *Surf. Sci. Rep.*, 43:127–254, 2001.
- [36] C. Teichert. Self-organization of nanostructures in semiconductor heteroepitaxy. *Phys. Rep.*, 365:335–432, 2002.
- [37] H. Brune. Microscopic view of epitaxial metal growth: nucleation and aggregation. *Surf. Sci. Rep.*, 31:121–229, 1998.
- [38] B. Poelsema and G. Comsa. *Scattering of Thermal Energy Atoms from Disordered Surfaces*. Springer Tracts in Modern Physics. Springer-Verlag, Berlin, 1989.

- [39] P. K. Larsen and P. J. Dobson, editors. *Reflection High-Energy Electron Diffraction and Reflection Electron Imaging of Surfaces*. Nato ASI Series B. Plenum Press, New York, 1988.
- [40] D. D. Vvedensky. Epitaxial phenomena across length and time scales. *Surf. Interface Anal.*, 31:627–636, 2001.
- [41] H. Jónsson. Theoretical studies of atomic-scale processes relevant to crystal growth. *Annu. Rev. Phys. Chem.*, 51:623–653, 2000.
- [42] M. Biehl. Lattice gas models and Kinetic Monte Carlo simulations of epitaxial growth. In A. Voigt, editor, *Multiscale Modeling in Epitaxial Growth, International Series of Numerical Mathematics*, volume 149, pages 3–18. Birkhäuser, 2005.
- [43] M. Kotrla. Numerical simulations in the theory of crystal growth. *Comput. Phys. Commun.*, 97:82–100, 1996.
- [44] D. D. Vvedensky. Multiscale modelling of nanostructures. *J. Phys. - Condens. Mat.*, 16(50):R1537–R1576, 2004.
- [45] R. M. Dreizler and E. K. U. Gross. *Density Functional Theory*. Springer, Berlin, 1990.
- [46] P. Hohenberg and W. Kohn. Inhomogeneous electron gas. *Phys. Rev.*, 136(3B):B864 – B871, 1964.
- [47] W. Kohn and L. J. Sham. Self-consistent equations including exchange and correlations effects. *Phys. Rev.*, 140(4A):A1133 – A1138, 1965.
- [48] G. Brocks, P. J. Kelly, and R. Car. Binding and diffusion of a Si adatom on the Si(100) surface. *Phys. Rev. Lett.*, 66(13):1729–1732, 1991.
- [49] A. P. Smith and H. Jónsson. Dimer and string formation during low temperature silicon deposition on Si(100). *Phys. Rev. Lett.*, 77(7):1326–1329, 1996.
- [50] R. Stumpf and M. Scheffler. Theory of self-diffusion at and growth of Al(111). *Phys. Rev. Lett.*, 72(2):254 – 257, 1994.
- [51] R. Stumpf and M. Scheffler. Ab initio calculations of energies and self-diffusion on flat and stepped surfaces of Al and their implications on crystal growth. *Phys. Rev. B*, 53(8):4958–4973, 1996.
- [52] C. Lee, G. T. Barkema, M. Breeman, A. Pasquarello, and R. Car. Diffusion mechanism of Cu adatoms on a Cu(001) surface. *Surf. Sci.*, 306(3):L575–L578, 1994.



- [53] P. Erhart, K. Albe, and A. Klein. First-principles study of intrinsic point defects in zno: Role of band structure, volume relaxation, and finite-size effects. *Phys. Rev. B*, 73:205203, 2006.
- [54] P. J. Feibelman. Self-diffusion along step bottoms on Pt(111). *Phys. Rev. B*, 66(7):4972–4981, 1999.
- [55] S. Kurth, J. P. Perdew, and P. Blaha. Molecular and solid-state tests of density functional approximations: LSD, GGAs, and meta-GGAs. *Int. J. Quantum. Chem.*, 75(4-5):889–909, 1999.
- [56] M. Itoh, G. R. Bell, A. R. Avery, B. A. Joyce, and D. D. Vvedensky. Island nucleation and growth on reconstructed GaAs(001) surfaces. *Phys. Rev. Lett.*, 81(3):633 – 636, 1998.
- [57] T. Volkmann, M. Ahr, and M. Biehl. Kinetic model of II-VI(001) semiconductor surfaces: Growth rates in atomic layer epitaxy. *Phys. Rev. B*, 69:165303, 2004.
- [58] T. Volkmann. *Lattice Gas Models and Simulations of Epitaxial Growth*. PhD thesis, Bayerische Julius-Maximilians-Universität Würzburg, Würzburg, 2004.
- [59] P. Kratzer and M. Scheffler. Surface knowledge: Toward a predictive theory of materials. *Comput. Sci. Eng.*, 3(6):16–25, 2001.
- [60] P. B. Balbuena and J. M. Seminario, editors. *Molecular Dynamics - From Classical to Quantum Methods*. Elsevier Science, 1999.
- [61] D. C. Rapaport. *The Art of Molecular Dynamics Simulation*. Cambridge University Press, Cambridge, 2nd edition, 2004.
- [62] J. M. Haile. *Molecular Dynamics Simulation - Elementary Methods*. Wiley, New York, 1992.
- [63] M. C. Payne, M. P. Teter, D. C. Allan, T. A. Arias, and J. D. Joannopoulos. Iterative minimization techniques for ab initio total-energy calculations: molecular dynamics and conjugate gradients. *Rev. Mod. Phys.*, 64(4):1045–1097, 1992.
- [64] R. Car and M. Parrinello. Unified approach for molecular dynamics and density-functional theory. *Phys. Rev. Lett.*, 55(22):2471–2474, 1985.
- [65] M. Parrinello. From silicon to RNA: The coming of age of ab initio molecular dynamics. *Solid State Commun.*, 102(2-3):107–120, 1997.

- [66] A. F. Voter, F. Montalenti, and T. C. Germann. Extending the time scale in atomistic simulation of materials. *Annu. Rev. Mater. Res.*, 32:321–346, 2002.
- [67] C. L. Kelchner and A. E. DePristo. Molecular dynamics simulations of multilayer homoepitaxial thin film growth in the diffusion-limited regime. *Surf. Sci.*, 393(1-3):72–84, 1997.
- [68] C. M. Gilmore and J. A. Sprague. Molecular-dynamics simulation of the energetic deposition of ag thin films. *Phys. Rev. B*, 44(16):8950–8957, 1991.
- [69] J. Merikoski, I. Vattulainen, J. Heinonen, and T. Ala-Nissila. Effect of kinks and concerted diffusion mechanisms on mass transport and growth on stepped metal surfaces. *Surf. Sci.*, 387(1-3):167–182, 1997.
- [70] A. Madhukar and S. V. Ghaisas. The nature of molecular beam epitaxial growth examined via computer simulations. *CRC Cr. Rev. Sol. State*, 14:1–131, 1988.
- [71] D. D. Vvedensky, S. Clarke, K. J. Hugill, A. K. Myers-Beaghton, and M. R. Wilby. In M. G. Lagally, editor, *Kinetics of Ordering and Growth at Surfaces*, pages 297–311, New York, 1990. Plenum Press.
- [72] D. P. Landau and K. Binder. *A Guide to Monte Carlo Simulations in Statistical Physics*. Cambridge University Press, Cambridge, 2000.
- [73] M. E. J. Newman and G. T. Barkema. *Monte Carlo Methods in Statistical Physics*. Clarendon Press, Oxford, 1999.
- [74] W. Kinzel and G. Reents. *Physik per Computer*. Spektrum, 1996.
- [75] G. H. Gilmer and K. A. Jackson. *Crystal Growth and Materials*, chapter Computer Simulation of Crystal Growth. North-Holland Publishing Co., Amsterdam, 1977.
- [76] Nicholas Metropolis, A. W. Rosenbluth, M. N. Rosenbluth, A. H. Teller, and E. Teller. Equation of State Calculations by Fast Computing Machines. *J. Chem. Phys.*, 21(6):1087–1092, 1953.
- [77] S. Glasstone, K. J. Laidler, and H. Eyring. *The theory of rate processes - the kinetics of chemical reactions, viscosity, diffusion and electrochemical phenomena*. McGraw-Hill, New York, 1941.
- [78] G. Wahnström. In V. Bortolani, N. H. March, and M. P. Tosi, editors, *Interaction of Atoms and Molecules with Solid Surfaces*, page 529, New York, 1990. Plenum Press.

- [79] K. J. Laidler, editor. *Chemical Kinetics*. Prentice Hall, 3rd edition, London, 1987.
- [80] P. Ruggerone, C. Ratsch, and M. Scheffler. Density-Functional Theory of Epitaxial Growth of Metals. In D. A. King and D. P. Woodruff, editors, *The Chemical Physics of Solid Surfaces*, volume 8, page 490. Elsevier Science, 1997.
- [81] G. Ehrlich. Direct observations of the surface diffusion of atoms and clusters. *Surf. Sci.*, 246(1-3):1–12, 1991.
- [82] S. C. Wang and G. Ehrlich. Atom condensation on an atomically smooth surface: Ir, Re, W, and Pd on Ir(111). *J. Chem. Phys.*, 94:4071–4074, 1991.
- [83] J. Villain. Continuum models of crystal growth from atomic beams with and without desorption. *J. Phys. I*, 1:19–42, 1991.
- [84] Z. W. Lai and S. Das Sarma. Kinetic growth with surface relaxation: Continuum versus atomistic models. *Phys. Rev. Lett.*, 66(18):2348–2351, 1991.
- [85] J. S. Langer. Models of Pattern Formation in First-Order Phase Transitions. In G. Grinstein and G. Mazenko, editors, *Directions in Condensed Matter Physics*, pages 165–186, Singapore, 1986. World Scientific.
- [86] G. B. McFadden, A. A. Wheeler, R. J. Braun, S. R. Coriell, and R. F. Sekerka. Phase-field models for anisotropic interfaces. *Phys. Rev. E*, 48(3):2016–2024, 1993.
- [87] M. Biehl, M. Ahr, W. Kinzel, M. Sokolowski, and T. Volkmann. A lattice gas model of II-VI(001) semiconductor surfaces. *Europhys. Lett.*, 53(2):169–175, 2001.
- [88] M. Ahr and M. Biehl. Flat (001) surfaces of II-VI semiconductors: a lattice gas model. *Surf. Sci.*, 505:124–136, 2002.
- [89] T. Volkmann, F. Much, M. Biehl, and M. Kotrla. Interplay of strain relaxation and chemically induced diffusion barriers: Nanostructure formation in 2D alloys. *Surf. Sci.*, 586(1-3):157–173, 2005.
- [90] W. M. Plotz, K. Hingerl, and H. Sitter. Monte carlo simulation of epitaxial growth. *Phys. Rev. B*, 45(20):12122–12125, 1992.
- [91] A. L. Barabási. Self-assembled island formation in heteroepitaxial growth. *Appl. Phys. Lett.*, 70(19):2565–2567, 1997.

- 
- [92] F. Much, M. Ahr, M. Biehl, and W. Kinzel. Kinetic Monte Carlo simulations of dislocations in heteroepitaxial growth. *Europhys. Lett.*, 56(6):791–796, 2001.
- [93] F. Much, M. Ahr, M. Biehl, and W. Kinzel. A Kinetic Monte Carlo method for the simulation of heteroepitaxial growth. *Comput. Phys. Commun.*, 147:226–229, 2002.
- [94] M. Biehl, M. Ahr, W. Kinzel, and F. Much. Kinetic Monte Carlo simulations of heteroepitaxial growth. *Thin Solid Films*, 428(1-2):52–55, 2003.
- [95] F. Much. *Modeling and Simulation of Strained Heteroepitaxial Growth*. PhD thesis, Bayerische Julius-Maximilians-Universität Würzburg, Würzburg, 2003.
- [96] A. Schindler. *Theoretical aspects of growth on one and two dimensional strained crystal surfaces*. PhD thesis, Gerhard-Mercator-Universität Duisburg, Duisburg, 1999.
- [97] S. Weber. *Simulation of self-assembled nanopatterns in binary alloys on the fcc(111) surface*. PhD thesis, Julius-Maximilians-Universität Würzburg, Würzburg, 2008.
- [98] H. Bethge, D. Heuer, C. Jensen, K. Reshöft, and U. Köhler. Misfit-related effects in the epitaxial growth of iron on W (110). *Surf. Sci.*, 331-333(Part 2):878–884, 1995.
- [99] D. Sander, R. Skomski, A. Enders, C. Schmidhals, and J. Kirschner. The correlation between mechanical stress and magnetic properties of ultrathin films. *J. Phys. D: Appl. Phys.*, 31(6):663–670, 1998.
- [100] A. Enders D. Sander and J. Kirschner. Strain dependence of the magnetic properties of nm Fe films on W(100). *J. Appl. Phys.*, 85(5):5279–5281, 1999.
- [101] W. H. Press, S. A. Teukolsky, W. T. Vetterling, and B. P. Flannery. *Numerical recipes in C*. Cambridge University Press, Cambridge, 2 edition, 1992.
- [102] J. P. K. Doye and D. J. Wales. Thermodynamics of Global Optimization. *Phys. Rev. Lett.*, 80(7):1357–1360, 1998.
- [103] M. Schroeder and D. E. Wolf. Diffusion on strained surfaces. *Surf. Sci.*, 375(1):129–140, 1997.
- [104] G. T. Barkema and N. Mousseau. Event-Based Relaxation of Continuous Disordered Systems. *Phys. Rev. Lett.*, 77(21):4358–4361, 1996.

- 
- [105] N. Mousseau and G. T. Barkema. Traveling through potential energy landscape of disordered materials: The activation-relaxation technique. *Phys. Rev. E*, 57(2):2419–2424, 1998.
- [106] R. Malek and N. Mousseau. Dynamics of Lennard-Jones clusters: A characterization of the activation-relaxation technique. *Phys. Rev. E*, 62(6):7723–7728, 2000.
- [107] K. A. Fichthorn and W. H. Weinberg. Theoretical foundations of dynamical Monte Carlo simulations. *J. Chem. Phys.*, 95(2):1090–1096, 1991.
- [108] D. E. Knuth. *The Art of Computer Programming*. Addison-Wesley, Massachusetts, 2 edition, 1981.
- [109] C. Vey. Kinetische Monte Carlo Simulation von heteroepitaktischem Wachstum. Diplomarbeit, Bayerische Julius-Maximilians-Universität Würzburg, Würzburg, 2004.
- [110] R. F. Sabiryanov, M. I. Larsson, K. J. Cho, W. D. Nix, and B. M. Clemens. Surface diffusion and growth of patterned nanostructures on strained surfaces. *Phys. Rev. B*, 67:125412, 2003.
- [111] L. Dong, J. Schnitker, R. W. Smith, and D. J. Srolovitz. Stress relaxation and misfit dislocation nucleation in the growth of misfitting films: A molecular dynamics simulation study. *J. Appl. Phys.*, 83(1):217–227, 1998.
- [112] R. L. Schwoebel and E. J. Shipsey. Step Motion on Crystal Surfaces. *J. Appl. Phys.*, 37(10):3682–3686, 1966.
- [113] J. de la Figuera, K. Pohl, O. R. de la Fuente, A. K. Schmid, N. C. Bartelt, C. B. Carter, and R. Q. Hwang. Direct Observation of Misfit Dislocation Glide on Surfaces. *Phys. Rev. Lett.*, 86(17):3819–3822, 2001.
- [114] A. S. Bader, W. Faschinger, C. Schumacher, J. Geurts, and L. W. Molenkamp. Real-time in situ x-ray diffraction as a method to control epitaxial growth. *Appl. Phys. Lett.*, 82(26):4684–4686, 2003.
- [115] O. Trushin, E. Granato, S. C. Ying, P. Salo, and T. Ala-Nissila. Energetics and atomic mechanisms of dislocation nucleation in strained epitaxial layers. *Phys. Rev. B*, 68(15):155413, 2003.
- [116] J. Coelho, G. Patriarche, F. Glas, G. Saint-Girons, I. Sagnes, and L. Largeau. Buried dislocation networks designed to organize the growth of III-V semiconductor nanostructures. *Phys. Rev. B*, 70(15):155329, 2004.
- [117] F. Leroy, J. Eymery, P. Gentile, and F. Fournel. Controlled surface nanopatterning with buried dislocation arrays. *Surf. Sci.*, 545:211–219, 2003.

- [118] H. Brune, M. Giovannini, K. Bromann, and K. Kern. Self-organized growth of nanostructure arrays on strain-relief patterns. *Nature*, 394:451–453, 1998.
- [119] A. Bourret. How to control the self-organization of nanoparticles by bonded thin layers. *Surf. Sci.*, 432:37–53, 1999.
- [120] A. E. Romanov, P. M. Petroff, and J. S. Speck. Lateral ordering of quantum dots by periodic subsurface stressors. *Appl. Phys. Lett.*, 74(16):2280–2282, 1999.
- [121] F. Much and M. Biehl. Simulation of wetting-layer and island formation in hetero epitaxial growth. *Europhys. Lett.*, 63(1):14–20, 2003.
- [122] M. Belzer. Oberflächenwachstum von zweidimensionalen Kristallen mit Dreiecksgitterstruktur. Diplomarbeit, Gerhard-Mercator-Universität-Gesamthochschule Duisburg, Duisburg, 1995.
- [123] J. Zegenhagen, P. F. Lyman, M. Böhringer, and M. J. Bedzyk. Discommensurate Reconstructions of (111)Si and Ge Induced by Surface Alloying with Cu, Ga and In. *Phys. Stat. Sol. (b)*, 204:587–616, 1997.
- [124] S. O. Ferreira, B. R. A. Neves, R. Magalhães Paniago, A. Malachias, P. H. O. Rappl, A. Y. Ueta, E. Abramof, and M. S. Andrade. AFM characterization of PbTe quantum dots grown by molecular beam epitaxy under Volmer-Weber mode. *J. Cryst. Growth*, 231(1-2):121–128, 2001.
- [125] S. O. Ferreira, E. C. Paiva, G. N. Fontes, and B. R. A. Neves. Characterization of CdTe quantum dots grown on Si(111) by hot wall epitaxy. *J. Appl. Phys.*, 93(2):1195–1198, 2003.
- [126] A. Raviswaran, C.-P. Liu, J. Kim, D. G. Cahill, and J. M. Gibson. Evolution of coherent islands during strained-layer Volmer-Weber growth of Si on Ge(111). *Phys. Rev. B*, 63(12):125314, 2001.
- [127] M. C. Kuo, C. S. Yanga, P. Y. Tsenga, J. Leea, J. L. Shena, W. C. Chou, Y. T. Shi, C. T. Kud, M. C. Leed, and W. K. Chen. Formation of self-assembled ZnTe quantum dots on ZnSe buffer layer grown on GaAs substrate by molecular beam epitaxy. *J. Cryst. Growth*, 242(3–4):533–537, 2002.
- [128] Z. M. Zhao, O. Hulko, T. S. Yoon, and Y. H. Xie. Initial stage of InAs growth on Si (001) studied by high-resolution transmission electron microscopy. *J. Appl. Phys.*, 98(12):123526, 2005.
- [129] G. Russo and P. Smereka. Computation of Strained Epitaxial Growth in Three Dimensions by Kinetic Monte Carlo. *J. Comput. Phys.*, 214:809–828, 2006.

- [130] I. V. Markov. *Crystal Growth for Beginners: Fundamentals of Nucleation, Crystal Growth and Epitaxy*. World Scientific, Singapore, 1995.
- [131] E. Bauer and Jan H. van der Merwe. Structure and growth of crystalline superlattices: From monolayer to superlattice. *Phys. Rev. B*, 33(6):3657–3671, 1986.
- [132] P. M. J. Marée, K. Nakagawa, F. M. Mulders, J. F. van der Veen, and K. L. Kavanagh. Thin epitaxial Ge-Si(111) films: study and control of morphology. *Surf. Sci.*, 191:305–328, 1987.
- [133] Y.-W. Mo, D. E. Savage, B. S. Swartzentruber, and M. G. Lagally. Kinetic pathway in Stranski-Krastanov growth of Ge on Si(001). *Phys. Rev. Lett.*, 65(8):1020–1023, 1990.
- [134] Y. W. Mo and M. G. Lagally. Scanning tunneling microscopy studies of the growth process of Ge on Si(001). *J. Cryst. Growth*, 111:876 – 881, 1991.
- [135] P. Sutter and M. G. Lagally. Nucleationless Three-Dimensional Island Formation in Low-Misfit Heteroepitaxy. *Phys. Rev. Lett.*, 84(20):4637–4640, 2000.
- [136] C. W. Snyder, B. G. Orr, D. Kessler, and L. M. Sander. Effect of strain on surface morphology in highly strained InGaAs films. *Phys. Rev. Lett.*, 66(23):3032–3035, 1991.
- [137] C. Heyn. Critical coverage for strain-induced formation of InAs quantum dots. *Phys. Rev. B*, 64(16):165306, 2001.
- [138] K. Alchalabi, D. Zimin, G. Kostorz, and H. Zogg. Self-Assembled Semiconductor Quantum Dots with Nearly Uniform Sizes. *Phys. Rev. Lett.*, 90(2):026104, 2003.
- [139] D. Schikora, S. Schwedhelm, D. J. As, K. Lischka, D. Litvinov, A. Rosenauer, D. Gerthsen, M. Strassburg, A. Hoffmann, and D. Bimberg. Investigations on the Stranski-Krastanov growth of CdSe quantum dots. *Appl. Phys. Lett.*, 76(4):418–420, 2000.
- [140] J. E. Prieto and I. Markov. Quantum-dot nucleation in strained-layer epitaxy: Minimum-energy pathway in the stress-driven two-dimensional to three-dimensional transformation. *Phys. Rev. B*, 72:205412, 2005.
- [141] J. E. Prieto and I. Markov. Thermodynamic driving force of formation of coherent three-dimensional islands in Stranski-Krastanov growth. *Phys. Rev. B*, 66:073408, 2002.

- [142] K. E., Khor, and S. Das Sarma. Quantum dot self-assembly in growth of strained-layer thin films: A kinetic Monte Carlo study. *Phys. Rev. B*, 62(24):16657–16664, 2000.
- [143] J. M. Moison, F. Houzay, F. Barthe, L. Leprince, E. André, and O. Vatel. Self-organized growth of regular nanometer-scale InAs dots on GaAs. *Appl. Phys. Lett.*, 64(2):196–198, 1994.
- [144] E. Korutcheva, A. M. Turiel, and I. Markov. Coherent Stranski-Krastanov growth in 1+1 dimensions with anharmonic interactions: An equilibrium study. *Phys. Rev. B*, 61:16890–16901, 2000.
- [145] Y. H. Xie, G. H. Gilmer, C. Roland, P. J. Silverman, S. K. Buratto J. Y., Cheng, E. A. Fitzgerald, A. R. Kortan, S. Schuppler, M. A. Marcus, and P. H. Citrin. Semiconductor Surface Roughness: Dependence on Sign and Magnitude of Bulk Strain. *Phys. Rev. Lett.*, 73(22):3006–3009, 1994.
- [146] M. Tikhov and E. Bauer. Growth, structure and energetics of ultrathin ferromagnetic single crystal films on Mo(110). *Surf. Sci.*, 232(1–2):73–91, 1990.
- [147] J. Malzbendera, M. Przybylski, J. Giergiela, and J. Kirschner. Epitaxial growth of Fe on Mo(110) studied by scanning tunneling microscopy. *Surf. Sci.*, 414(1–2):187–196, 1998.
- [148] P. O. Jubert, O. Fruchart, and C. Meyer. Self-assembled growth of faceted epitaxial Fe(110) islands on Mo(110)/Al<sub>2</sub>O<sub>3</sub> (11 $\bar{2}$ 0). *Phys. Rev. B*, 64:115419, 2001.
- [149] Z. Q. Wang, Y. S. Li, F. Jona, and P. M. Marcus. Epitaxial growth of body-centered-cubic nickel on iron. *Solid State Commun.*, 61(10):1376, 1987.
- [150] F. Scheurera, B. Carrièrea, J. P. Devillea, and E. Beaurepaire. Evidence of epitaxial growth of bcc Co on Cr(100). *Surf. Sci.*, 245(3):L175–L185, 1991.
- [151] B. F. P. Roos, A. R. Frank, S. O. Demokritov, and B. Hillebrands. Epitaxial growth of metastable Pd(0 0 1) on BCC-Fe(0 0 1). *J. Magn. Magn. Mater.*, 198–199:725–727, 1999.
- [152] J. Thomassen, F. May, B. Feldmann, M. Wuttig, and H. Ibach. Magnetic live surface layers in Fe/Cu(100). *Phys. Rev. Lett.*, 69(26):3831–3834, 1992.
- [153] M. Schroeder. *Diffusion und Wachstum auf Kristalloberflächen*. PhD thesis, Gerhard-Mercator-Universität Duisburg, Duisburg, 1997.
- [154] F. Much. *Strukturbildung in der Heteroepitaxie*. Diplomarbeit, Bayerische Julius-Maximilians-Universität Würzburg, Würzburg, 2000.



- 
- [155] G. Wedler, C.M. Schneider, A. Trampert, and R. Koch. Strain relief of heteroepitaxial bcc-fe(001) films. *Phys. Rev. Lett.*, 93(23):236101, 2004.
- [156] H. Brune, K. Bromann, H. Röder, K. Kern, J. Jacobsen, P. Stoltzer, K. Jacobsen, and J. Nørskov. Effect of strain on surface diffusion and nucleation. *Phys. Rev. B*, 52(20):R14380–R14383, 1995.
- [157] F. Jensen. *Introduction to Computational Chemistry*. Wiley, Chichester, 1999.
- [158] J. E. Jones. On the Determination of Molecular Fields. – II. From the Equation of State of a Gas. *Proc. Roy. Soc.*, A106(738):463–477, 1924.
- [159] S. Zehn and G. J. Davies. Calculation of the Lennard–Jones n-m Potential Energy Parameters for Metals. *Phys. Stat. Sol. (a)*, 78(2):595–605, 1983.
- [160] N. W. Ashcroft and N. D. Mermin. *Festkörperphysik*. Oldenbourg Verlag, München, 2001.
- [161] P. M. Morse. Diatomic Molecules According to the Wave Mechanics. II. Vibrational Levels. *Phys. Rev.*, 34(1):57–64, 1929.
- [162] I. Markov and A. Trayanov. Epitaxial interfaces with realistic inter-atomic forces. *J. Phys. C Solid State*, 21(13):2475–2493, 1988.
- [163] J. R. Hart and A. K. Rappé. van der Waals functional forms for molecular simulations. *J. Chem. Phys.*, 97(2):1109–1115, 1992.



# Danksagung

An dieser Stelle möchte ich mich bei den Personen bedanken, die auf unterschiedlichste Art und Weise zum Gelingen dieser Arbeit beigetragen haben. Insbesondere gilt mein Dank:

- Priv. Doz. Dr. Michael Biehl für die gute Betreuung dieser Arbeit sowie die vielfachen Anregungen und Ideen.
- Prof. Dr. Wolfgang Kinzel für die Möglichkeit, die vorliegende Arbeit an seinem Lehrstuhl anzufertigen.
- Dr. Miroslav Kotrla für die Gastfreundschaft an der Tschechischen Akademie der Wissenschaften in Prag und die fruchtbare Zusammenarbeit.
- Sebastian Weber für die hilfreichen Diskussionen und die fachliche sowie freundschaftliche Zusammenarbeit.
- Corinna Schreck für das sorgfältige Korrekturlesen dieser Arbeit.
- den Systembetreuern der Universität Würzburg für die hervorragende Wartung des Computersystems.
- allen Mitgliedern unseres Lehrstuhls für die angenehme und freundliche Arbeitsatmosphäre, die mir ein konstruktives Arbeiten ermöglicht hat.
- der Deutschen Forschungsgemeinschaft für die Finanzierung dieser Arbeit im Rahmen des Sonderforschungsbereich 410.
- meiner Familie für die Unterstützung während meines Studiums und der Anfertigung dieser Arbeit.



# Lebenslauf

## Angaben zur Person

Markus Walther  
geboren am 08.03.1978 in Füssen  
Staatsangehörigkeit: deutsch  
Familienstand: ledig

## Schulbildung

09/1984–07/1988 Christoph-von-Schmid-Grundschule Dinkelsbühl  
09/1988–07/1997 Gymnasium Dinkelsbühl,  
Allgemeine Hochschulreife

## Wehrdienst

11/1997–08/1998 Luftwaffe in Bayreuth und Neuburg an der Donau

## Studium

11/1998–12/2003 Studium der Physik an der  
Bayerischen Julius-Maximilians-Universität Würzburg  
Diplomarbeit: *Hügelform und Skalenverhalten beim  
instabilen Wachstum: Kinetische Monte Carlo Simulation*

## Promotion

01/2004–02/2008 Wissenschaftlicher Mitarbeiter am Institut für Theoretische  
Physik und Astrophysik der Universität Würzburg  
08/2006 Forschungsaufenthalt bei Dr. Miroslav Kotrla an der  
Tschechischen Akademie der Wissenschaften in Prag

